Summer 2021

Development of Eam and Rf-MEAM Interatomic Potential for Zirconium Diboride

Bikash Timalsina
Missouri State University, bik369@live.missouristate.edu

Recommended Citation
Timalsina, Bikash, "Development of Eam and Rf-MEAM Interatomic Potential for Zirconium Diboride" (2021). *MSU Graduate Theses*. 3670.
https://bearworks.missouristate.edu/theses/3670

DEVELOPMENT OF EAM AND RF-MEAM INTERATOMIC POTENTIAL FOR ZIRCONIUM DIBORIDE

A Master's Thesis
Presented to
The Graduate College of
Missouri State University

In Partial Fulfillment
Of the Requirements for the Degree
Master of Science, Materials Science

By
Bikash Timalsina
July 2021

DEVELOPMENT OF EAM AND RF-MEAM INTERATOMIC POTENTIAL FOR ZIRCONIUM DIBORIDE

Physics, Astronomy and Materials Science

Missouri State University, July 2021

Master of Science

Bikash Timalsina

ABSTRACT

Embedded Atom Method (EAM) and Modified-EAM (MEAM) interatomic potentials were developed for zirconium diboride (ZrB_2). The EAM and "Reference Free" (RF) version of the Modified Embedded Atom Method (RFMEAM) potentials have been fitted by utilizing Density Functional Theory (DFT)-based datasets including lattice deformations and high-temperature *ab-initio* molecular dynamics (AIMD) simulation results. The occupancies of phonons for acoustic phonon modes from the density functional theory calculation shows that these modes of vibration, mostly due to heavier mass element (Zr), which occur below $8.711\ THz$, while a slight underestimation to that of DFT calculation predicted by EAM below $8.439\ THz$ and an overestimation predicted by RF-MEAM below $8.880\ THz$. Consequently, the frequency shifting of acoustic phonon modes for heavier mass element (Zr) on EAM and RF-MEAM potential models results in a similar frequency shifts on optical modes which is mostly due to lighter element (B); the frequency range for optical modes is $12.013 - 22.733\ THz$ for EAM and $12.616 - 23.957\ THz$ for RF-MEAM models compared to the frequency range of $12.181 - 23.124\ THz$ by DFT calculation. In addition, the bulk modulus of ZrB_2 for EAM and RF-MEAM potential models are $263.81\ GPa$ and $254.78\ GPa$ compared to that of ground state DFT calculation of $238\ GPa$. Overall, the results showed that the applicability of EAM and RF-MEAM to modeling the interatomic potentials of the diboride system.

KEYWORDS: interatomic potential, molecular dynamics, thermal properties, zirconium diboride, ultra-high temperature ceramics

DEVELOPMENT OF EAM AND RF-MEAM INTERATOMIC POTENTIAL FOR ZIRCONIUM DIBORIDE

By

Bikash Timalsina

A Master's Thesis
Submitted to the Graduate College
Of Missouri State University
In Partial Fulfillment of the Requirements
For the Degree of Master of Science, Materials Science

July 2021

Approved by:

Ridwan Sakidja, Ph.D., Thesis Committee Chair

Kartik C. Ghosh, Ph.D., Committee Member

Tiglet Besara, Ph.D., Committee Member

Julie Masterson, Ph.D., Dean of the Graduate College

ACKNOWLEDGEMENTS

First and foremost, my sincere gratitude to my advisor, Dr. Ridwan Sakidja for his constant support and guidance over the past two years. I would like to offer my appreciation to him for advising in my research and mentoring me in every way possible up to this end. I would also like to thank him for encouraging me to participate in various conferences and present my research work.

I would like to thank Dr. Kartik C. Ghosh and Dr. Tiglet Besara for serving as a committee member in my thesis defense. I am grateful to all the faculties and staff in the department of Physics, Astronomy and Materials Science for providing me an opportunity to learn and grow. Also, I would like to acknowledge the support from the NSF Division of Civil, Mechanical & Manufacturing Innovation (CMMI) within the Directorate for Engineering with an award number 1902069. In addition, I am also grateful for the computing support provided by the National Energy Research Scientific Computing Center (NERSC).

Finally, I would like to thank all the colleagues in my research group for providing their valuable support, assistance and discussion. Also, I am thankful to fellow graduate students and friends who were in constant touch with me providing emotional support and making my time memorable and enjoyable.

I dedicate this thesis to my father Muktinath Timalsina and my mother Devkumari Timalsina.

TABLE OF CONTENTS

LIST OF TABLES

LIST OF FIGURES

INTRODUCTION

Literature Review

Zirconium diboride is an ultra-high temperature composite (UHTC) of zirconium and boron that has many aerospace applications in extreme environments. The melting points of ceramics based on transition-metal borides, nitrides, and carbides are extremely high. High melting points ($> 3000°C$), high thermal and electrical conductivity, chemical inertness against molten metals, and excellent thermal shock resistance are all characteristics of zirconium diboride[1-3]. Due to these fascinating properties zirconium diboride has wide range of applications in thermal protective structures for leading-edge components on hypersonic reentry space vehicle propulsion systems, furnace elements, refractory crucibles, and plasma-arc electrodes[1, 4]. Among the ultrahigh temperature ceramics, zirconium diboride has the lowest theoretical density, making it a desirable substrate for aerospace applications[1, 2, 4].

The synthesis of several ultrahigh temperature composites including zirconium diboride date back to late 1800, however, due to the lack of potential usage and technological advancement, its research interest only significantly grew during the space race in late 1950's[5-7]. In the United States, several assessment of ultrahigh temperature ceramics matrix composites of borides, nitrides, oxides and silicides etc. have been conducted over 1960's to be used for gas turbines engine that withstand temperature of 1650°C in oxidizing environment[8]. The composites of oxides were mostly investigated because of its high resistant to oxidation but due to higher creep rates in polycrystalline oxide composites, other ceramic composites of borides, nitrides and silicides were explored[8]. In 1963, first major effort was carried out for composites of diboride with an aim in establishing the understanding of physical, thermodynamic and oxidation characteristics of diboride in terms of composition, temperature and oxidation response[8, 9].

While many experimental studies have focused on zirconium diboride, relatively little computational modelling has been done on the atomistic scale. This is mainly due to lack of accurate interatomic potentials for ZrB2, which is in stark contrast to zirconium (Zr) metal. For metals like Zr, the lack of angular dependence for the metallic bonds, especially in a highly coordinated environment, has enabled development of many interatomic potential types, such as the Embedded Atom Method/Finnis-Sinclair (EAM/FS)[71-73]. The EAM approach, has been extended from the FS potential for Hf and Zr from William and Massobrio to become the first interatomic potential developed for ZrB_2 and HfB_2[64]. Daw et.al reparametrized and developed Tersoff style potential for the two diboride compounds by converting the FS potentials of elemental zirconium and hafnium into the 3-body Tersoff interatomic potential form[64, 74]. In their approach, the Tersoff style potential was chosen to address the relatively high degree of covalency in the hexagonal sheets of boron atoms that extend along the basal planes as well as the out-of-plane Zr-B and Hf-B bonds[64]. However, the much lower coordination number involved in the diborides that results from the presence of directional/covalent bonding increases the significance of angular dependency of the interatomic bonding, which cannot simply be ignored for ZrB_2 and HfB_2. In fact, as also observed by Daw et al., this has resulted in an inaccurate calculation of the elastic constants[64]. Daw et al. indicate that this might be a ramification of choosing FS potentials as the starting point for reparameterizations since they are better suited for non-directional metallic bonds. Recently, a ReaxFF type interatomic potential was developed for ZrB2 to study bond formation, dissociation, diffusion-based processes, and oxidation. However, the potential placed more emphasis in modeling chemical reactions at the surface and has not been fully tested for bulk mechanical properties[75-77]. Most recently, Zhang demonstrated a machine learning algorithm to generate a spectral neighbor analysis potential (SNAP) potential for ZrB2[78]. The SNAP potential employed several types of molecular dynamics snapshots, crystalline lattice and aspect-ratio variations, and deformation datasets for training.

Structure of Zirconium Diboride

Zirconium diboride is a transition metal diboride that has hexagonal crystal structure with the lattice parameter $a = 3.18$ Å and $c = 3.547$ Å consisting of one zirconium and two boron atoms in a unit cell. The transition metal (zirconium) and boron are arranged as an alternating zirconium and boron layer with P6/mmm symmetry. Each of the zirconium atom in zirconium plane is surrounded by 6 other zirconium atoms and 12 out-of-plane boron atoms. The zirconium atoms in a zirconium layer have metallic bonding. In the boron layer, each boron atom is surrounded by three boron atoms forming sp^2 bond (covalent bond) in the plane. Additionally, the boron atom is surrounded by six zirconium atoms. Considering the nearest neighbor, first, second and third nearest neighbor for zirconium are at 2.547 Å (out of Zr plane), 3.173 Å (in the Zr plane) and 4.069 Å (out of Zr plane). Similarly, first, second and third nearest neighbor for boron are at 1.832 Å (in the B plane), 2.547 Å (out of B plane) and 3.664 Å (in the B plane). The structure representing zirconium diboride is given below in Figure 1.

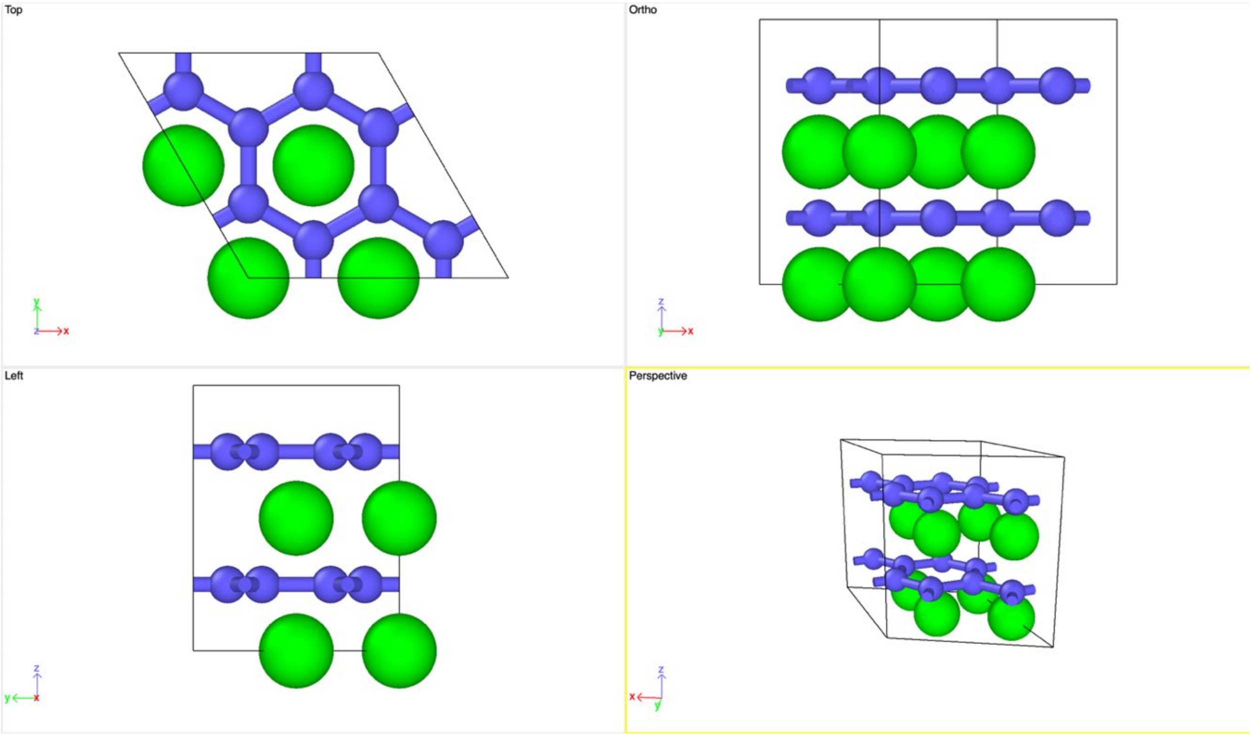

Figure 1: Eight-unit cells (2x2x2) of zirconium diboride expanded along a, b and c orientation. Here, green circle represents zirconium atom and blue circle represent boron atom. Each of the unit cells in this figure represent different perspective of the 2x2x2 unit cell of zirconium diboride.

Similarly, the transition metal (TM) zirconium in zirconium layer is exactly above the midpoint of hexagonal boron ring in boron layer. For the position of zirconium and boron atom in a unit cell, the zirconium atom is positioned at (0,0,0) and two boron atoms are positioned at (1/3, 2/3, ½) and (2/3, 1/3, ½). The zirconium metal could be replaced by other transition metal (TM) like Hf, Ti, Va, Nb and yet still retains the same structure (P6/mmm) as that of zirconium diboride[2]. However, the lattice parameter is changed in accordance with the size of transition metal being replaced for zirconium atom. For example, replacing zirconium atom by hafnium atom would lead in the increase of lattice parameter a (due to Hf-Hf interaction) and c (due to Hf-B interaction). The variation of lattice parameter a is characterized by transition metal (TM)-transition metal (TM) interaction and the lattice parameter c is characterized by TM-B interaction. Due to TM-TM interaction along the plane and TM-B interaction out of the plane, the variations in lattice parameter a and c in changing transition metal are different, usually c increases or decreases more than a[2].The structural integrity in ZrB_2 is related to Zr-Zr, Zr-B and B-B interaction or bond strength. The strength, hardness and stiffness in ZrB_2 is contributed by B-B bond strength and Zr-B bonds formed by zirconium donating two electrons and each boron atoms in unit cell sharing one electron contributes to the melting temperature[2]. Also, remaining free valence electrons in Zr-Zr plane contributes for the thermal and electrical conductivities in ZrB_2[2].

Thermal Properties of Zirconium Diboride

The unconventional structure of zirconium diboride and its unique properties at the atomic and electronic level contributes to the excellent thermal properties. Several works on zirconium diboride reports the melting point greater than $3000°C$[1, 2, 4, 10]. Being anisotropic material, zirconium diboride has different thermal properties along lattice direction a and c. For instance, the thermal expansion of ZrB_2 is different in the different lattice directions. The thermal expansion coefficient measures the rate at which the lattice expands by increasing the temperature. This anisotropic behavior on thermal expansion have been extensively studied. Previous work by Belikov reported the thermal expansion of polycrystalline zirconium diboride by X-ray diffraction along a to be $6.63 * 10^{-6}\ /K$ and that along c to be $7.35 * 10^{-6}\ /K$ for temperature range $300 - 1070\ K$[11]. Keihn also reported similar expansion coefficient for zirconium diboride powder sample along a to be $6.6 * 10^{-6}\ /K$ and along c to be $6.78 * 10^{-6}\ /K$ for temperature range $300 - 1023K$ and also, different expansion from temperature range $1027 - 2073K$ to be $8.62 * 10^{-6}/K$ and $7.65 * 10^{-6}/K$ for a and c[12]. Further, experimental study by Lonnberg modelled the thermal expansion coefficient for temperature range $300 - 1500K$ along a by $\alpha_a = 4.397 * 10^{-6} + 4.494 * 10^{-9}\,T$ and on c by $\alpha_c = 4.682 * 10^{-6} + 4.190 * 10^{-9}T$[13]. All of the study were for either polycrystalline or powder sample. The thermal expansion coefficient measurement on single crystal ZrB_2 sample Okamoto also reported similar results of expansion along a to be $6.66 * 10^{-6}/K$ and along c to be $6.93 * 10^{-6}/K$. Nonetheless, the thermal expansion for broad range of temperature for different polycrystalline sample is given below in Figure 2.

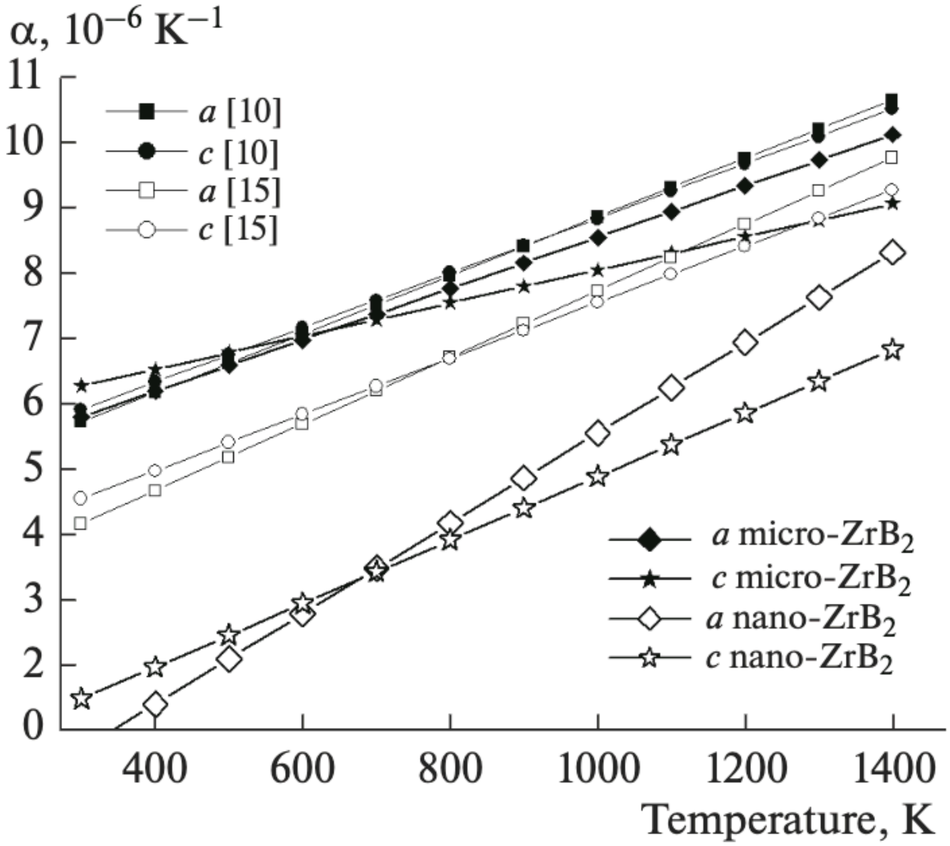

Figure 2: Thermal expansion coefficient for micro crystalline and nano crystalline zirconium diboride sample along lattice direction a and c obtained from D.Y. Kovalev[11]. In X-axis is the temperature in Kelvin and Y-axis is the thermal expansion coefficient in per Kelvin.

Similarly, the ability of matter to conduct heat is known as thermal conductivity. Heat is transferred in solids by conduction, which is caused by electrons and phonons. The propagation of elastic waves, also known as phonons, is responsible for the transfer of heat energy between atoms in ceramics at low temperatures. The room temperature thermal conductivity of ZrB_2 is $95\ W/mK$[14, 15]. Experimental studies have shown a large variation in thermal conductivity of zirconium diboride. Variations in manufacturing technique, impurities, contaminants, and grain sizes have all contributed to variations in thermal conductivity[16, 17]. The thermal conductivity of ZrB2 has been stated to be as low as 38 W/mK and as high as 95 W/mK for ZrB2 from different techniques[18, 19]. The mechanism by which phonons contribute to the thermal conductivity of ZrB_2 type ceramics is close to that of other covalent and ionic bonded ceramics. In diborides, the phonon contribution to thermal conductivity is mostly insignificant in comparison to the electron contribution. At room temperature, the phonon contribution is normally $1/3$ that of the electron contribution, decreasing to $1/8$ at $1000°C$[16]. The metallic bonding in the ZrB_2 crystal structure of diborides contributes to electron contribution to thermal conductivity. Electron contribution to thermal conductivity, is generated by free electron motion in the close packed layers of zirconium atoms and can be obtained theoretically by Wiedemann-Lorenz-Franz law as $\lambda_{el} = L\sigma T$ where, L is Lorenz number and σ the electrical conductivity[20, 21]. Several works have reported the thermal conductivity due to electron contribution is greater than 66% of total thermal conductivity of zirconium diboride[16, 22]. The thermal conductivity in ZrB_2 for wide range of temperature is given below in Figure 3.

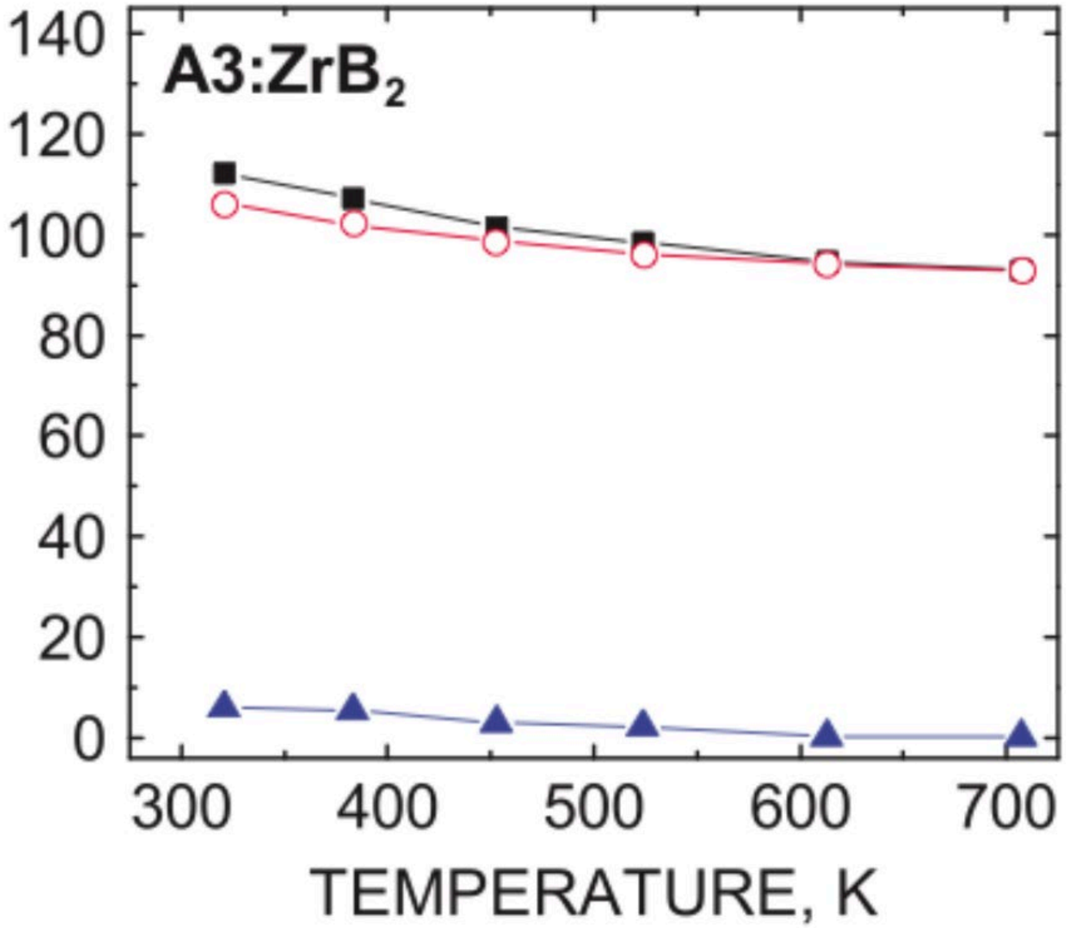

Figure 3: The electron (open circles) and phonon (triangles) contributions to ZrB2's overall thermal conductivity (squares) from Zhang[14]. The horizontal axis (x-axis) is temperature in Kelvin and vertical axis (y-axis) is thermal conductivity measured in W/mk.

Thermal Properties in a Crystalline Solid

The thermal properties in a crystalline solid structure are related to the electrons and lattice vibration (atomic vibration)[23]. At the ground state, atoms are held perfectly in static positions through stiff chemical bonds as shown below in Figure 4[23]. These chemical bonds are forces due to potential energy between atoms that hold them together in a crystal[23]. However, as temperature increases, the kinetic energy of atoms in a crystal increases and consequently the atomic vibration increases. In a crystalline solid structure, the atoms vibrate within the crystal and these atomic vibration dictates many thermal properties like thermal expansion, specific heat capacity, lattice thermal conductivity and other thermodynamical parameters including entropy and free energy[23].

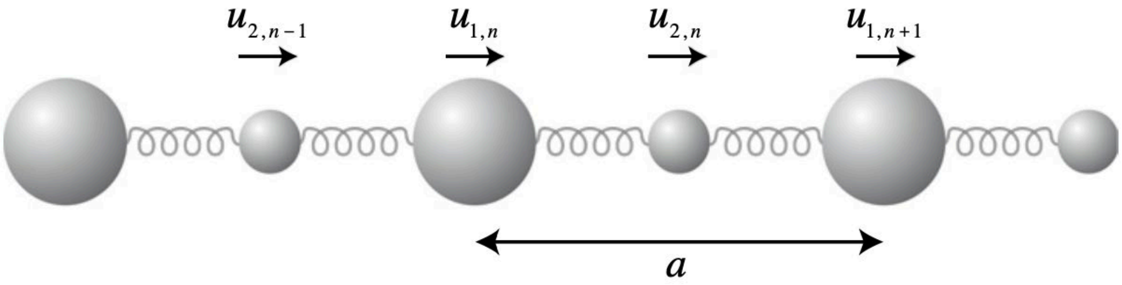

Figure 4: Representation of lattice vibration in a simple diatomic chain of unit cell length a. Here, spring represents the chemical bonds (forces between atoms) and $u's$ are small atomic displacement around equilibrium.

Now, in the study of lattice vibration**,** the atomic motions are explained in terms of phonons, which are harmonic travelling waves that can be characterized by its frequency, amplitude and direction of travel. The phonons are dependent on forces between atoms. At low temperature harmonic theory of lattice vibration explains very well the thermal properties of crystalline solid, as pressure of gas of harmonic phonons is temperature independent because the frequency of phonon does not depend on the amplitude of the oscillation[24]. In the harmonic theory of lattice vibration, the oscillations of atoms are very small from the equilibrium sites which can be expressed in constructing the potential energy as[23]

$$E(r) = E_0 + \frac{1}{2!}\frac{\partial^2 E}{\partial r^2}\Big|_{r=r_0} (r - r_0)^2 \qquad (1)$$

Where, E_0 is the potential energy at ground state i.e., at $0\ K$ and the latter term in above equation is the potential energy due to small oscillation of atoms around equilibrium. The form of the potential energy above is able to accurately explain some of the thermal properties like specific heat, Debye-Waller factor, thermal diffuse scattering etc. at the low temperature. However, the harmonic theory of lattice vibration is not able to explain other ubiquitous phenomenon like thermal expansion, thermal conductivity and deviation from harmonic expression for Debye-Waller factor because these phenomenon are very significant at high temperature and since only small atomic vibration are taken in account but at high temperature these atomic vibration are considerable so anharmonic correction to energy expression which are higher order terms of atomic oscillation are added to essentially encompass these phenomenon[24]. The energy expression is then given by

$$E(r) = E_0 + \frac{1}{2!}\frac{\partial^2 E}{\partial r^2}\Big|_{r=r_0} (r - r_0)^2 + \frac{1}{3!}\frac{\partial^3 E}{\partial r^3}\Big|_{r=r_0} (r - r_0)^3 + \cdots \tag{2}$$

Addition of anharmonic term in energy expression, the phonon gas acquires a finite temperature dependent pressure. This temperature dependent pressure explains the lattice thermal expansion of a crystal. From the thermodynamic expression, the linear expansion coefficient is given by

$$\alpha = \frac{1}{3V}\left(\frac{\partial V}{\partial T}\right)_P = -\frac{1}{3V}\frac{\left(\frac{\partial P}{\partial T}\right)_V}{\left(\frac{\partial P}{\partial V}\right)_T} = \frac{1}{3B}\left(\frac{\partial P}{\partial T}\right)_V \tag{3}$$

Where, P, T and V and B are the temperature, pressure, volume and bulk modulus of the given crystal structure. It is obvious from the above thermodynamic expression that the thermal expansion is related to temperature dependent pressure. Now, in crystalline solid this pressure is the phonon pressure acquired by atoms at the given temperature which is given by[24]

$$P = P_{ph} = -\frac{\partial}{\partial V}\left[\frac{1}{2}\sum_{k,s} \hbar\omega_s(k)\right] + \sum_{k,s}\left(-\frac{\hbar\partial\omega_s(k)}{\partial V}\right)\frac{1}{e^{\beta\hbar\omega_s(k)}-1} \tag{4}$$

Where, P_{ph} is phonon pressure, $\omega_s(k)$ is the phonon frequency in a reciprocal lattice vector k and $\beta = 1/k_B T$ where, k_B is Boltzmann constant and $\hbar$ the reduced Planck's constant. In the above equation of phonon pressure, the second term i.e., the volume dependent phonon frequencies vanish, and the lattice thermal expansion coefficient is zero at all temperature if the potential energy expression has only harmonic term. From the above expression lattice thermal expansion is related to volume and temperature dependent phonon pressure.

$$\alpha = \frac{1}{3B} \sum_{k,s} \left(-\frac{\partial \hbar\omega_s(k)}{\partial V}\right) \frac{\partial}{\partial T} \left(\frac{1}{e^{\beta\hbar\omega_s(k)}-1}\right) \tag{5}$$

Similarly, other thermodynamic properties i.e., the specific heat capacity is also a function of phonons. The specific heat capacity at constant volume is given by sum of individual phonon modes as

$$C_V = \sum_{k,s} \left(\frac{\hbar\omega_s(k)}{V}\right) \frac{\partial}{\partial T} \left(\frac{1}{e^{\beta\hbar\omega_s(k)}-1}\right) \tag{6}$$

Here, the distinction can be made of specific heat capacity at low and high temperature from the temperature derivative of phonon population in above equation. At low temperature, according to Bose-Einstein equation the phonon population $\left(n = \left(e^{\beta\hbar\omega_s(k)} - 1\right)^{-1}\right)$ only contains contributions from the acoustic modes so the exact formulation of density of states can be evaluated simply by considering a spherical shell volume in radius k and $k + dk$ in reciprocal space and provided that the acoustic modes follow linear dependence on wave vector ($\omega = ck$), where c is velocity of sound[24].

$$g(\omega) = \frac{3V}{2\pi^2 c^3}\omega^2 \tag{7}$$

The validity of the above relation holds within the theory of harmonic lattice vibration. This density of states contributes to the total energy of phonons and further specific heat capacity of ordered crystalline solid at low temperature. Thus, the heat capacity is written in the form

$$C_V = \frac{2V\pi^2 k_B}{5\left(\frac{c\hbar}{k_B}\right)^3} T^3 = N\frac{12\pi^4 k_B}{5}\left(\frac{T}{\theta_D}\right)^3 ; \theta_D = \left(\frac{c\hbar}{k_B}\right)\left(\frac{6\pi^2 N}{V}\right)^{\frac{1}{3}} \tag{8}$$

Where, θ_D is the Debye temperature. In what follows from the above equation that the heat capacity at low temperature varies as T^3. This relation establishes the fact that in metals the linear variation of heat capacity with temperature can be extracted from the phonon contribution to the heat capacity. Also, deeper understanding of thermodynamics of amorphous materials not following T^3 law for specific heat can be understood taking this as a reference[24].

Density Functional Theory

As I discussed above in section thermal properties of crystalline solid that to successfully describe the thermal properties at least on the context of crystalline solid one would essentially need to account for the anharmonic corrections in the potential energy terms. Now, up to this point only lattice vibration i.e., the vibration due to atoms are considered to discuss the thermal properties of crystalline solid. However, the state of electron also plays significant role in determining the thermal properties in a crystalline solid. In the formalism of density functional, the ground state and other properties for the system of electrons can be determined from electron distribution alone. In 1927, Hartree devised a method to evaluate approximate wavefunction and energies for atoms and in the same year Thomas and Fermi proposed a statistical model to compute the energy of atoms by approximating the distribution of electrons in an atom[25]. The key idea here was to approximate the kinetic energy expression in Hamiltonian (total energy) by the functional of electron density and add two classic terms of nuclear-electron and electron-electron interactions (these can be represented in terms of electron density) to compute the atom energy. Later, Dirac added the exchange energy correlation functional to account for the Pauli principle. In 1964, Hohenberg and Kohn finally formulated the density functional theory that turned complicated many electron wavefunction which contains $3N$ (N being number of electrons for 3 spatial variables) variables into 3 spatial variables[26]. The reduction of this many body problems came only year later by Kohn and Sham by simplifying multi-electron problem into a problem of non-interacting electrons in an effective potential which includes interaction between electrons, the exchange and correlation interactions[25]. The total energy of an N_{el} electrons and N_{at} atoms is given by the following equation

$$H = T_N + T_e + V_{N-N} + V_{e-e} + V_{N-e} \tag{9}$$

Herein, T_N represents the kinetic energy for the nuclei, T_e the kinetic energy for electrons, V_{N-N} the potential energy for nucleus-nucleus interaction, V_{e-e} the potential energy for electron-electron interaction, V_{e-e} the potential energy for nucleus-electron interaction. Each representing energy in the above given equation are

$$T_N = -\sum_{\alpha}^{N_{at}} \frac{\hbar^2}{2M_\alpha}\nabla^2; T_e = -\sum_{i=1}^{N_{el}} \frac{\hbar^2}{2m}\nabla^2;\ V_{N-N} = \frac{1}{2}\sum_{\alpha=1}^{N_{at}} \sum_{(\alpha\neq\beta)=1}^{N_{at}} \frac{Z_\alpha Z_\beta e^2}{4\pi\epsilon_0 |R_\alpha - R_\beta|}; V_{e-e}$$

$$= \frac{1}{2}\sum_{i=1}^{N_{el}} \sum_{(i\neq j)=1}^{N_{el}} \frac{e^2}{4\pi\epsilon_0 |r_i - r_j|}; V_{N-e} = -\sum_{i=1}^{N_{el}}\sum_{\alpha=1}^{N_{at}} \frac{Z_\alpha e^2}{4\pi\epsilon_0 |R_\alpha - r_i|}$$

According to Hohenberg-Kohn, the Hamiltonian can be written in terms of electron density as[27]

$$E_{HK}[n] = T[n] + E_{int}[n] + \int drV_{ext}(r)n(r) + E_{II}$$

$$= F_{HK}[n] + \int dr\, V_{ext}(r)n(r) + E_{II} \tag{10}$$

Here, the kinetic energy T_N and T_e are fused to written in the expression $T[n]$ $M_\alpha, m, R_\alpha, R_\beta, r_i$ are the mass of nucleus, mass of electron, position of α nucleus, position of β nucleus and position of electron. The core-core repulsion is represented as external potential by the term $\int dr\, V_{ext}(r)n(r)$ and any other term accounting Hamiltonian in the energy E_{II}. By the Hohenberg-Kohn assumption that the system is still interacting meaning that the interaction between nucleus-nucleus and electron-electron are still part of Hamiltonian formulation. It is still $3N(= N_{el} + N_{at})$ number of variables to account for. Since, considering the system as non-interacting the coupled Schrodinger equation of 3N variable can be now separated into 3 variables. This is because each energy for the electron and nucleus can be added to get the total energy. The Hamiltonian now then be written as[28]:

$$E_{KS} = T_s[n] + \int dr\, V_{ext}(r)n(r) + E_{Hartree}[n] + E_{II} + E_{XC}[n] \tag{11}$$

Where, the Hartree energy is given by:

$$E_{Hartree}[n] = \frac{1}{2}\int dr \frac{dr'n(r)n(r')}{|r-r'|} \tag{12}$$

Unlike energy expression $T[n]$ in Hohenberg Kohn which is interacting, the kinetic energy of electron and nucleus $T_s[n]$ in this system is non interacting and other forms of energy is embedded into Hartree energy $E_{Hartree}[n]$ and E_{II}. Also, energy due to spin for electron is considered in the energy $E_{xc}[n]$, the exchange correlation energy.

Ab-initio Molecular Dynamics

The problem of motion of electron and nucleus is ab-initio molecular dynamics. This is the application to density functional theory to solve time evolution of electronic wave functions under potential energy surface. The above energy expressions from density functional theory constitutes the nuclear wave functions that are coupled to the electronic wave functions and are too complex to be solved directly. Therefore, some approximation has to be applied to the calculation of Hamiltonian (H) that would substantially reduce the complexity in terms of number of variables to solve.

Adiabatic and Born-Oppenheimer approximation assumes that the electron is very small compared to that of nucleus and immediately follows the nuclear motion or the potential energy surface[29]. This approximation leads to immediate results for the Hamiltonian that the nucleus is decoupling from electrons that means the electronic and nuclear motions are separable and there is no exchange of energy between electrons and nuclei. Therefore, equation (9) becomes

$$H = T_e + V_{e-e} + V_{n-e} + V_{n-n} \tag{13}$$

Here, H is the Hamiltonian of a system at ground state. Now this Hamiltonian determines the time evolution of quantum mechanical state of electron-nucleus system $\Phi(r, R; t)$ through time dependent Schrodinger equation as

$$i\hbar \frac{\partial}{\partial t} \Phi(r, R; t) = H\Phi(r, R; t) \tag{14}$$

Since, this quantum mechanical state can be decoupled to individual electronic and nuclear state by Born-Oppenheimer approximation as

$$\Phi(r, R; t) = \Psi(r, R)\chi(R; t) \tag{15}$$

It is worth to mention that relative comparison has been made considering the size of nucleus and electron. Following the nuclear state of motion, the electronic state of motion is given by $\Psi(r, R)$ and nuclear motion by $\chi(R; t)$ in above equation (15). Hence, from equation (14) and (15) one can solve the evolution of electronic state under this assumption using Hamiltonian constructed from density functional theory. The solution obtained for evolution of nuclear-electron system is entirely quantum mechanical up to this point and is not in the realm of classical molecular dynamics. Now, further assumption made by Ehrenfest states that the nuclear motion is semiclassical in a sense that the nuclei are relatively heavy, and a good approximation can be made considering the average nuclear motion instead of instantaneous nuclear motion which is a Newtons equation of motion[29]. This assumption leads the evolution of nuclear-electron state in any material into the problem of classical molecular dynamics but the Hamiltonian or energy still from the density functional theory and thus the name ab initio molecular dynamics. The equation of motion for ab initio molecular dynamics is then given by[29]

$$M_\alpha \frac{d^2 R_\alpha}{dt^2} = -\nabla_\alpha \langle \Phi | H | \Phi \rangle \ (16)$$

Where, M_α is the mass of nucleus at α and the operator $\nabla_\alpha = \frac{\partial}{\partial R_\alpha}$. The $\langle \Phi | H | \Phi \rangle$ is bra-ket notation given by $\langle \Phi | H | \Phi \rangle = \int dr \Phi^*(r) H \Phi(r)$.

The construction of Born-Oppenheimer molecular dynamics is due to the approximation by Born-Oppenheimer and Ehrenfest[29]. In Born-Oppenheimer molecular dynamics, the electronic wave function is in its ground state, the orthogonality is enforced for time evolution of electronic wave function with Lagrange multiplier[29]. This condition is a physical requirement for the set of orbitals in order to be able to compute real and observable quantities[29]. The Lagrange multiplier has a special importance in this dynamic in a sense that the multiplier builds up validation of antisymmetric function of orbitals namely the wave functions associated with the individual electrons. The Lagrange multiplier is given by[29]

$$L^{BO} = \frac{1}{2} \sum_\alpha M_\alpha \dot{R}_\alpha^2 - \langle \Psi_0 | H | \Psi_0 \rangle + \sum_{i,j} A_{ij} \left(\langle \psi_i | \psi_j \rangle - \delta_{ij} \right) \quad (17)$$

The first term in Lagrange multiplier is the kinetic energy of the nuclei, the second term corresponds to the Hamiltonian from Erhenfest, and Born-Oppenheimer approximation and the last term is a Lagrange function that address the orthonormality of the orbitals by introducing the multiplier A_{ij}. The electron obeys Pauli Exclusion principle and follow Fermi-Dirac statistics. Thus, the electronic wave function is an antisymmetric function of its orbitals of individual electrons. In above equation (17), Lagrange solves the associated equation of motion from Euler-Lagrange equation for nuclear and electronic degrees of freedom. For nuclear degrees of freedom, the equation of motion is given by:

$$\frac{d}{dt}\frac{\partial L}{\partial \dot{R}_\alpha} - \frac{\partial}{\partial R_\alpha} = 0 \tag{18}$$

Similarly, for electronic degrees of freedom, the equation of motion is given by

$$\frac{d}{dt}\frac{\delta L}{\delta \psi_i^*(r)} - \frac{\delta L}{\delta \psi_i^*(r)} = 0 \tag{19}$$

So, to sum up the nuclear equation of motion for Born-Oppenheimer molecular dynamics can be written as[29]

$$M_\alpha \ddot{R}_\alpha(t) = -\frac{\partial}{\partial R_\alpha} \min_{\psi} \langle \Psi_0 | H | \Psi_0 \rangle \tag{20}$$

And for electronic equation of motion as

$$H\psi_i(r) = \sum_j A_{ij}\psi_i(r) \tag{21}$$

Now, above Born-Oppenheimer molecular dynamics includes the orbital orthonormality of electronic wave function through Lagrange multiplier[29]. The inclusion of orthonormality essentially forms the antisymmetric wavefunctions which is Pauli exclusion state. However, the Born-Oppenheimer molecular dynamics does not state approximation of antisymmetric electronic wavefunction[29]. Hartree-Fock molecular dynamics approximate the antisymmetric electronic wave function by single determinant also known as Slater determinant of the electronic orbitals $\psi_i(r_i)$ by[29]

$$\Psi = \frac{1}{\sqrt{N!}}\, det \begin{bmatrix} \psi_1(r_1) & \psi_1(r_2) & \cdots & \psi_1(r_N) \\ \psi_2(r_1) & \psi_2(r_2) & \cdots & \psi_2(r_N) \\ \vdots & \vdots & \ddots & \vdots \\ \psi_N(r_1) & \psi_N(r_N) & \cdots & \psi_N(r_N) \end{bmatrix} \tag{22}$$

In here, two operator associates electronic interaction, the first one is the coulomb operator that corresponds to electrostatic interaction between the orbitals as in

$$\mathcal{L}_j(r)\psi_i(r) = \left[\int dr' \psi_j^*(r') \frac{1}{\|r-r'\|} \psi_j(r')\right] \psi_i(r) \tag{23}$$

The second operator is the exchange operator that represent exchange energy as a result of Pauli Exclusion principle as in

$$\mathcal{K}_j(r)\psi_i(r) = \left[\int dr'\psi_j^*(r')\frac{1}{\|r-r'\|}\psi_i(r')\right]\psi_j(r) \tag{24}$$

The identification of the coulomb and exchange operator in Hartree-Fock molecular dynamics provides more precision to that of Born-Oppenheimer molecular dynamics. With these operators added the Hamiltonian is now rewritten as

$$H^{HF} = T_e + V_{n-n} + 2\sum_j \mathcal{L}_j(r) - \sum_j \mathcal{K}_j(r) \tag{25}$$

Now, the Hamiltonian in equation (25) determines the Lagrangian for the electronic wavefunction by

$$\mathcal{L}^{HF} = -\langle\Psi_0|H^{HF}|\Psi_0\rangle + \sum_{i,j} A_{ij}\left(\langle\psi_i|\psi_j\rangle - \delta_{ij}\right) \tag{26}$$

The equation of motion is obtained similarly to equations (18)-(24) with Lagrange defined in (26). After Hartree-Fock molecular dynamics, several other abinitio molecular dynamics techniques were developed. Those methods efforts were aimed at correctly predicting the Hamiltonian by integrating energy from Kohn-Sham and exchange correlation[29]. Car-Parrinello molecular dynamics is the most sophisticated technique currently being used in many abinitio molecular dynamics calculation software. Car-Parrinello molecular dynamics uses a version of the equation of motion that is similar to Born-Oppenheimer and Hartree-Fock molecular dynamics. However, such approaches do not take electron dynamics into account, resulting in electronic orbitals that are not complex molecular fields. As a result, by introducing a fictitious electronic kinetic energy concept, this approach incorporates the complex essence of electronic degrees of freedom[29]. With the additional assumption of including dynamic nature of electrons the extended Lagrangian in Car-Parrinello molecular dynamics is given by

$$\mathcal{L}^{CP} = \frac{1}{2}\sum_\alpha M_\alpha \dot{R}_\alpha^2 + \sum_i \mu\langle\dot{\psi}_i|\dot{\psi}_i\rangle + \langle\Psi_0|H^{KS}|\Psi_0\rangle + \sum_{i,j} A_{ij}\left(\langle\psi_i|\psi_j\rangle - \delta_{ij}\right) \tag{27}$$

Where, μ acts as a fictitious electronic mass of inertia and H^{KS} is the Hamiltonian due to Kohn-Sham approximation. Therefore, the nuclear and electronic equation of motion are given by[29]

$$M_\alpha \ddot{R}_\alpha = -\frac{\partial}{\partial R_\alpha}\langle\Psi_0|H^{KS}|\Psi_0\rangle + \sum_{i,j} A_{ij}\frac{\partial}{\partial R_\alpha}\langle\psi_i|\psi_j\rangle \tag{28}$$

$$\mu\ddot{\psi}_i(t) = -H^{KS}\psi_i(t) + \sum_j A_{ij}\,\psi_j(t) \tag{29}$$

Molecular Dynamics Simulation

Molecular dynamics or classical molecular dynamics is another method for simulating solids (MD). The advantage is that it can handle particle numbers many orders of magnitude larger than ab initio approaches in a fraction of the time. Physical science can reliably predict a system's behavior if it is given adequate starting details. Furthermore, if all related mechanisms are understood, it can predict exact future actions. The above argument is exemplified by classical mechanics[30]. With the mass, position, and velocity of an object, Laplace determined the object's eternal trajectory by referring to the Newtonian equation of motion. The Newtons equation of motion is simply given by

$$m_i\frac{\partial^2 r_i}{\partial t^2} = F_i \text{ and } F_i = -\frac{\partial U(r_1, r_2, \ldots, r_n)}{\partial r_i} \tag{30}$$

Here, m_i is the mass of ith particle and r_i is the position of ith particle. The derivative of potential U is used to calculate the force F_i. The trajectory of any particle can be deterministically predicted if the right potential U is known. And there are n simultaneous differential equations to solve. The above equation becomes a bit more complex in reality. Rather than attempting a series of different equations, one normally integrates over a timestep, adjusting the location and velocity as needed. It is given by the equation

$$-m_i\frac{dv_i}{dt} = \sum_j F_2(r_i, r_j) + \sum_j\sum_k F_3(r_i, r_j, r_k) + \cdots \tag{31}$$

Here, $v_i = dr_i/dt$. F_2 denotes the force between two atoms, and F_3 denotes the force between three atoms, and so on. This topic is much more complex than it seems because of the increasing number of summations in each force. Despite the complexity involved in equation (31) the molecular dynamics system always works since the system will eventually settle into equilibrium under external force and we can describe any macroscopic event for each of the atoms present. Furthermore, the system is ergodic meaning that the system can reach any microstate given a large enough time. The ergodicity states that regardless of time some fundamental properties of time do not change like the total energy of system and number of particles in the system due to periodic boundary condition. The set of observables or parameters which does not change over time are called ensembles. We can evaluate canonical ensembles with a variety of conditions using MD simulations, including constant volume, controlled pressure (variable volume), and controlled temperature. The temperature demands further care because it is difficult to regulate. The particles velocity must be taken into account. The thermostat is responsible for maintaining a given constant temperature. For a given system, if the temperature is too high then the thermostat extract heat from the system and if the temperature is too low than the desired value, the thermostat supply heat to the system from outside.

Now the temperature in molecular dynamics simulation is given by

$$\frac{KT_{MD}}{2} = \frac{1}{6N} \sum_{i=1}^{N} \sum_{j=1}^{3} m_i v_{ij}^2 \frac{dr_i}{dt} \qquad (32)$$

The implication of equation (32) is that the temperature of a system can be regulated by controlling the average velocity of the system under proper distribution. Initial temperature can be set by assigning random velocities that match the Maxwell Boltzmann Distribution. Then, for the next move, Andersen's simple scheme can be followed[31]. For each time, the heat bath interacts with one particle, according to this scheme. The particle's velocity is then re-assigned at random using the Gaussian distribution. As the device exceeds the target temperature, the frequency collision becomes a factor in the speed of convergence. By adding the additional force as a function of time, the Langevin scheme overcomes this constraint. It functions as a noise. However, this system has the downside of sometimes over-correcting. The Nose-Hover reduces the over correction by extending the Hamiltonian or the energy by introducing heat bath which is given by[32]

$$H_{NH} = \sum_i \frac{m_i v_i^2}{2s^2} + U(r, q) + \frac{P_s^2}{2Q} + LKT \log(s) \qquad (33)$$

In equation (33), p_s is the momentum of heat bath and Q is the fictious mass. s is the scaling parameter and L essentially is number of degrees of freedom. The equations that need to solve above equation (33) are given by

$$\dot{r}_i = \frac{m_i v_i}{s}, \qquad \dot{v}_i = -\frac{1}{m}\frac{\partial U}{\partial r_i}, \qquad \dot{s} = \frac{p_s}{Q} = \frac{Lk\left(T - T_{target}\right)}{Q}, \qquad \dot{p}_s = \sum_i m_i s \dot{r}_i^2 - LkT \qquad (34)$$

Now to evaluate the time integral equation of motion, the position of the particle at time $t + \Delta t$ is given by

$$r_i(t + \Delta t) = r_i(t) + \dot{r}_i(t)\Delta t + \frac{1}{2}\,\ddot{r}_i(t)\Delta t + \frac{1}{2}\,\ddot{r}_i(t)\Delta t^2 + O(\Delta t^3) \qquad (35)$$

The equation (35) can also be rewritten using central difference formula using finite difference by

$$r_i(t + \Delta t) \approx 2r_i(t) - r_i(t - \Delta t) + \frac{F_i(t)}{m_i}\,\Delta t^2 + O(\Delta t^3) \qquad (36)$$

The algorithm above for equation (35) and (36) is also known as Verlet algorithm and have been mostly used for calculation position and force for the next time step. However, calculation of force expression become complicated so, separating long and short-range force greatly reduce the computational complexity. Considering the interaction of up to certain cutoff radius for nearest neighbor interaction also helps to reduce the computational complexity. Another is to be mindful of the length scale and time restrictions. It would only take a few nanoseconds to complete a million-step run. Furthermore, the number of atoms is restricted to millions. This problem can be mitigated by using periodic images for homogeneous systems. The Verlet algorithm's inherent parameter is the size of the timestep. The calculation would take longer if smaller time step were used. Finally, I will talk about atomic interactions. Since it requires instantaneous electron change, classical molecular dynamics requires potential energy. As a result, no chemical bond breaking, or formation is needed in the simulation.

Most significantly, potential energy is needed to run classical molecular dynamics. This could be done by fitting experimental data or ab-initio calculations into the appropriate relationships for parameters including volumes, strain, and many other mechanical properties. This is a time-consuming process, and the availability of potential for several elements is more difficult. Things get complicated when there are more than two components in a scheme. And since this mechanism is highly dependent on the input data, one possibility for a structure made up of the same elements but with different structures may not function satisfactorily outside of its original crystal structure or outside of targeted property. This is referred to as transferability, and it is also a top priority when it comes to developing potential energy. The aim of this research is to develop the interatomic potential for zirconium diboride for classical molecular dynamics.

Having discussed the techniques being applied in ab-initio molecular dynamics and molecular dynamics simulation, the ab-initio molecular dynamics while being very precise in simulating system of materials it cannot simulate more than hundreds of atoms and the computational cost significantly increases with each atom increasing in the system. Also, the simulation cannot exceed more than femtoseconds to picoseconds. The schematic diagram for simulating different simulation is given in the Figure 5 below.

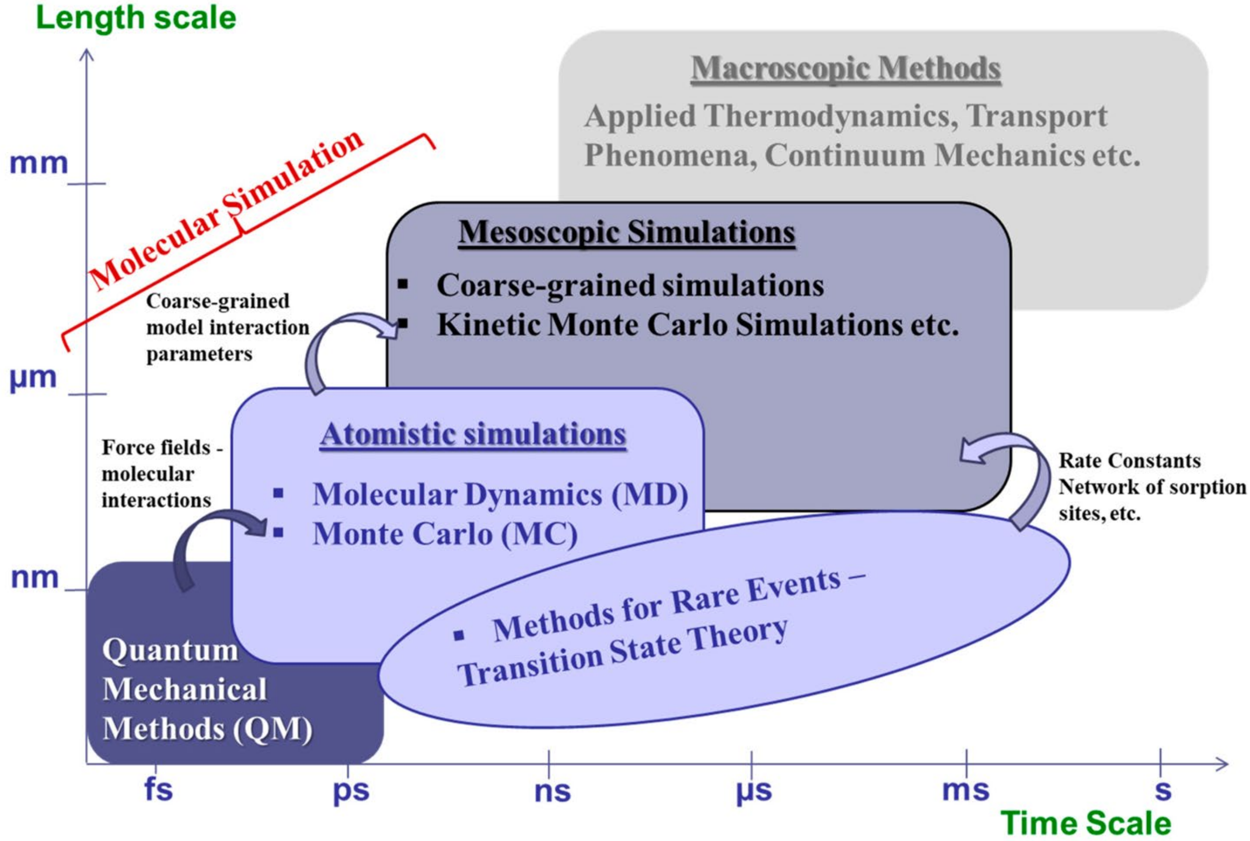

Figure 5: Schematic diagram showing different simulation in time and length scale.

The benefit of atomistic simulation like molecular dynamics and Monte Carlo is that we can simulate millions of atoms with simulation size up to micrometer and time length from femtoseconds to nano or microseconds as compared to the quantum mechanical or ab-initio molecular dynamics simulation. Simulating in the larger scale allow us to mimic the experimental observation and help us to understand the fundamental principle. Several other techniques like mesoscopic simulation and other macroscopic simulation exist but the precision is compromised and that also depend on one or other way to atomistic scale.

Interatomic Potentials for Molecular Dynamics Simulation

As I discussed in above section that the interatomic potential is a key ingredient for us to be able to perform molecular dynamics simulation for greater time scale and size, and explore different properties of materials like thermal or mechanical properties or to study the behavior of materials at different conditions like temperature, pressure, strain etc. The development of interatomic potential is entirely on the interest of which properties of material to fit or reproduce. Also, the development of potential also depends on the choice of material. There are several types of interatomic potential for classical molecular dynamics for wide range of materials available.

From the ab-initio molecular dynamics simulation and molecular dynamics simulation it is quite obvious the approximations and measures taken to perform molecular dynamics simulation for the purpose of determining several material properties in large scale. What I meant by interatomic potential is embedded on how the approximations of Hamiltonian are made and relative treatment of electron and nucleus by Born-Oppenheimer from above sections. Starting from equation (15) that the electronic and nuclear motion are separable and, the electronic wave function depends on atomic positions only, we can write total many-body state by $|\Phi\rangle = |\Psi(\mathrm{R}_1, R_2, \ldots, R_{N_{at}}\rangle|\chi\rangle$. So, the problem of coupled electronic and nuclear Hamiltonian system can be decoupled as

$$\widehat{H}_{el}|\Psi\rangle = E_{el}(R_1, R_2, \ldots, R_{N_{at}})|\Psi(R_1, \ldots, R_{N_{at}}\rangle \tag{37}$$

$$\widehat{H}_{at}|\chi\rangle = \left[E - E_{el}\left(R_1, \ldots, R_{N_{at}}\right)\right]|\chi\rangle \tag{38}$$

Here, $\widehat{H}_{el} = T_{e-e} + V_{e-e} + V_{n-e}\,(R_1, \ldots, R_{N_{at}})$ and $\widehat{H}_{at} = T_{n-n} + V_{n-n}$ are the Hamiltonian in the electron and nuclear system. Through the nucleus-electron interaction, the electronic

Hamiltonian and thus the electronic eigen equation are still parametrically depending on the atomic positions. Equation (38) can be rewritten as follows in coordination space.

$$\left[-\sum_{\alpha=1}^{N_{at}} \frac{\hbar^2}{2M_\alpha} \nabla_{R_a}^2 + V_{IAP}(R_1, \dots, R_{N_{at}})\right] \chi = \mathrm{E}\chi \tag{39}$$

Herein, $V_{IAP}(R_1, \dots, R_{N_{at}})$ is the interatomic potential that contains pair interaction and repulsive Coulomb interaction between all nuclei and electrons and is given by

$$V_{IAP}\left(R_1, \dots, R_{N_{at}}\right) = \frac{1}{2} \sum_{\alpha,\beta} \frac{Z_\alpha Z_\beta}{|R_\alpha - R_\beta|} e^2 + E_{el}(R_1, \dots, R_{N_{at}}) \tag{40}$$

So, in simpler terms the interatomic potential is the pair interaction or nuclear potential and possible Coulombic interaction associated with all electrons and nucleus. The energy due to possible electron-electron or nucleus-nucleus interaction is determined through rigorous density functional or ab-initio molecular dynamics calculation. The interatomic potential can be determined in theory by solving the electronic Schrodinger equation for the desired atomic positions. The electronic Schrödinger equation describes an electronic many-body structure that can be solved using ‘ab initio' techniques including Density Functional Theory (DFT), Hartree Fock (HF), Configuration Interaction (CI), and Coupled Cluster Analysis (CCA) (CC)[33, 34]. All of these ab initio techniques produce parametric N_{el} Self-Consistent Field (SCF) equations based on atomic positions. The time it takes to solve these SCF equations grows exponentially with the number of electrons in the device, making these techniques easily unmanageable. This is where semi-empirical approaches come into play. In these methods, the Inter Atomic Potential (IAP) is essentially fitted to experimental or ab initio results.

The total energy of interatomic interaction of the N_{at}-atom system can also be extended in summations over many body terms in interatomic potential theory. The total energy is given by

$$E_{tot} = E_0 + \frac{1}{2!} \sum_{\alpha,\beta} V_2(R_\alpha, R_\beta) + \frac{1}{3!} \sum_{\alpha,\beta,\gamma} V_3\left(R_\alpha, R_\beta, R_\gamma\right) + \cdots \tag{41}$$

Here, E_0 stands for the reference energy (which is ignored in the following), and V_n stands for the n-body interatomic potential function. Pair potentials are used when only pair interactions are included, and cluster potentials are used when higher order interactions are included. Pair potentials are usually used to model a small number of atomic rearrangements and have a restricted range of application. The addition of higher order interactions to cluster potentials improves on pair potentials. Angles between bonds are defined in three body and higher order terms, which are not present in pair potential descriptions. Cluster potentials are typically truncated at the three-body level in operation. Cluster potentials can accommodate a wider variety of atomic configurations than pair potentials, but they still fall short of offering a detailed definition of E_{tot}. Using cluster potentials instead of pair potentials comes at a large cost in terms of computation time. The total energy E_{tot} can also be expanded in terms of functional by:

$$E_{tot} = E_0 + \frac{1}{2}\sum_{\alpha,\beta} V_2\left(R_\alpha, R_\beta\right) + \sum_\alpha F\left[\sum_\beta g_2(R_\alpha, R_\beta) \sum_{\beta,\gamma} g_3(R_\alpha, R_\beta)\ R_\gamma \ldots\right] \tag{42}$$

Here in the above equation (42), the higher order interactions are expressed as a functional F of cluster terms g_n, rather than the total energy of interatomic interactions as a sum of pairs and higher. The functions g_n are set of function that represent the local environment and the functional F describe how the energy is influenced by g_n in an atom. The cluster functionals are thought of when higher order interactions are accounted for. As a result, pair functionals generalize pair potentials and provide a much more precise description of inhomogeneous environments. When a cut-off radius is applied, the computational speed is comparable to the pair potential. Cluster functionals are similar to cluster potentials in that they generalize them. By explicitly using angular forces in the functions describing the local context, cluster functionals build on the precision of pair functionals. In addition, they can accommodate a broader range of inhomogeneous environments than cluster potentials. Since the atomic geometries can still be visualized at these stages, and the computation time is significantly less than for higher order treatments, cluster functionals are normally limited to the three and four body levels. Depending on the number of interactions, the interatomic potentials can be categorized as pair interactions-pair interactions consist of pair potentials and pair functionals and cluster interactions-consisting of cluster potentials and cluster functionals.

The most common type of interaction also known as pair interaction is always available in cluster interactions. Many common types of pair interactions or pair potentials exist that has a various mathematical formulation. For instance, repulsive wall potentials are used to model repulsive interaction that is more prominent at small interatomic separation i.e., less than 1 Å. These types of potentials are mostly used in the simulation of collision of energetic particles. There are several modifications in repulsive wall potentials based on fitting function in it and is given by

$$V(r) = \frac{Z_1 Z_2}{4\pi\epsilon_0 r}\,\chi(x) \qquad (43)$$

Here, $x = r/a_0$ and $a_0 = 0.8853 a_B \bar{Z}^{-\frac{1}{3}}$. The quantity a_B is Bohr radius and $\bar{Z}^{-\frac{1}{3}} = \left(Z_1^{\frac{1}{2}} + Z_2^{\frac{1}{2}}\right)^{-\left(\frac{2}{3}\right)}$ [35]. $\chi(x)$ is the fitting function in equation (43). Moliere, krypton-carbon and ZBL repulsive potential use the exponential type of fitting function like[36]

$$\chi(x) = \sum_{i=1}^{4} a_i e^{-b_i x} \qquad (44)$$

Here, a_i, b_i are the fitting parameters. While Lenz-Jenson repulsive potential use other types of fitting parameters given by[37]

$$\chi(x) = e^{-q}\left(1 + \sum_{i=1}^{4} a_i q^i\right); q = 3.11126\sqrt{x} \qquad (45)$$

Similarly, other type of pair interaction, also attractive well potentials explain attractive interaction between atomic pairs. At particle separations of around $1 - 4$ Å, these types of potentials define the attractive part of the interaction potential. These types of potentials have a very small range of applicability, which is a major disadvantage. For example, they can only describe crystal structures that are tightly packed. The Lennard-Jones and Morse potentials are the most commonly used and is given by the following equations[38, 39]:

$$V(r) = 4\epsilon\left[\left(\frac{\sigma}{r}\right)^{12} - \left(\frac{\sigma}{r}\right)^{6}\right] \tag{46}$$

$$V(r) = \frac{D_e}{S-1}\left[e^{-(2S)^{\frac{1}{2}}\beta(r-R_e)} - Se^{-\left(\frac{2}{S}\right)^{\frac{1}{2}}\beta(r-R_e)}\right] \tag{47}$$

The Lennard-Jones potential was developed to describe noble gases, and it is based on the assumption that atoms in a solid noble gas are only slightly skewed from their stable electronic closed-shell configuration in the free state. Dipole interactions are proportional to r^{-6} when small distortions in the electronic closed-shell structure occur. The Van Der Waals forces between closed shell atoms are the product of these interactions. While for Morse potential, the parameter D_e is the dimer energy, R_e the equilibrium displacement and β is usually fitted for bulk modulus.

Now, the cluster potential is achieved by extending pair potential by including angular contributions. Among different forms of cluster potential, the simplified form of this potential by Tersoff implement environment dependent bond order or to say the information regarding bond angle or dihedrals[40]. Such potential is given by the equation

$$V(R_{\alpha\beta}) = f_C(R_{\alpha\beta})[a_{\alpha\beta}f_R(R_{\alpha\beta}) + b_{\alpha\beta}f_A(R_{\alpha\beta})] \tag{48}$$

Herein, $R_{\alpha\beta}$ is the distance between atoms α and β. A repulsive pair potential is represented by the function f_R, while an attractive pair potential is represented by the function f_A. The extra term f_C is just a smooth cut-off feature that limits the potential's range. The coefficient b now becomes a function of the local environment, which is the only new aspect of this potential. It is thought to be a monotonically decreasing property of atom coordination and represents a measure of bond order. The parameter $a_{\alpha\beta}$ represents range-limiting terms. For the attractive and repulsive potential in above equation (48), the exponential function is used and for the cutoff function F_C, a step function in the form of sine is taken for certain cutoff range. The parameter $b_{\alpha\beta}$ contains the angular information i.e., the bond angle between atom pairs $\alpha\beta$ and say other atom pairs $\alpha\gamma$.

Embedded Atom Method Interatomic Potential

The Hohenberg and Kohn theorem states that the total electron density uniquely determines the external potential up to an additive constant, and vice versa[27]. The Embedded Atom Method (EAM) has its origins in density functional theory. The Stott-Zaremba corollary, as a result of this theorem, can be stated as follows: 'The embedding energy of an impurity is calculated by the electron density of the host system before the impurity is added'[41]. The statement can be explained as follows: the electron density of an unaffected host determines its potential. If an impurity is added in the system, the total potential is then the sum of the potentials of the host and the impurity. Thus, the energy of the host with impurity is a function of the host and impurity potentials. The location and charge of the impurity nucleus determine the host electron density and impurity potential. So, the energy of the host with impurity is a function of the unaffected host electron density as well as the impurity form and position. The total energy can be expressed as follows:

$$E = \mathcal{F}_{Z,R}[\rho_h(r)] \quad (49)$$

Here, $\rho_h(r)$ represent the unperturbed electron density of the host, Z and R are type and position of the impurity. The functional form $\mathcal{F}$ is not known and is independent of host but is universal.

Assuming that the energy depends only on the minimal environment immediately surrounding the impurity, or that the impurity encounters a locally uniform electron density as a basic approximation[42]. This simplification can be thought of as either a local approximation or the lowest order term involving the density's successive gradients. Since the assumption is that the energy only depends on limited environment around the impurity, so the impurity only has local electron density which is also the lowest order term that involve the successive gradient of density.

Each atom in embedded atom method can be viewed as impurity in the host so the total energy can be written as:

$$E = \sum_\alpha F_\alpha[\bar{\rho}_\alpha] \qquad (50)$$

Here, F is the embedding energy and $\bar{\rho}_\alpha$, the uniform density of host at position R_α without atom α. It is to note that the embedding function F and the functional $\mathcal{F}$ are not the same thing. The concept of extreme locality, or total uniformity of the electron gas and background, results in unreasonable values for the electron gas or electron density in equation (50). A core-core repulsion must be added to accurately explain the energy, which is presumed to take the form of a short-range pairwise repulsion between cores here. With addition of core-core repulsion for a certain cutoff, the EAM energy is further improved so the total energy is given by

$$E_{tot} = \frac{1}{2}\sum_{\alpha,\beta} V(R_{\alpha\beta}) + \sum_\alpha F[\bar{\rho}_\alpha] \qquad (51)$$

Here, $V(R_{\alpha\beta})$ is the core-core repulsion, $F[\bar{\rho}_\alpha]$ is embedding function and, $\bar{\rho}_\alpha$ the electron density given by

$$\bar{\rho}_\alpha = \sum_\beta \rho(R_{\alpha\beta}) \qquad (52)$$

In general, $F[\bar{\rho}_\alpha]$ the embedding function has no specific form and is entirely dependent on the fitting procedure. Several embedding functional have been proposed. For example, the Tight

Binding Model for second moment approximation use the form $F[\rho] = -A\rho^{\frac{1}{2}}$. Daw and Baskes, used the density form to evaluate embedding functional for the fitting procedure given by the equations[43]

$$\rho(R_{\alpha\beta}) = \frac{Z_\alpha Z_\beta}{R_{\alpha\beta}}\ ; Z(r) = Z_0(1 + \gamma r^\kappa)e^{-\nu r} \tag{53}$$

Here, γ, κ and ν are adjustable parameters and Z_0 the number of valence electrons. Similarly, the density function by Voter-Chen use $\rho(r) = r^6(e^{-\beta r} + 2^9 e^{-2\beta r})$ for embedding function evaluation. Further, the electron density function used by Foiles is given by

$$\rho(r) = r^8(e^{-\beta r} + 2^{11} e^{-2\beta r}) \tag{54}$$

Now, instead of using electron density to determine the embedding functional, Johnson came with a universal form for the embedding functional given by[44]

$$F[\rho] = -F_0\left[1 - n\ln\left(\frac{\rho}{\rho_{eq}}\right)\right]\left(\frac{\rho}{\rho_{eq}}\right)^n \tag{55}$$

Here, ρ_{eq} is the equilibrium value of the electron density ρ and F_0 and n can be determined by

$$F_0 = E_c - E_f \tag{56}$$

$$n = \sqrt{\frac{\Omega B}{A\beta^2 E_f}} \tag{57}$$

In equations (56) and (57), the parameter E_c and E_f are the cohesive energy and monovacancy formation energy. Ω is the equilibrium atomic volume, B the bulk modulus and $A = 2C_{44}/(C_{11} - C_{12})$ the anisotropic ratio. Similarly, the density function for the Johnson is given by

$$\rho(r) = \rho_e\left(\frac{r_1}{r}\right)^\beta \tag{58}$$

Here, ρ_e is atomic electron density at the nearest neighbor.

Reference Free Modified Embedded Atom Method Interatomic Potential

The reference free modified embedded atom method (RF-MEAM) potentials are derived from the MEAM formalism where the energy E for a given system of N atoms in the RF-MEAM is represented by[45-47]:

$$E = \sum_{i=1}^{N} E_{\alpha_i}^{emb}(\rho_i) + \frac{1}{2}\sum_{i\neq j}^{N} \phi_{\alpha_i,\alpha_j}(r_{ij}) \tag{59}$$

Where N denotes the total number of atoms in the crystal structure, $E_{\alpha}^{emb}(\rho)$ is the embedding energy function, $\phi_{\alpha_i,\alpha_j}(r_{ij})$ is the pair potential between atoms i and j with separation r_{ij}, and ρ_i is the background density at site i. The embedding energy function, pair potential and background density are described using:

$$E_{\alpha}^{emb}(\rho) = a_{\alpha}\rho^{\frac{1}{2}} + b_{\alpha}\rho^2 + c_{\alpha}\rho^3 \tag{60}$$

$$\rho_i = \frac{2\rho_i(0)}{1+e^{-\tau_i}} \tag{61}$$

$$\tau_i = \sum_{l=1}^{3} t_i^{(l)} \left(\frac{\rho_i^{(l)}}{\rho_i^{(0)}}\right)^2 \tag{62}$$

Here, a_{α}, b_{α} and c_{α} are parameters needed to be optimized. $\rho_i^{(l)}$ and $\rho_i^{(0)}$ are contributions to background density ρ_i with and without angular contributions. Setting $\rho_i^{(l)}$ to zero retains the standard EAM formalism. In addition, the background density without and with angular contributions are modeled using:

$$\rho_i^{(0)} = \sum_{j\neq i}^{N} f_{\alpha_j}^{(0)}(r_{ij}) \tag{63}$$

$$\left(\rho_i^{(l)}\right)^2 = \sum_{j,k(\neq i)}^{N} f_{\alpha_j}^{(l)}(r_{ij}) f_{\alpha_k}^{(l)}(r_{ik})\, P^{(l)}(\cos\theta_{\mathrm{jik}}) \tag{64}$$

Where, $f_{\alpha_i}^{(l>0)}$ are partial background density contributions and $P^{(l)}(x)$ $(l = 1,2,3,\ x = cos\theta_{jik})$ is the Legendre polynomial up to order 3, which introduces the effect of bond angle into the RF-

MEAM formalism. Similarly, the partial background density contributions and pair potential can be further expressed as a function of the fitting parameter a_α, b_α and c_α which is given by:

$$f_{\alpha_i}^{(l)}(r) = \textstyle\sum_{n=1}^{2} a_{\alpha_i}^{(n,l)} \left(r_{\alpha_i}^{(n,l)} - r\right)^3 \Theta(r_{\alpha_i}^{(n,l)} - r) \tag{65}$$

$$\phi_{\alpha_i,\alpha_j}^{(l)}(r) = \textstyle\sum_{n=1}^{2} b_{\alpha_i,\alpha_j}^{(n)} \left(s_{\alpha_i,\alpha_j}^{(n)} - r\right)^3 \Theta(s_{\alpha_i,\alpha_j}^{(n)} - r) \tag{66}$$

Where, n is the total number of terms to be included in the electron density and pair potential, $r_{\alpha_i}^{(n,l)}$ and $s_{\alpha_i,\alpha_j}^{(n)}$ are parameters needed to be optimized, and $\Theta(r_{\alpha_i}^{(n,l)} - r)$, $\Theta(s_{\alpha_i,\alpha_j}^{(n)} - r)$ are step functions in the form $\Theta(r' - r)$ with cutoff for $r' > r$.

Computational Tools for Interatomic Potential Development

To develop interatomic potential, one would require fitting parameters associated with embedding energy and pair potential in the energy formulation of embedded atom method (EAM) and reference free embedded atom method (RF-MEAM) potential. Now, these parameters are fitted from the experimental data for different properties of materials like bulk modulus, elastic constants, lattice constants, thermal expansion etc. or using abinitio molecular dynamics calculation.

There are many computational techniques on density functional theory (DFT) with a wide variety of DFT codes based on choice of system and type of simulation we want to perform. For instance, plane wave DFT is quite good for simulating small crystal structure since the calculation relies in reciprocal space (Fast Fourier Transform) by expanding Kohn-Sham orbitals in terms of plane waves with periodic boundary conditions[48]. In this type of technique, plane wave basis set depends on the value of kinetic energy cutoff for the given system and grid spacing. The computational cost for N number of atoms is typically in the order of $O(N^3)$ for this type of technique. Many DFT software's like Vienna Abinitio Simulation Package (VASP), Quantum Espresso, ABINIT, Cambridge Serial Total Energy Package (CASTEP) etc. are available that use plane wave DFT technique. Localized-orbital DFT or chemists DFT computational technique utilize more localized or fast decaying orbitals to perform calculations for the given system. This type of technique is not strict in terms of boundary condition as like plane wave DFT and periodicity can be switched off. The molecular dynamics calculation is rarely performed using this technique since basis function move with atoms, so it develop Pulay force on the system leading to inaccurate description of nucleus or electron. Further, for very small system this technique is usually faster than plane wave DFT because the computational cost is very low even using hybrid functional but, the cost increases quite rapidly if the accuracy is preferred. Some common examples of codes utilizing this technique include NWCHEM, ADF, TURBOMOLE etc.

Similarly, other technique like linear scaling DFT performs calculation on a linear scale $O(N)$ by adding additional approximation to that of density functional theory[48]. This type of technique is suitable for couple of thousands of atoms but, the accuracy may be greatly compromised. Some common software that uses this technique are ONETEP, SIESTA, BigDFT etc.

Vienna Abinitio Simulation Package (VASP) is most widely used DFT and abinitio molecular dynamics codes for computing quantum mechanical calculation from the first theory. It is a plane-wave DFT code that uses pseudopotential of type Local Density Approximation (LDA) and Generalized Gradient Approximation (GGA) for calculating exchange-correlation energies[49-51]. It uses various potentials such as norm-conserving, ultra-soft, or PAW potential to solve many-body Kohn-Sham equations self-consistently. The matrix diagonalization algorithms are very effective even with a limited plane-wave basis package. Symmetry analysis decreases the number of degrees of freedom, resulting in faster computation. Born-Oppenheimer molecular dynamics and structure relaxation are both possible with VASP. Many physical properties can be calculated directly by VASP without the need for external data. The VASP code can be used to simulate molecular dynamics for a few hundred atoms. These runs, however, necessitate extremely high memory requirements, which are difficult to meet on standard computers. This computation will take several weeks on a normal computer. A large device storage with more than hundreds of giga bytes is needed for medium cutoff energy and k-point spacing.

Several interatomic potential development codes exist based on types of potential. Rapid advancement and usage of machine learning and artificial intelligence divides the type of potential into two: functional or analytic interatomic potential and machine learning potential. Functional or analytic interatomic potential have certain analytic assumption on the potential energy surface and utilize the parameters in these analytic form in formulating interatomic potential to express the total energy of the crystal structure. While machine learning potential does not presume any analytic form of the potential energy surface but, rather tries to make correlation from the given large datasets between the crystal structure and potential energy surface and, once the correlation has been established then it is applicable for other test datasets and molecular dynamics simulation. There are wide range of interatomic potential development codes for functional form like POTFIT, MEAMfit, COMB, REBO etc., to develop potential for wide variety of materials. Recently, many machine learning interatomic potential codes based on neural network have been developed like aenet, Amp, ANI, DeepMD, PINN etc, are available for the purpose of describing many physical properties and chemical interactions. Many databases like Materials Cloud, Materials Project, NOMAD, AFLOW etc, are available for variety of materials from organic, inorganic, metallic and others that can be implemented to study wide range of properties based on machine learning.

MEAMfit is an interatomic potential development code that allows us to develop functional form of interatomic potential, specifically, embedded atom method (EAM) and reference free modified embedded atom method (RF-MEAM) potential[46]. MEAMfit code is very simple to use and has direct integration of VASP output that can be used as an input to generate EAM and RF-MEAM potential. In this code, the energy and force data from VASP output i.e., from vasprun.xml file is used as an input data to fit the parameters in the EAM and RF-MEAM potential. MEAMfit creates a fitdbse file that includes the trajectories when it runs for the first time. These files must be customized to meet the precise specifications. The optimization functions that MEAMfit use to find the best solution is shown below.

$$R^2 = \frac{\sum_n W_n\left(E_{pot}^{n} - E_{DFT}^{n}\right)^2}{\sum_n W_n\left(E_{DFT}^{n} - E_{DFT}^{avg}\right)^2} + \frac{\sum_n \sum_{i,\beta} W_n\left(E_{\beta,pot}^{n,i} - E_{\beta,DFT}^{n,i}\right)^2}{\sum_n \sum_{i,\beta} W_n\left(F_{\beta,pot}^{n,i} - F_{\beta,DFT}^{avg}\right)^2} \qquad (67)$$

Here n represents the number of trajectories in vasprun.xml files. E_{pot}^{n} and E_{DFT}^{n} are the total energy from the generated potential and from the DFT data for given n^{th} structure. $F_{\beta,pot}^{n,i}$ and $F_{\beta,DFT}^{avg}$ denote the force obtained from the potential and ab-initio data for the given structure. The cartesian components on atom i of n^{th} structure is represented by β. W_n is the measure of relative weight to which energy, force and stress data are given for parameter to fit. Typically, only considering energy data from the vasprun.xml file a fitted potential generate energy within 10% error of DFT data.

The conjugate gradient (CG) algorithm and the genetic algorithm (GA) are used in MEAMfit[46]. The optimization function (R) is minimized using the CG algorithm. The first potential is created by randomly initializing each potential parameter within the defined bounds. Parameters initialization for pairwise coefficients are randomly seeded from the range [-10, 10]. This range is the default value set by MEAMfit code. In the pairwise functions, random values are provided for cut-off radii. These random values are derived from the fitting database's smallest interatomic distance (0.9 Å) and the user-specified maximum cut-off radius. The randomly seeded potential will go for CG-optimization once minimization begins, and the value R falls below 10. Once ten potentials have been developed using this method, GA is used to combine pairs of potentials at random.

One can obtain the global minimum, which is difficult to obtain using only randomly seeded potentials using genetic algorithm. This optimization helps to benefit from previous ones. Although the first value of the potential parameter is provided at random, these starting values can be set using the existing potential. POTFILE=potparas in MEAMfit will get the starting values for the subsequent optimization from the setting file. MEAMfit generates EAM file compatible to that in LAMMPS and CAMELION formats once the optimization is complete.

COMPUTATIONAL DETAILS

Zirconium Diboride Crystal Structures for Ab-initio Simulation

To do computation for density functional theory and ab-initio calculation, the structure of zirconium diboride must be generated. Since it is essential to sample at different volume of the zirconium diboride crystal structure at different temperature to properly capture the phonon vibrations and explain thermal properties. I used 2x2x2 super cell (eight-unit cells) of zirconium diboride crystal structure for all my sample for VASP ab-initio molecular dynamics calculation using Materials Project with kinetic energy cutoff of 520 eV shown below in Figure 6[52].

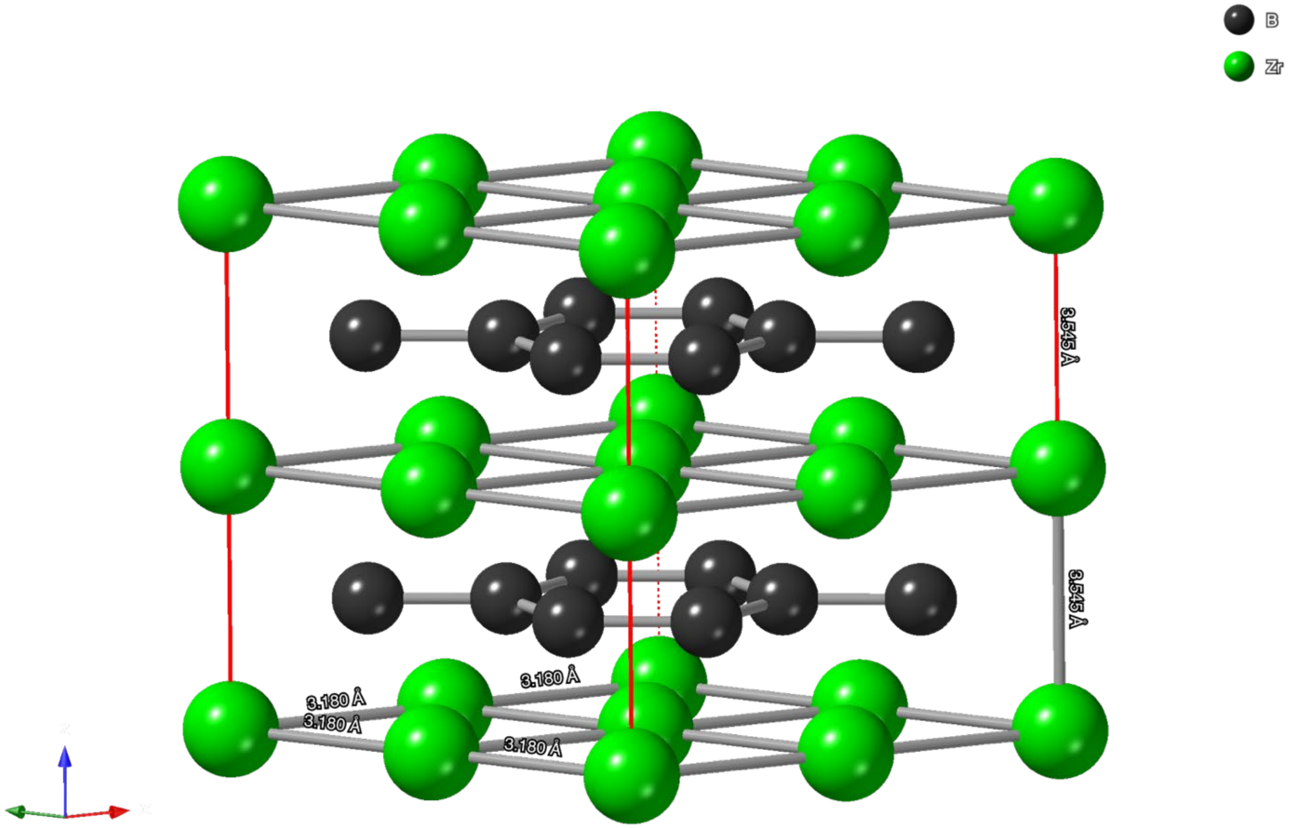

Figure 6: 2x2x2 (8-unit cells) super cell of zirconium diboride

I used Open Visualization Tool (OVITO) along with Visualization for Electronic and Structural Analysis (VESTA) for crystal structure manipulation to create crystal structure for different volumes. Different volumes were made either by scaling up or down by consecutive 2% increasing and decreasing the relaxed structure. Table 1 below shows the number of volume configurations made for the zirconium diboride crystal structure.

Table 1: Constant volume and temperature (NVT) VASP calculation of the sample structures for different volume scaling of relaxed crystal structure

Sample number	Volume change	Ensemble for VASP
1	±2%	NVT
2	±4%	NVT
3	±6%	NVT
5	±8%	NVT
6	±10%	NVT
7	±12%	NVT

Here, the changes in crystal structure made in this way are only the lattice parameters i.e., a and c of zirconium diboride crystal structure. However, I retained the angle of cell as that of relaxed structure for this sampling. Figure 7 below shows the lattice parameters of the zirconium diboride after scaling down volume by 2%.

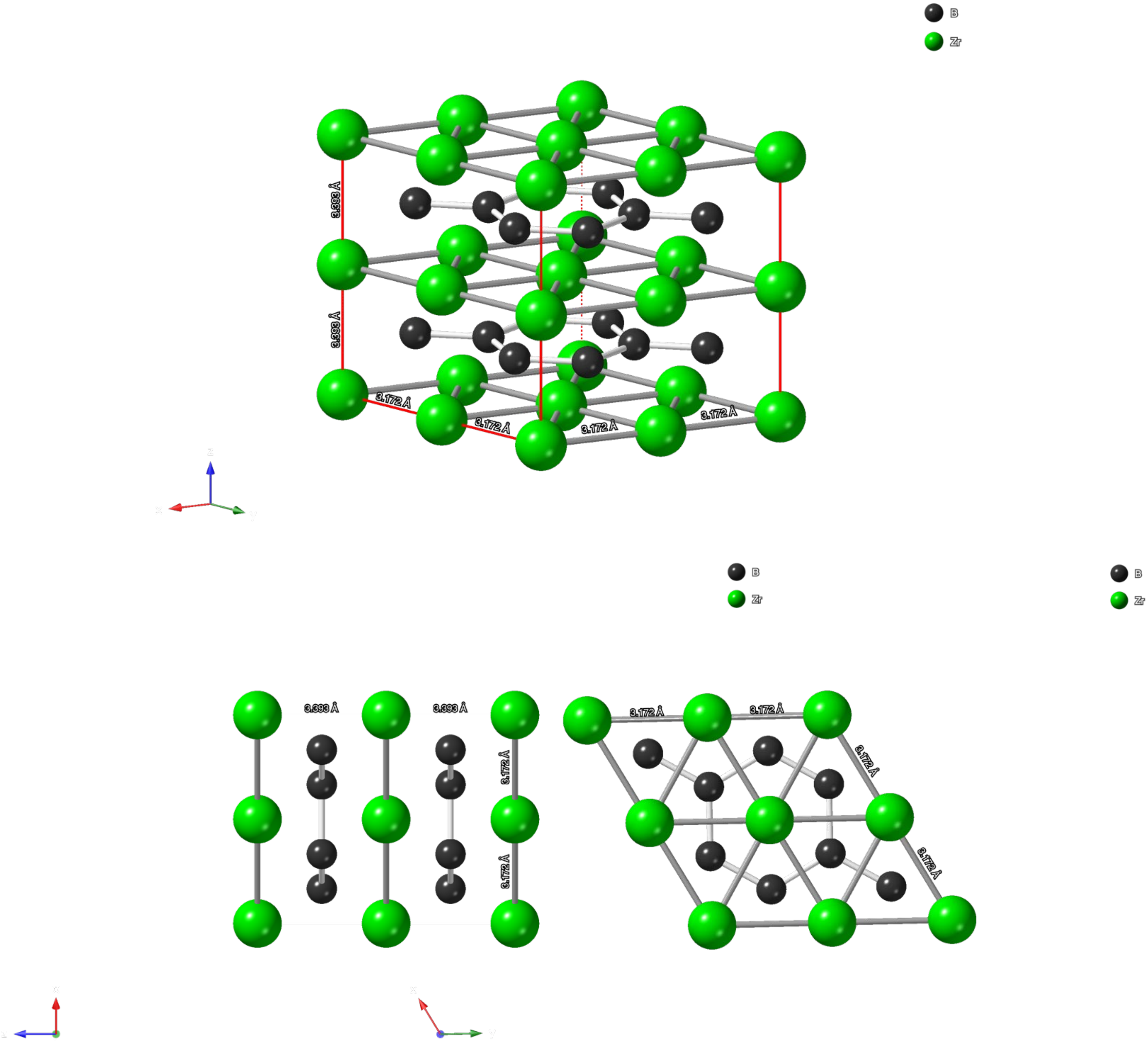

Figure 7: 2x2x2 super cell (a) top, (8-unit cells) of zirconium diboride with 2% volume reduced, resulting lattice parameter $a = 3.172$ Å and $c = 3.393$Å, (b) bottom left, front view of the 2% volume reduced (c) bottom right, top view of the 2% volume reduced zirconium diboride

Similarly, I also generated the crystal structure varying only one lattice parameters, either a or c. To vary the lattice parameter a, firstly, I fixed the lattice parameter c i.e., to 3.545Å and generated 100 structures by changing lattice parameter a by 0.1Å. Also, for generating structures with varying c, I fixed the lattice parameter a to 3.18Å and change lattice parameter c by 0.1Å. In addition, I also varied the cell angle of 2x2x2 super cell of zirconium diboride to better predict mechanical properties like elastic constants. This cell deformations are achieved by evaluating elastic constants of the relaxed structure of zirconium diboride using VASP. The relaxed 2x2x2 structure of zirconium diboride is given below in Figure 8. I used 2x2x2 super cell of zirconium diboride to calculate elastic constants using IBRION=6. The kinetic energy cutoff of 600 eV was used and Monkhorst-Pack scheme of 11x11x11 for this calculation. The calculation was performed based on the plane wave basis projector augmented wave method with Perdew-Burke-Ernzerhof (PBE) parametrization of generalized gradient approximation of exchange correlation functional as implemented in VASP[49, 51]. Thus, generated deformed cells were then used as a sample for AIMD calculation. There are 21 deformations of 2x2x2 super cells deformed along Zr or B plane and to the plane perpendicular to it.

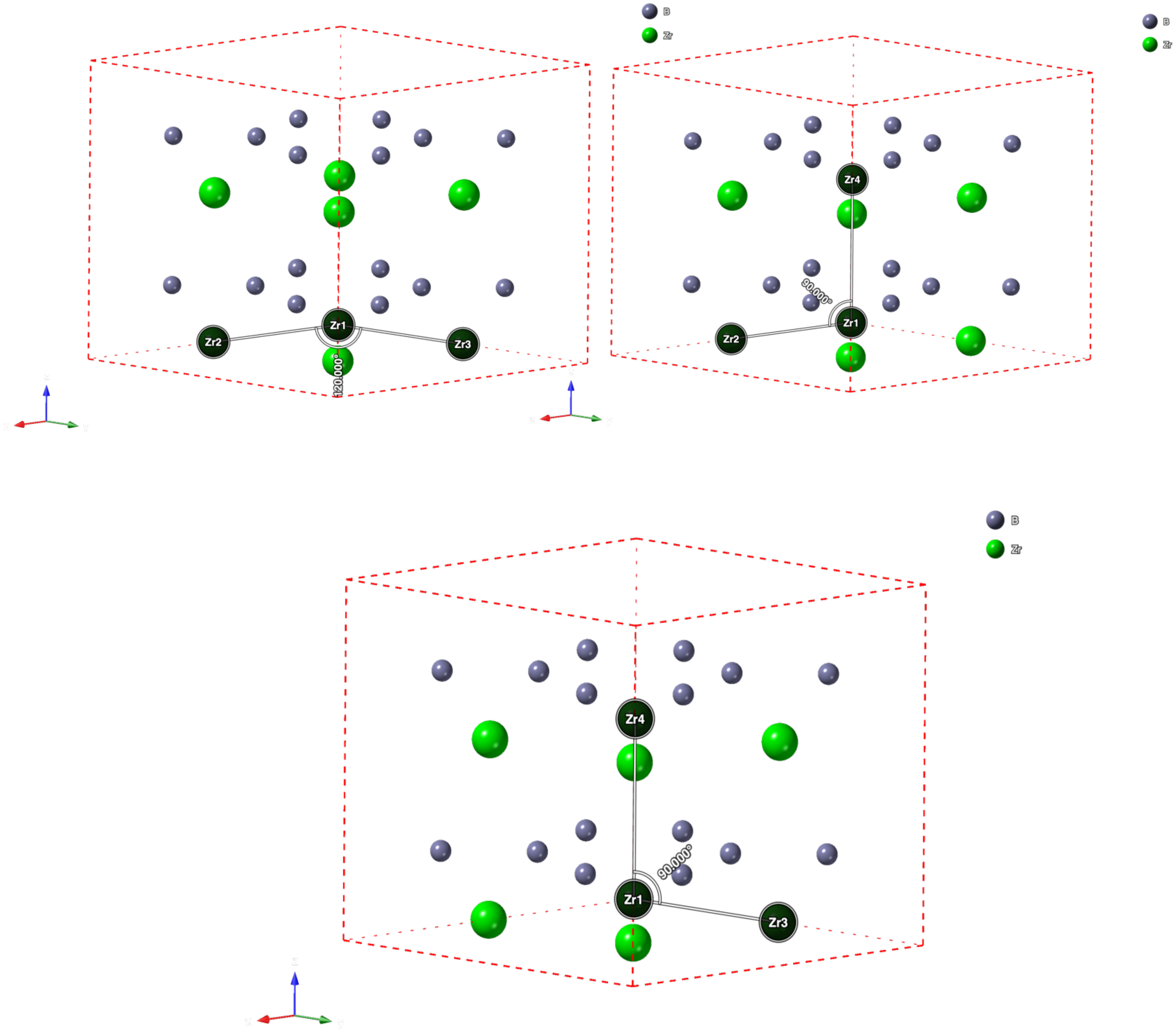

Figure 8: Undeformed 2x2x2 super cell of zirconium diboride (a) top left, with basal angle i.e., angle between α and β (b) top right, angle between Zr or B basal and perpendicular plane i.e., angle between α and γ (c) bottom, angle between Zr or B basal and perpendicular plane i.e., angle between β and γ. Here red arrow in the figure represents x-axis (lattice vector a1), green represents y-axis (lattice vector a2) and blue represents z-axis (lattice vector a3). α is angle between lattice vector a1 and a2, β angle between lattice vector a1 and a3 and γ the angle between lattice vector a2 and a3.

Here in the above undeformed 2x2x2 super cell of zirconium diboride in Figure 8, the cell angles are as it is in the hexagonal closed pack structure i.e., 120°, 90° and 90°. Figure 9 below shows the deformed super cell of size 2x2x2 with lattice parameter $a = 3.14044$ Å, $c = 3.54519$ Å and $a = 3.172168, c = 3.54519$ Å.

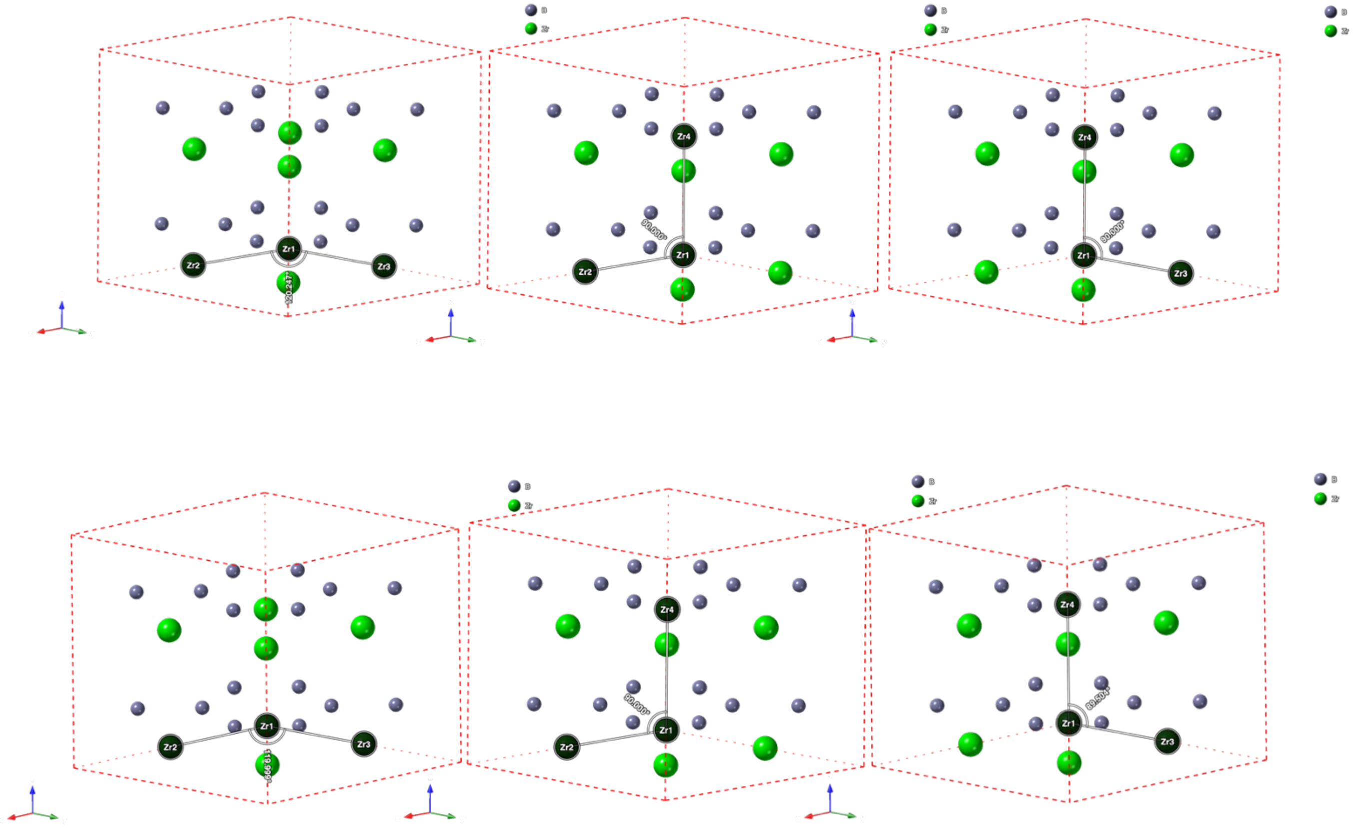

Figure 9: Deformed 2x2x2 super cell of zirconium diboride (a) top left, deformation along basal plane i.e., on angle α (b) top middle, no deformation on angle β (c) top right, no deformation on angle γ (d) bottom left, cell angle deformed by 0.01° on α (e) bottom middle, no change on angle β (f) angle γ changed to 89.504°

Ab-initio Simulation with VASP for Zirconium Diboride

After having sampled the structure of zirconium diboride for different volumes and deformations I discuss the procedure to obtain the behavior of these structures using ab-initio molecular dynamics with Vienna Abinitio Simulation Package (VASP). The objective of doing ab-initio molecular dynamics on the crystal structure is to acquire energy, force, and strain information at high temperature. At far from its melting temperature the atomic vibrations are mostly harmonic so firstly, I used constant volume and temperature (NVT) canonical ensemble to sample this information at relatively lower temperature of 1000K and 1500K from its melting point at 3500K. VASP allows different type of thermostat to achieve the NVT ensemble. Noose-Hover thermostat was used to get the temperature with ISIF=2 and MDALGO=2 settings in VASP. The kinetic energy cutoff was set to 520 eV which was 30% above the maximum energy cutoff for the recommended potential for Zr and B. This setting for energy was chosen throughout all abinitio molecular dynamics (AIMD) calculation of NVT ensemble. Similarly, the Monkhorst-Pack scheme of 4x4x4 was used in all the NVT ensemble including 1000K and 1500K sample. The precision was set to accurate and self-consistent field convergence of 1.0E-6 eV was used. Similarly, Gaussian smearing with smearing width of 0.03 eV was set for partial occupancies of set of orbitals. There are several ways of getting samples for different configurational space within the structure and canonical NVT ensemble temperature that would address the harmonic and anharmonic vibrations in the crystal structure. However, the general strategy here is to first match the thermal fluctuation due to harmonic vibration and consequently move to higher temperature for the given configurational space for sampling the anharmonic contribution[53]. I adopt this strategy and further simulate NVT ensemble at temperature 2000K, 2500K, 3000K, 3500K and 4000K for all given structures with volume scaling and deformations.

For the samples with varying lattice parameter, ground state calculation was performed with energy cutoff of 600 eV and Monkhorst-Pack scheme of 4x4x4. The precision set to Normal and self-consistent field convergence of 1.0E-4 eV was used. Gaussian smearing with width 0.03 eV was used. This type of sampling is like the volume scaling but also add to the variation of energy in changing only one lattice parameter a or c of the zirconium diboride crystal structure. Further, 50 sample structures of zirconium diboride with size 2x2x2 were taken by randomly displacing the atoms. The random displacement of atoms were performed using Phonopy and the magnitude of displacement of atoms was 0.1 Å[54]. Of these structures with randomly displaced atoms, ground state calculation was performed using ISIF=6. This setting allows us to fix position of the atoms and perform structure optimization on cell geometry. The kinetic energy cutoff of 600 eV was used along with gaussian smearing width of 0.03 eV and self-consistent field convergence of 1.0E-4 eV.

The effort to add possible sampling on deformations, NVT sampling by varying different lattice parameters (a or c only) and including cell geometry optimized structures by randomly displacing atomic positions in the volume scaling sample is to address for higher order force constants (third order and more) accounting anharmonicity and to better match the mechanical properties of the zirconium diboride including ground state and higher temperature bulk modulus and elastic constants.

MEAMfit for EAM and RF-MEAM Potential for Zirconium Diboride

The next step after ab-initio calculation of the zirconium diboride sample crystal structure is to fit the energy, force, and stress information. For each of the ab-initio VASP calculation, vasprun.xml file is generated that consists of energy, force and stress information of molecular dynamics run. 891 trajectories were generated for NVT ensemble with 1000K and 1500K and 4257 trajectories from 2000K, 2500K, 3000K, 3500K and 4000K sample. These trajectories were with volume scaling from vaprun.xml file. Each trajectory from the structures were generated from varying lattice parameters and randomly displacing the atoms. MEAMfit code allows us to fit the ab-initio VASP data to develop EAM and RF-MEAM potential[46]. The detailed working of the MEAMfit code is given in the introduction section. Fitdbse file was generated based on the given trajectories above. The fitdbse file contains the number of vasprun.xml files, number of trajectories in each of the vasprun.xml files and the weight to put on energy, force, and stress information for each of the vasprun.xml files. The weight is relative amount of energy, force, and stress data to put during fitting process. In fitting EAM and RF-MEAM potential, full weight is given to all the energy, force, and stress trajectories in the vasprun.xml files i.e., $w_n = 1$. Running MEAMfit again generates the separation histogram file and settings file. The separation histogram file contains the distribution of atoms/atomic pairs as a function of distance from the vasprun.xml files. The distribution of atomic pairs as a function of distance will be presented in the result. Similarly, in the settings, each EAM and RF-MEAM potential fit has the option to choose cutoff radius. This cutoff radius is the maximum distance up to which neighbor interaction is counted. MEAMfit has an option to consider the pair interaction using NTERMS tag. For each of the EAM and RF-MEAM potential, the cutoff radius was set to 4.4 Å and NTERMS to 3. This means that considering pair interaction, the interaction by third nearest neighbor term is counted within the interatomic distance of 4.4 Å. Similarly, another important parameter is NTERMS_EMB that accounts for contribution of nearest neighbor to construct electron density. The NTERMS_EMB was also set to 3 for each of the EAM and RF-MEAM potentials. Setting up these parameters MEAMfit runs the fitting but before running the fitting scheme another parameter OPTFUNCCG was set as the default value of 10. The OPTFUNCCG determines the threshold value for conjugate gradient minimization during the random sampling process.

RESULTS

EAM Potential for Zirconium Diboride

For both EAM and RF-MEAM potential, total number of 5348 trajectories obtained from ab-initio molecular dynamics via NVT ensemble and structural optimization/relaxation. From the AIMD runs with NVT ensemble at least 50 trajectories with 1 femto-second (fs) were obtained. The INCAR files for NVT sampling, structural optimization and deformations are given below in the APPENDIX. The statistical sampling for all the pairs is given below in Figure 10.

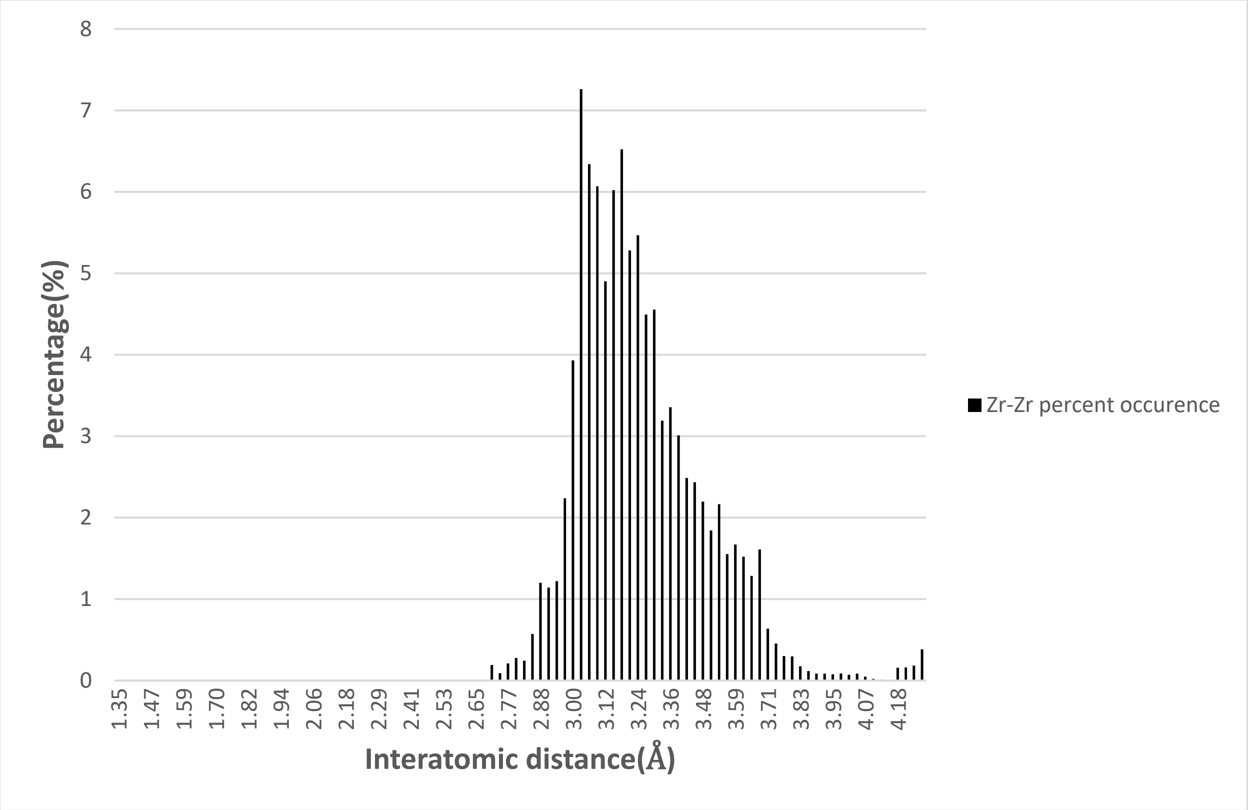

Figure 10: Percentage distribution of (zirconium-zirconium) Zr-Zr pair for all DFT samples

Mostly, the distribution peaks at 3.00261 Å. This suggests that the Zr-Zr pairs are available more around its equilibrium distance of 3.17 Å and less at smaller and larger interatomic separation. The variation of Zr-Zr pairs is directly correlated with the sampling of volume taken and since nearly 70% of samples are at high temperature and high volume or deformation, the distribution is skewed towards the right and has sampling more at larger distance than its equilibrium value of 3.17 Å[52]. Similarly, for the Zr-B pairs in Figure 11, at least second nearest neighbors are found in the sample as the percentage distribution of sample peaks at two values of 2.53 Å and 3.97 Å. As Zr-B interatomic separation is out of the Zr/B plane, the pair separation distance indicates that the Zr and B plane is quite intact even at the higher temperature since the equilibrium distance for Zr-B pair at ground state is 2.55234 Å and 4.078 Å (for first and second nearest neighbor).

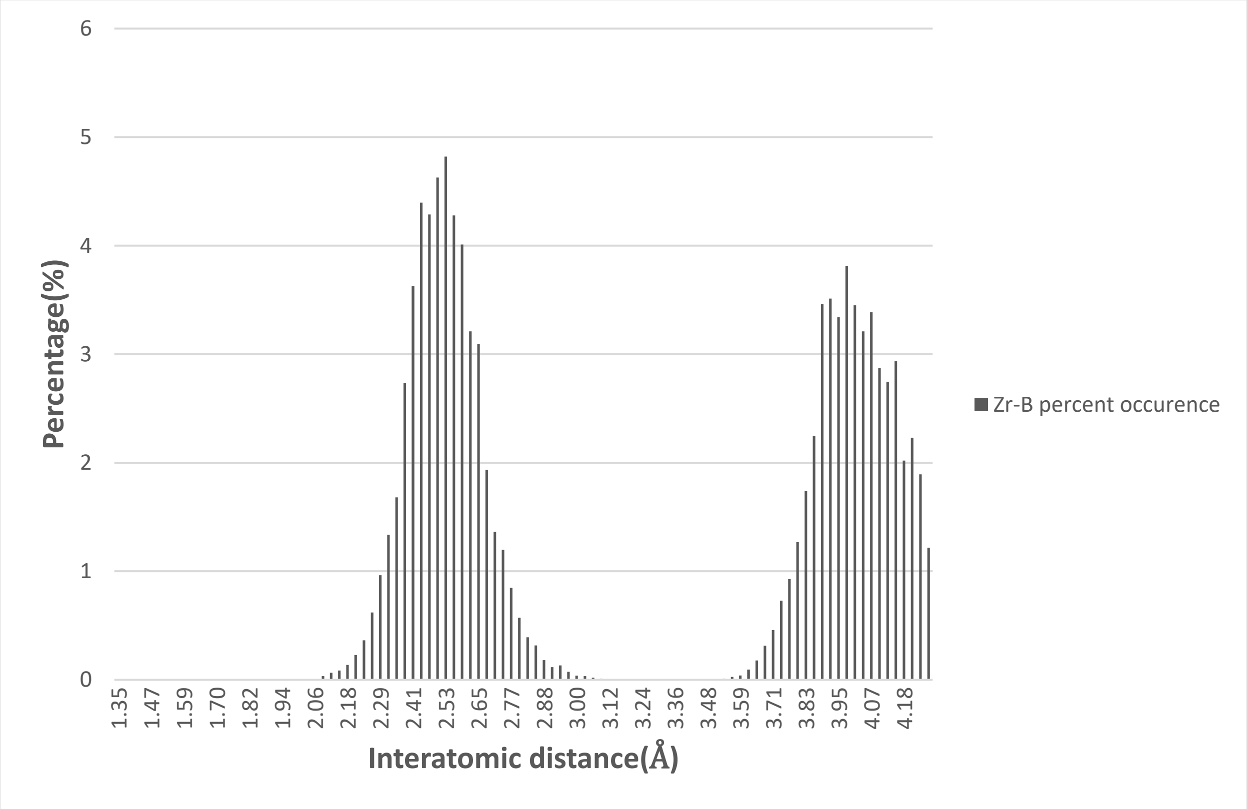

Figure 11: Percentage distribution of B-B pair for all DFT samples

Now, for the B-B pairs, the separation is sparser when it comes to second and third nearest neighbor in Figure 12. This is because the second neighbor and third nearest neighbor is relatively close at 3.18049 Å and 3.6725 Å of the boron ring at boron plane. The first nearest neighbor at 1.82 Å and the evenly distributed peak suggest that equal volume expansion and reduction of sampling present for the first nearest neighbor. The quality of the fit was determined by comparing

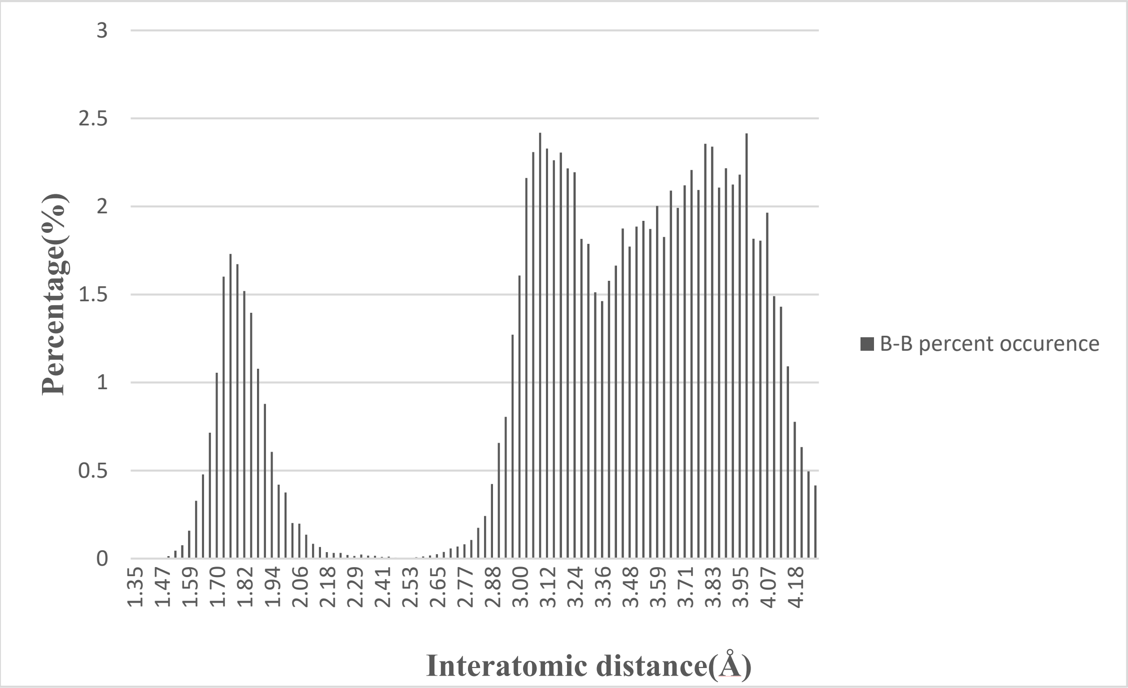

Figure 12: Percentage distribution of boron-boron (B-B) pairs for all DFT samples

the energy and force from the ab-initio simulation to the energy and force from the MD simulation of the developed EAM potentials each time a potential was formed. The true data is the data obtained from ab initio force and energy, while the fit data is obtained from EAM potentials. The first approach towards the validity of potential development is to match these energy and force data.

Figure 13(a) represent the energy fit obtained from the EAM potential and DFT calculation with a slope of 0.9884. This indicates that the energy values obtained from the EAM potential follows well to the DFT datasets. Linear regression analysis with regression coefficient of $R^2 = 0.991$ also suggest that the energy data from the EAM potential and DFT calculation matches well.

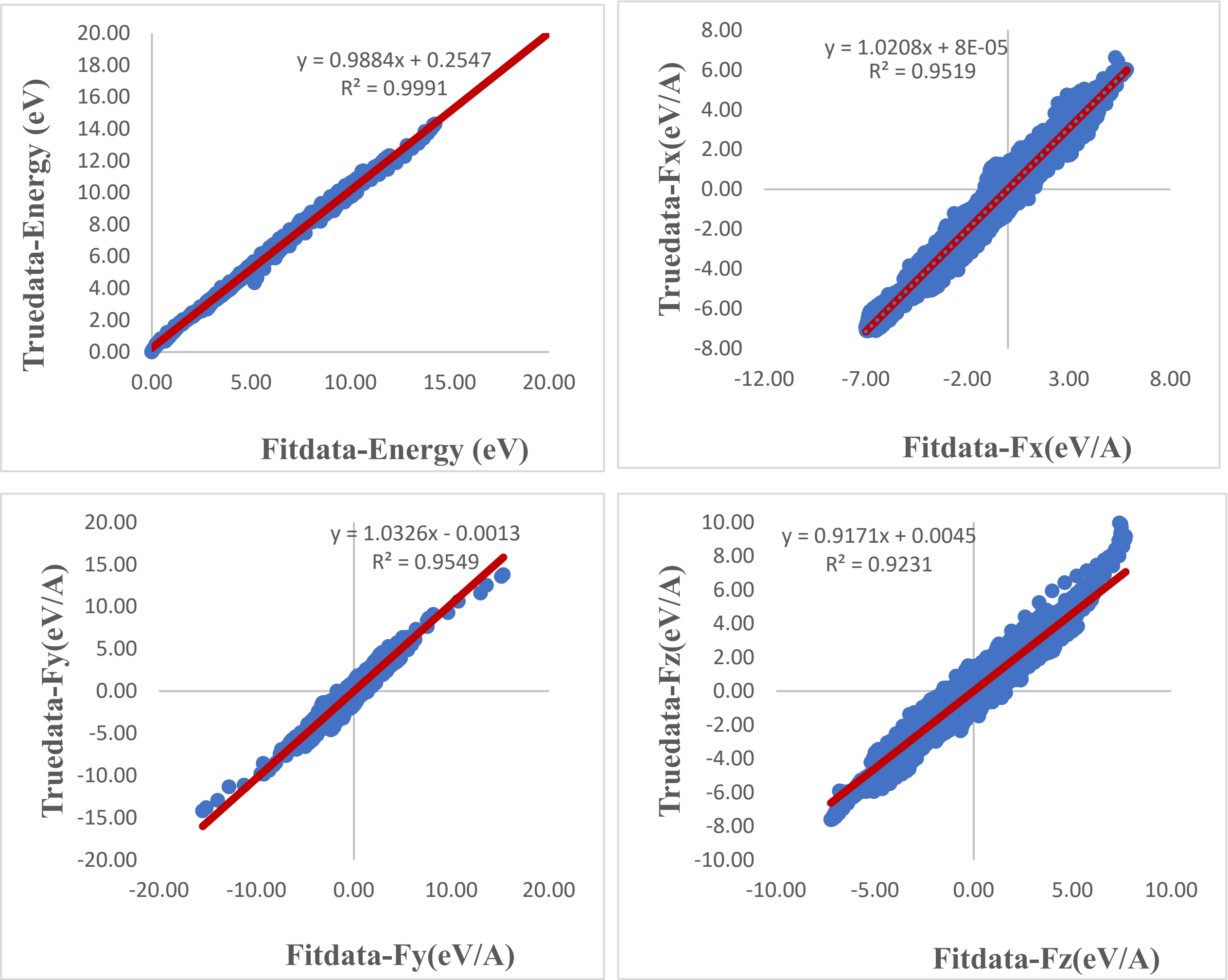

Figure 13 (a): Energy fit obtained from EAM potential to that of DFT (b) force fit data along x component (a-axis) (c) force fit data along y-component (b-axis) (d) force fit data along z component (c-axis)

In what follows, similar analysis on each of the forces along x, y and z direction with regression coefficients 0.9519 (slope 1.0208), 0.9549 (slope 1.0326) and 0.9231 (slope 0.9171) in Figure 13(b), Figure 13(c) and Figure 13(d) indicates that the EAM potential is able to correctly reproduce the force values of the DFT datasets with a reasonable quantification of its parameters. Similarly, the value of the optimization function obtained from MEAMfit code was 0.25, which is in agreement with the fit obtained from regression. Divergence was observed for higher force values along y-axis and z-axis near 10 eV/A. This may be possibly due to the limited number of points that were used for the larger force ranges. These data with higher positive force values are due to data with higher temperature sampling at 4000K. The vibration of atom at this temperature is comparatively higher causing high pressure of 75.8577 kbar and therefore higher force. I used more of the trajectories at 4000K into the sample to further fit higher force value and look up into the atomic vibration using phonon dispersion. For the fits with a larger sampling population (smaller force level), much better cartesian force fitting was obtained as shown in Figure 13. The parameters of the EAM potential for ZrB2 are given below in Table 2 (a) and Table 2 (b).

Table 2 (a): Parametrization of the ZrB_2 EAM potential for embedding functions

	$\boldsymbol{a}(\boldsymbol{eV})$	$\boldsymbol{b}(\boldsymbol{eV})$	$\boldsymbol{c}(\boldsymbol{eV})$
E_{Zr}^{emb}	10.064496271	2.572625271E-2	-2.000342775E-4
E_{B}^{emb}	6.345006591E-4	1.621390756E-3	-1.160965790E-5

Table 2 (b): Parametrization of ZrB_2 EAM potential for pairwise functions

	$\boldsymbol{a^{(1)}}$	$\boldsymbol{b^{(1)}}$Å	$\boldsymbol{a^{(2)}}$	$\boldsymbol{b^{(2)}}$Å
$f_{Zr}^{(l=0)}$	-0.970695245	1.678835710	-8.215461786	1.897361031
$f_{B}^{(l=0)}$	-4.795525007	3.155530117	1.025042683	4.302700579
$\phi_{Zr,Zr}$	70.353791434	4.133650447	4.320597369	2.961195564
$\phi_{Zr,B}$	562.65657584	3.342879995	-0.95492960	1.613735876
$\phi_{B,B}$	-186.083135395	2.624860851	5.945053708	1.903614237

The pairwise components of the EAM potential are shown in Figure 14 below. The relaxed DFT calculation for $B - B$ equilibrium positions, for example, is located at 1.83221 Å whereas the minimum is at 1.82 Å. Similar outcomes are also shown for Zr-B and Zr-Zr interatomic distances. The use of varied c/a ratio samples allows sampling of variations in Zr-B interatomic distance without necessarily altering the Zr-Zr or B-B interatomic planar distance

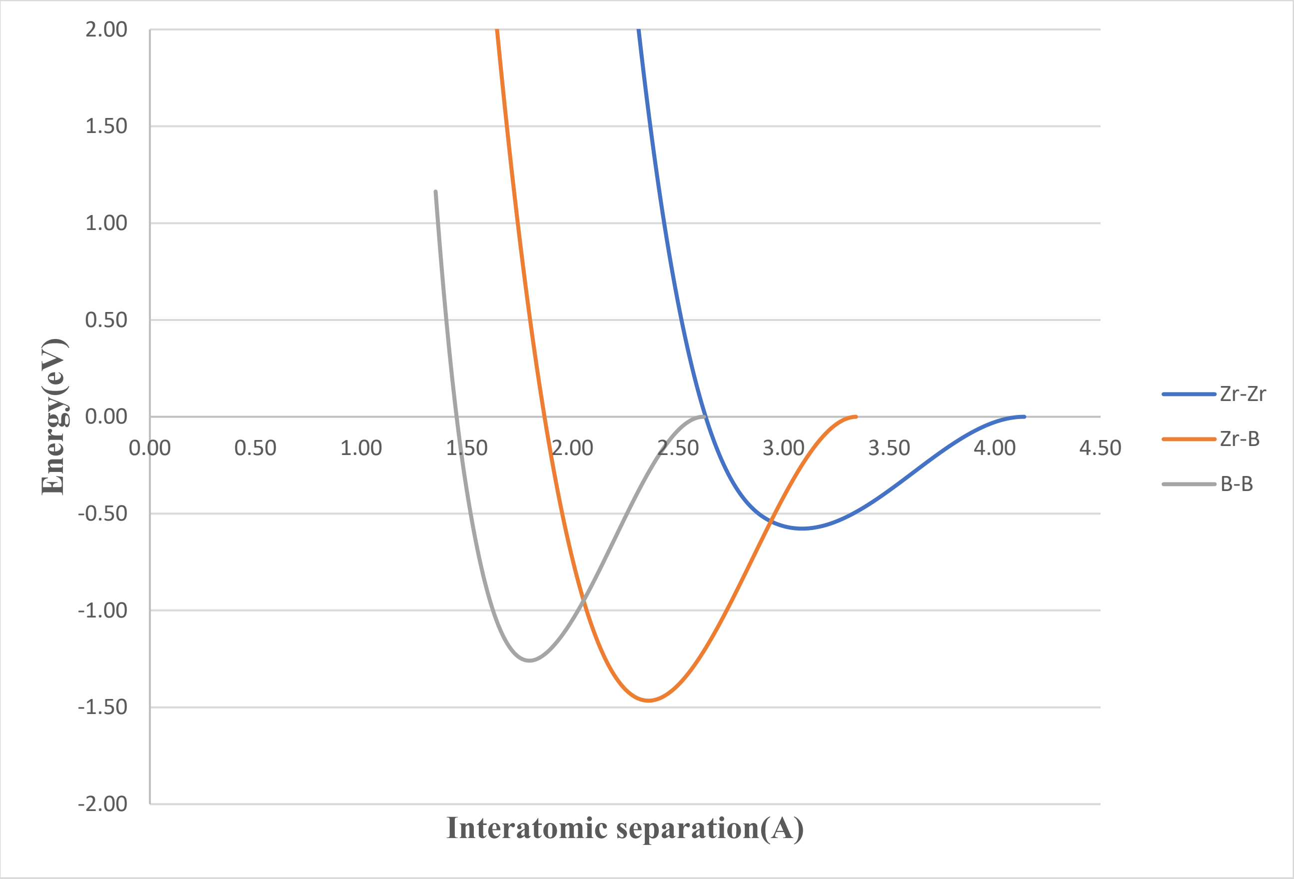

Figure 14: Pair potential for different atomic pairs in zirconium diboride using EAM potential

within the crystal structure. This also highlights the importance of utilizing larger sampling data and a wider range of pair interactions. For all of the atomic pairs i.e., Zr-Zr, Zr-B and B-B the shape of potential around minimum is harmonic and quadratic in nature so the potential is able to capture the harmonic vibration of the atom pairs. The harmonic motion is predominant below the midway of melting point in zirconium diboride. As we can see that the interatomic potential energy minimum for Zr-B pair is -1.463 eV which is greater than Zr-Zr pair and B-B pair. The Zr-B pair interaction strongly contributes to the melting temperature[2]. However, only the Zr-Zr pair interaction is weak compared to Zr-B and B-B pair and this degrades the strength and stiffness of zirconium diboride. Further insight into the electron density in Figure 15 presents the fact that density for boron is compromised below the interatomic separation of 1.6 Å. The electron density below interatomic separation of 1.6 Å for boron is mainly at the repulsive side of B-B interaction since the equilibrium distance for

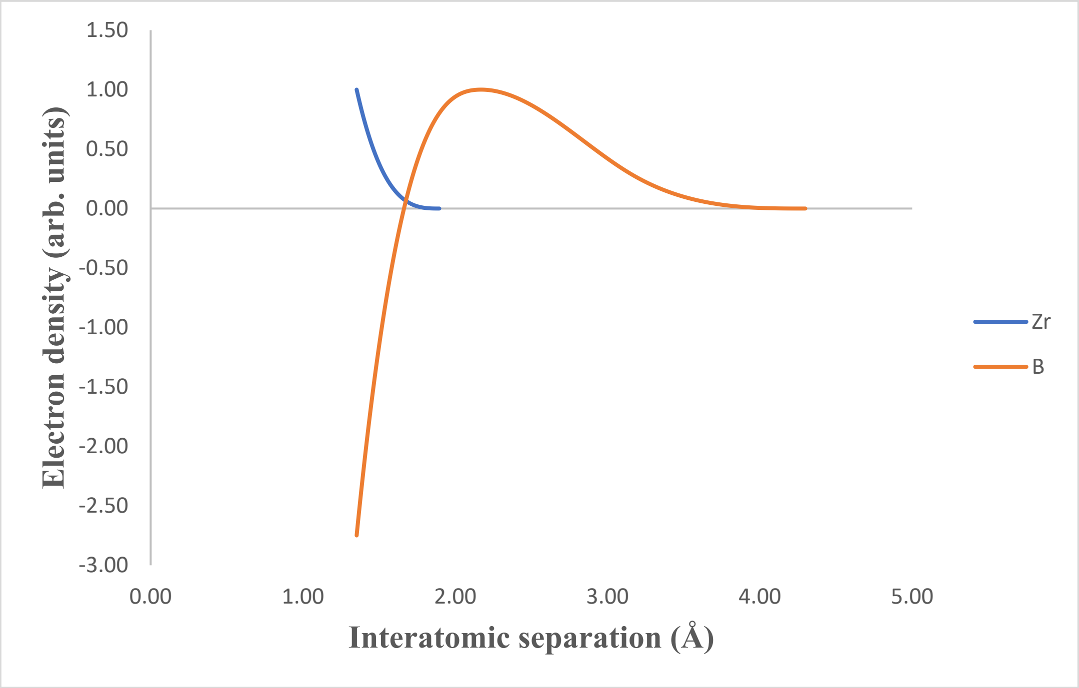

Figure 15: Normalized electron density as a function of interatomic separation

B-B pair is at 1.82 Å. The repulsive forces are predominant either in high pressure sample or reduced volume sample at high temperature i.e., the sample at 4000K. The effect of this ill-behaved density is that it is not able to capture the vibration of atom, especially, the boron atom at higher temperature where the anharmonic vibration exceeds the harmonic vibration. However, for larger interatomic separation the electron density for boron is well behaved and capture the decay of electron density as a function of interatomic separation. The shape of embedding function for zirconium in Figure 16 resembles that of electron density.

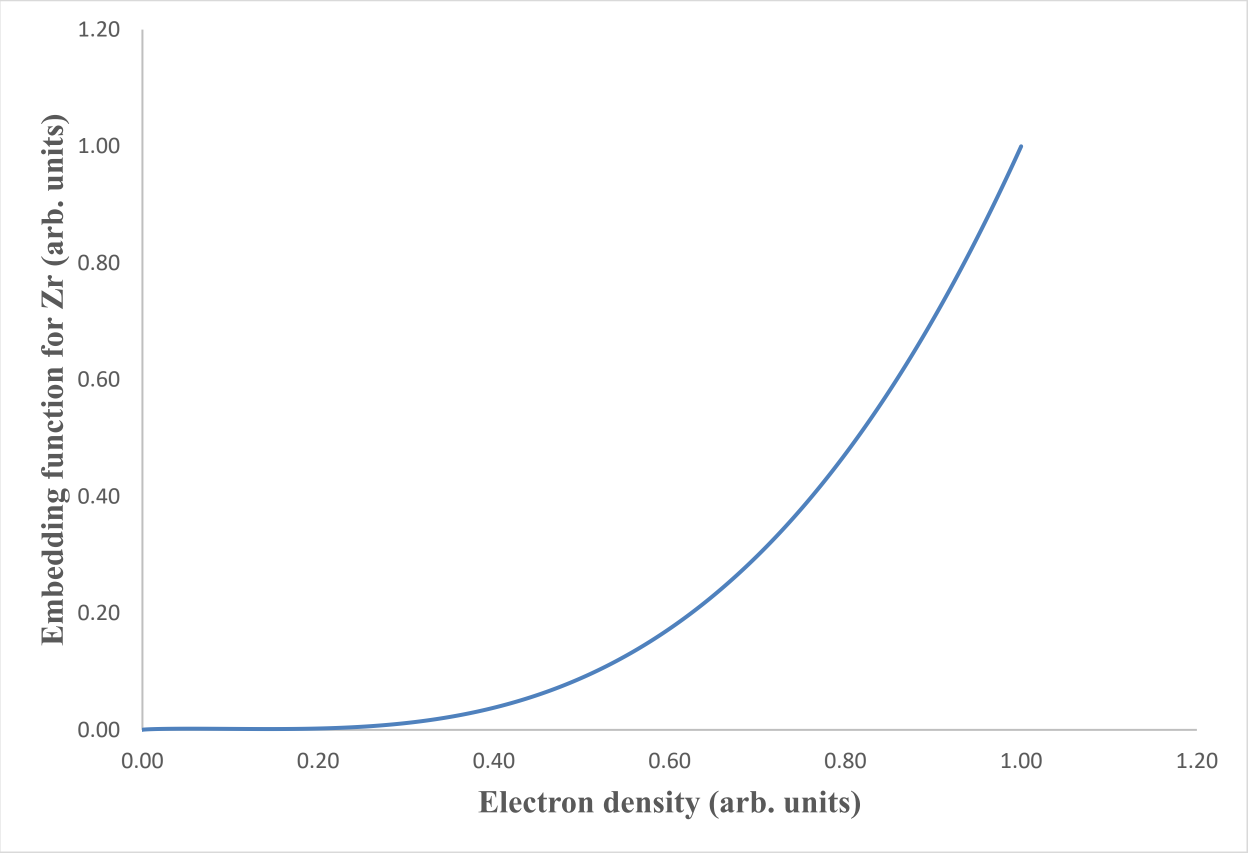

Figure 16: Normalized Embedding function for zirconium as a function of electron density

The normalized embedding function for both zirconium and boron are plotted against the normalized electron density in Figure 16 and Figure 17 respectively. As the electron density is just the linear combination of the electron density of neighboring atoms, the embedding function follows the shape of electron density given by Daw and Baskes for zirconium in EAM potential[43]. As the shape of density by Daw and Baskes is just the exponential decay coupled with quantity for number of valence electrons and some adjustable parameters, the functional too has similar nature given below in Figure 17.

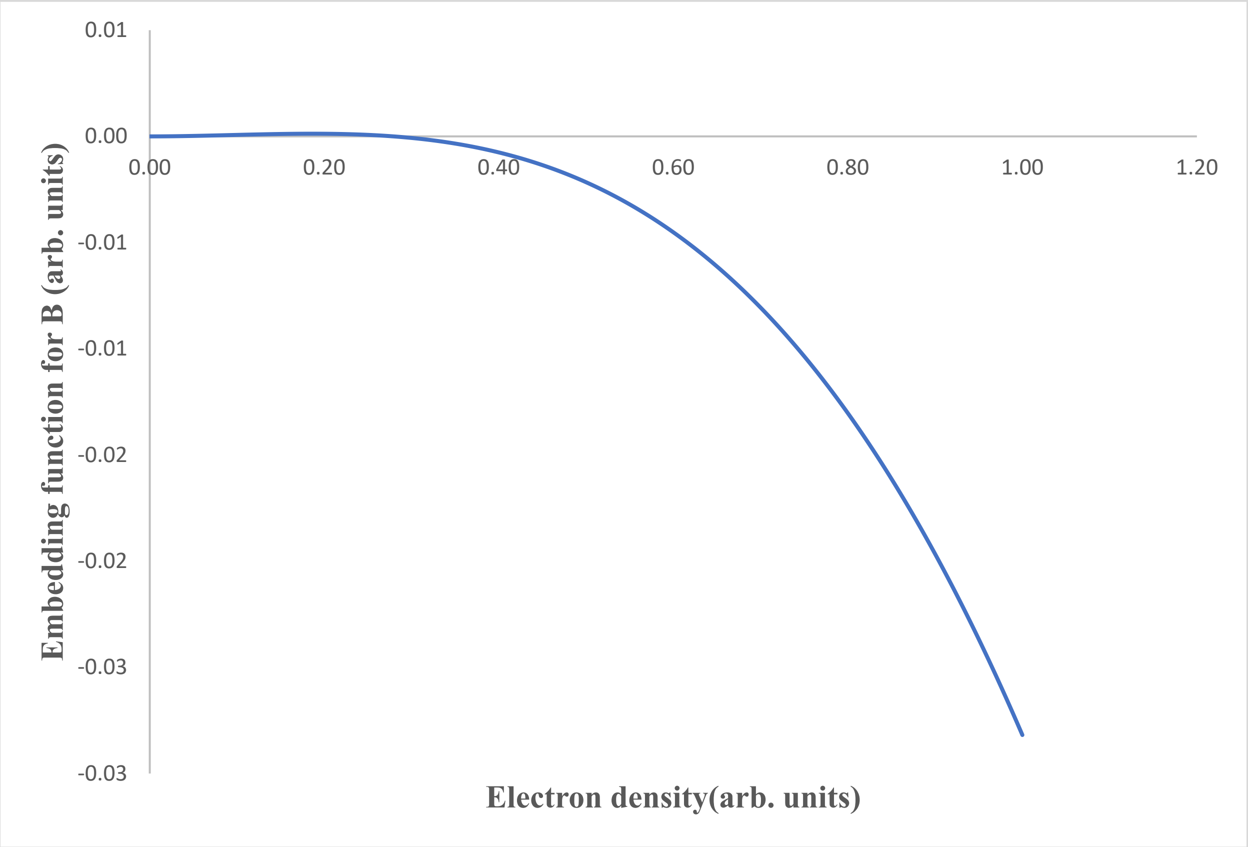

Figure 17: Normalized embedding function for boron as a function of electron density

RF-MEAM Potential for Zirconium Diboride

Similar to the energy fitting in EAM, the regression coefficients were 0.9991 (slope 1.0002), 0.9702 (slope 0.9982), 0.979 (slope 1.0119), 0.96 (0.991) for energy, force along x-axis, y-axis and z-axis, respectively in Figure 18(a), Figure 18(b), Figure 18(c) and Figure 18(d). The results show that the RF-MEAM potentials fit better than EAM potential when compared to DFT energy and force datasets. Here, for the energy fit to the DFT data, similar regression value is obtained as that for EAM potential. However, the distinction can be made to the force fitting. Because the EAM was not able to capture higher force values along y and z-axis, the regression value of force component along x, y, and z-axis with regression coefficient 0.9702, 0.979 and 0.96 is greater than that for EAM potential. This shows that RF-MEAM is able to better capture the higher forces value of high temperature sample at 4000K. Also, an optimization value of 0.23 was obtained from MEAMfit, which is consistent with regression analysis since this is the square average of the energy and force fits. Figure 18 compares the energy and cartesian force fitting between RF-MEAM and DFT calculations. The RF-MEAM values fit better than the EAM data, especially at higher force values. While low statistical samplings remain because the same data were used, the additional parameters employed in RF-MEAM help delineate the force contributions that result from the angular dependency. Table 3 (a), Table 3 (b) and Table 3 (c) below shows the parametrization of zirconium diboride for RF-MEAM potential. The addition of extra angular term in the parametrization with angular dependence contribution for $l = 1, l = 2$ and $l = 3$ fine tune the electron density for zirconium and boron that was absent in EAM potential. This also introduces the effect of bond angle in pairwise function and additional background density prefactors model the electron density at high temperature regime which I will be discussing below.

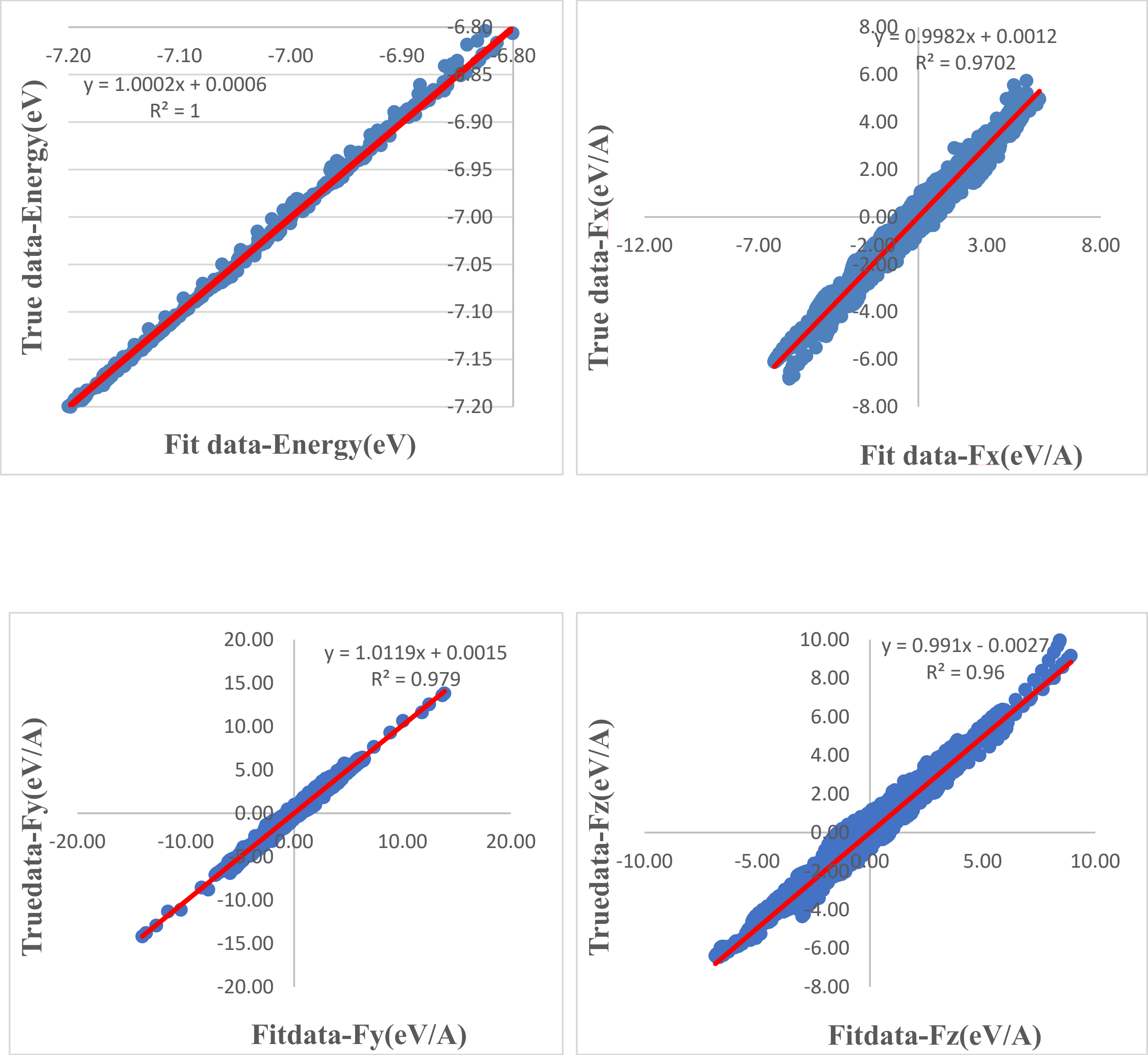

Figure 18: (a): Energy fit obtained from RF-MEAM potential to that of DFT (b) force fit data along x component (a-axis) (c) force fit data along y-component (b-axis) (d) force fit data along z component (c-axis)

Table 3 (a): Parametrization of ZrB_2 RF-MEAM potential for embedding functions

	$\boldsymbol{a}(\boldsymbol{eV})$	$\boldsymbol{b}(\boldsymbol{eV})$	$\boldsymbol{c}(\boldsymbol{eV})$
E_{Zr}^{emb}	0.468879747	-1.080724965E-3	1.075181169E-8
E_{B}^{emb}	1.999724253	1.061089499E-3	-5.946560991E-8

Table 3 (b): Parametrization of ZrB_2 RF-MEAM potential for pairwise functions

	$\boldsymbol{a}^{(\mathbf{1})}$	$\boldsymbol{b}^{(\mathbf{1})}$Å	$\boldsymbol{a}^{(\mathbf{2})}$	$\boldsymbol{b}^{(\mathbf{2})}$Å
$f_{Zr}^{(l=0)}$	2.379212158	2.002392789	6.975737719	2.179132926
$f_{Zr}^{(l=1)}$	-20.844456639	2.675448658	9.484100315	3.274452548
$f_{Zr}^{(l=2)}$	1.861463237	2.001695505	0.170608968	4.300691942
$f_{Zr}^{(l=3)}$	-5.838191610	3.185531811	6.271272076	3.529929373
$f_{B}^{(l=0)}$	2.065914315	2.002840591	1.464261431	3.701294261
$f_{B}^{(l=1)}$	7.391006372	3.030072001	-0.800069262	4.300925564
$f_{B}^{(l=2)}$	15.476480540	3.639311263	-15.892792579	3.602294698
$f_{B}^{(l=3)}$	15.113564318	3.662862215	-33.742956749	3.120952802
$\phi_{Zr,Zr}$	1.070660743	3.612628484	1.457329486	1.775642616
$\phi_{Zr,B}$	3.543207871	2.789923749	-1.736467135	2.159654436
$\phi_{B,B}$	11.209743335	1.981329643	-0.459566690	2.757900033

Table 3 (c): Parametrization of ZrB_2 RF-MEAM potential for density prefactors

	Zr	**B**
$t_{\alpha}^{(1)}$	-5.94322349	17.692141145
$t_{\alpha}^{(2)}$	2.119537031	-0.334007432
$t_{\alpha}^{(3)}$	-40.455207045	0.831323720

The pairwise components of the RF-MEAM potential are shown in Figure 19 below. The relaxed DFT calculation for $B - B$ equilibrium positions, for example, is located at 1.82 Å whereas the minimum is at 1.7823 Å for RF-MEAM potential. This might seem erroneous for the reason that minimum for EAM is quite accurate at 1.83221 Å to that of DFT calculation rather than RF-MEAM potential. However, the shape of pair potential weigh even more. Since the equilibrium distance is with respect to ground state calculation. The shape of interatomic potential dictates forces at higher temperature. In the EAM potential, the shape is largely harmonic at higher value of interatomic separation, even up to 2.3 Å. But, for the RF-MEAM potential, it introduces fair amount of anharmonicity from 1.9 Å. Now, for the Zr-Zr and Zr-B pair potential, even though the minimum has not been achieved, the components for this part have largely been suppressed and provide more emphasis on the electron density.

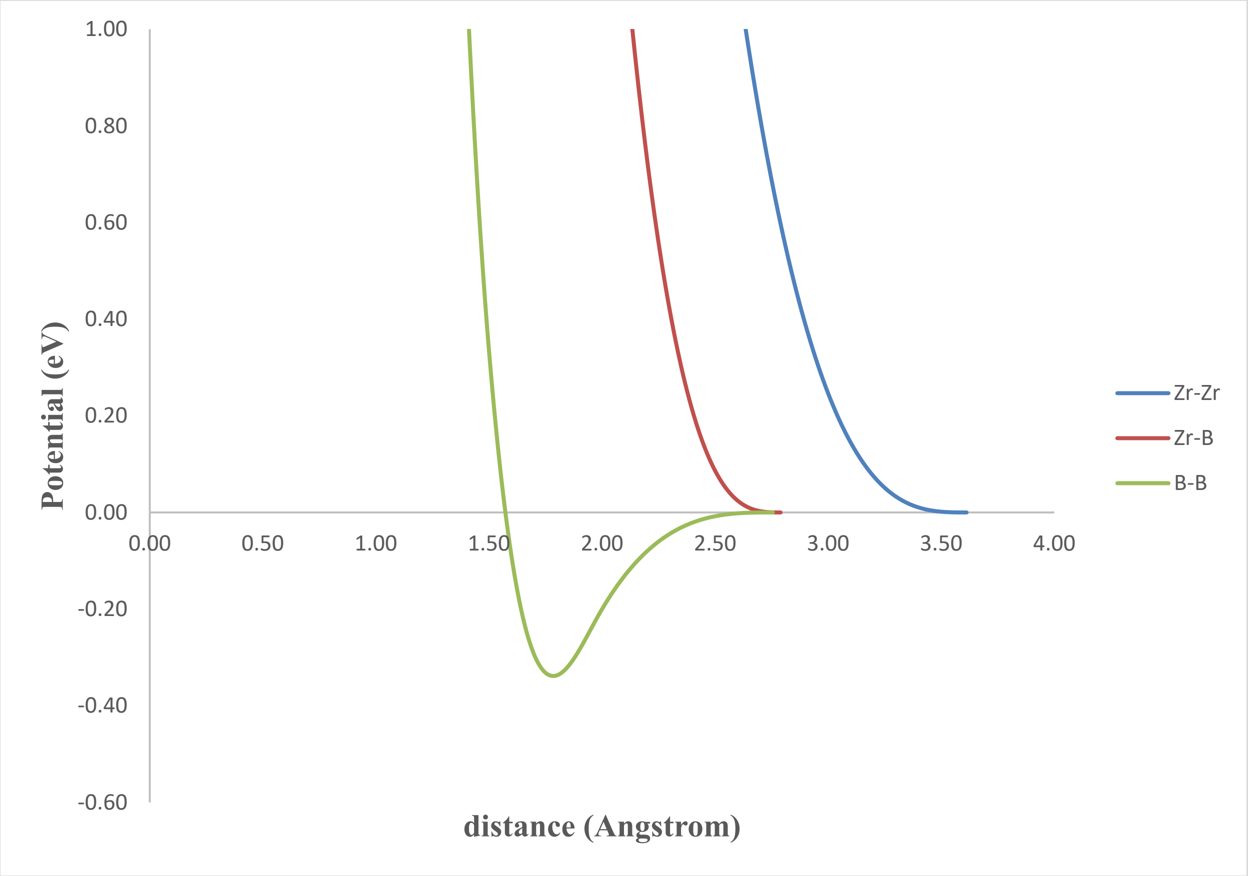

Figure 19: Pair potential for different atomic pairs in zirconium diboride using RF-EAM potential

Here, the electron density formalism is described by Daw and Baskes for the RF-MEAM potential[45]. Figure 20 below gives the variation of electron density for RF-MEAM potential as a function of interatomic separation. Unlike the electron density of boron in EAM potential, the electron density in RF-MEAM potential below 1.6 Å is well behaved. This electron density for B is decreasing as a function of interatomic separation and is a moderate fall as we would expect. Since, B-B bonding in zirconium diboride is covalent and symmetric in a plane with hexagonal structure and this would mean the distribution of electron is not abrupt and decrease smoothly as distance increases. The electron density for RF-MEAM potential alleviates the unconventional electron density for boron in EAM potential. To the other side, there is no significant improvement of electron density for zirconium over EAM potential. The EAM potential was able to only capture the electron density up to 1.895 Å but here, the RF-MEAM potential is able to capture density up to 2.1784 Å. In both the potential, there is a steepest decline in electron density for zirconium.

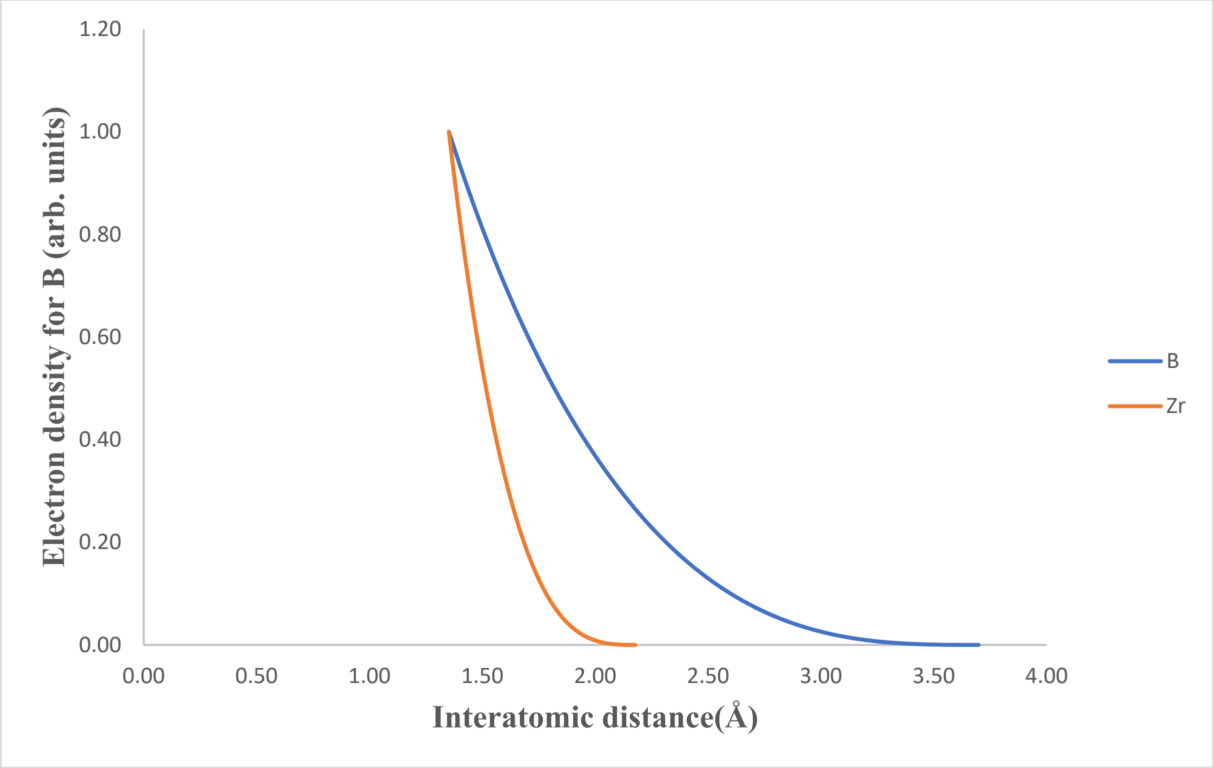

Figure 20: Normalized electron density as a function of interatomic separation for RF-MEAM

The embedding function for zirconium and boron is given below in Figure 21 and is quite opposite to that of EAM potential. The parameters a, b and c that determines the embedding function are different and especially the value of b is negative for RF-MEAM potential. This signifies that more of pair potential part is embedded into the embedding function.

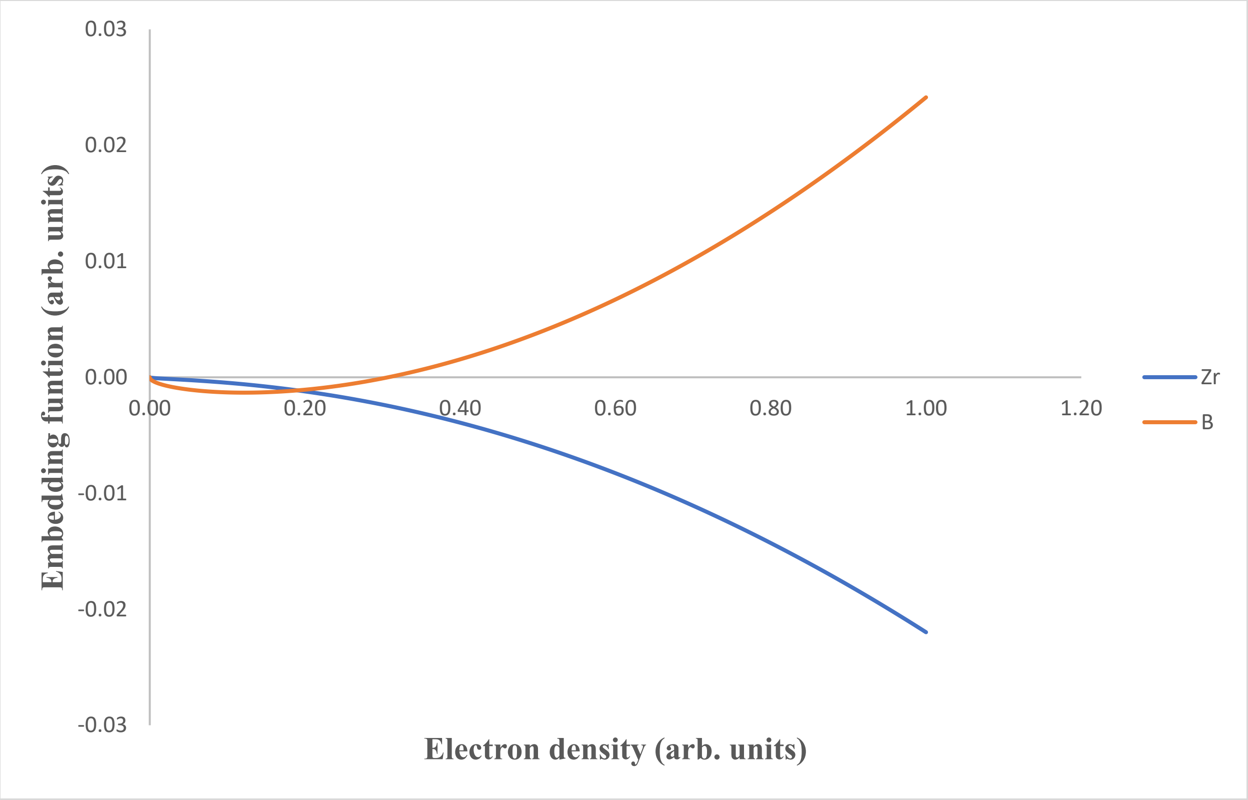

Figure 21: Normalized Embedding function for zirconium and boron as a function of electron density for RF-MEAM potential

DISCUSSIONS

Following the fitting process, EAM and RF-MEAM potentials were evaluated using a variety of computational methods for thermal and high-temperature mechanical properties. MEAMfit converts EAM and RF-MEAM potential into a LAMMPS-readable format. To execute the simulations, multiple molecular dynamics codes other than LAMMPS were employed, including phonopy, phonolammps, AICON and alamode[55-61]. To test the effectiveness of the developed potential several thermal properties like phonon dispersion, phonon density of states, thermal expansion, specific heat capacity, phonon relaxation time and thermal conductivity of zirconium diboride were evaluated. Similarly, I also tested the mechanical properties of zirconium diboride, especially the bulk properties of zirconium diboride like elastic constants, bulk modulus and high temperature elastic properties. All the properties measured were either compared to DFT calculation or to the experimental values.

Thermal Properties of Zirconium Diboride

Phonon Dispersion and Density of States. The vibrational properties of zirconium diboride including phonon dispersion curve and density of states were calculated using phonolammps and phonopy. Phonon dispersion curve using DFT was computed using density functional perturbation theory as implemented in VASP and phonopy[49-51, 54]. IBRION=8 was used to determine hessian matrix to evaluate force constants based on 2x2x2 supercell for the relaxed unit cell. For phonon dispersion using EAM potential, firstly relaxed unit cell of zirconium diboride is used to calculate force constants using 2x2x2 supercell by phonolammps.

After phonolammps evaluates force constants, phonon dispersion was obtained using phonopy with tetrahedron method and Monkhorst-Pack scheme of 8x8x8.

Figure 22 compares the phonon dispersion curves for conventional symmetry points along the first Brillouin zone of hexagonal lattice given below. The phonon dispersion curve consists of 9 dispersion curve, 3 phonon dispersion curves for each atom in a unit cell of zirconium diboride. 3 phonon modes which are below 9 THz represents acoustic phonon modes and in fact one longitudinal acoustic and two optical acoustic. These phonon modes occurring below 9 THz frequency is given by the heavier element, because phonon frequency is inversely proportional to mass $\left(\omega \propto \frac{1}{m}\right)$. So, in zirconium diboride the low frequency modes are given by zirconium. Similarly, the higher frequency modes are given by boron in zirconium diboride. These non-zero high frequency modes are in fact optical phonon modes occurring above 9 THz and below 25 THz in Figure 22 below. In general, the zirconium diboride is vibrating below 25 THz frequency range as can be seen using both the DFT calculation (blue curve) and that using EAM potential (orange curve). The in-phase vibration of Zr atoms (acoustic phonon modes) for EAM potential are in good agreement with the DFT calculated values which are below 9 THz in Figure 22 of the phonon dispersion curve. This means that EAM potential is able to capture quite precisely the vibration of zirconium atom only along x-, y- and z-axis respectively. Likewise reasonable frequency range was observed for optical phonon modes by EAM potential. EAM potential slightly overestimates the higher frequency optical phonon modes greater than 20 THz. These two phonon modes are boron vibrating in xy plane and out of xy plane while zirconium atom being fixed. Similarly, EAM potential also has a reasonable representation of phonon bands below 15 THz and these phonon modes are zirconium dominated boron vibration. This boron vibration occurs in boron in the xy plane when zirconium vibrates in xy plane. The other phonon modes below 15 THz is boron vibration in xy plane while zirconium vibrates along z-axis.

Now remaining two optical phonon modes greater than 13 THz and less than 20 THz are highly angular dependent zirconium and boron vibration in which all the angles between B-Zr-B triplets are changing. One of the phonon modes at this frequency range is zirconium dominated boron vibration in which case zirconium and boron are both vibrating along z-axis but opposite in direction. Similarly, other phonon mode is the boron vibrating along yz plane, but two boron's in opposite direction and zirconium along z-axis. The EAM potential is clearly not able to capture these phonon modes. Since because EAM potential lacks angular dependence terms the

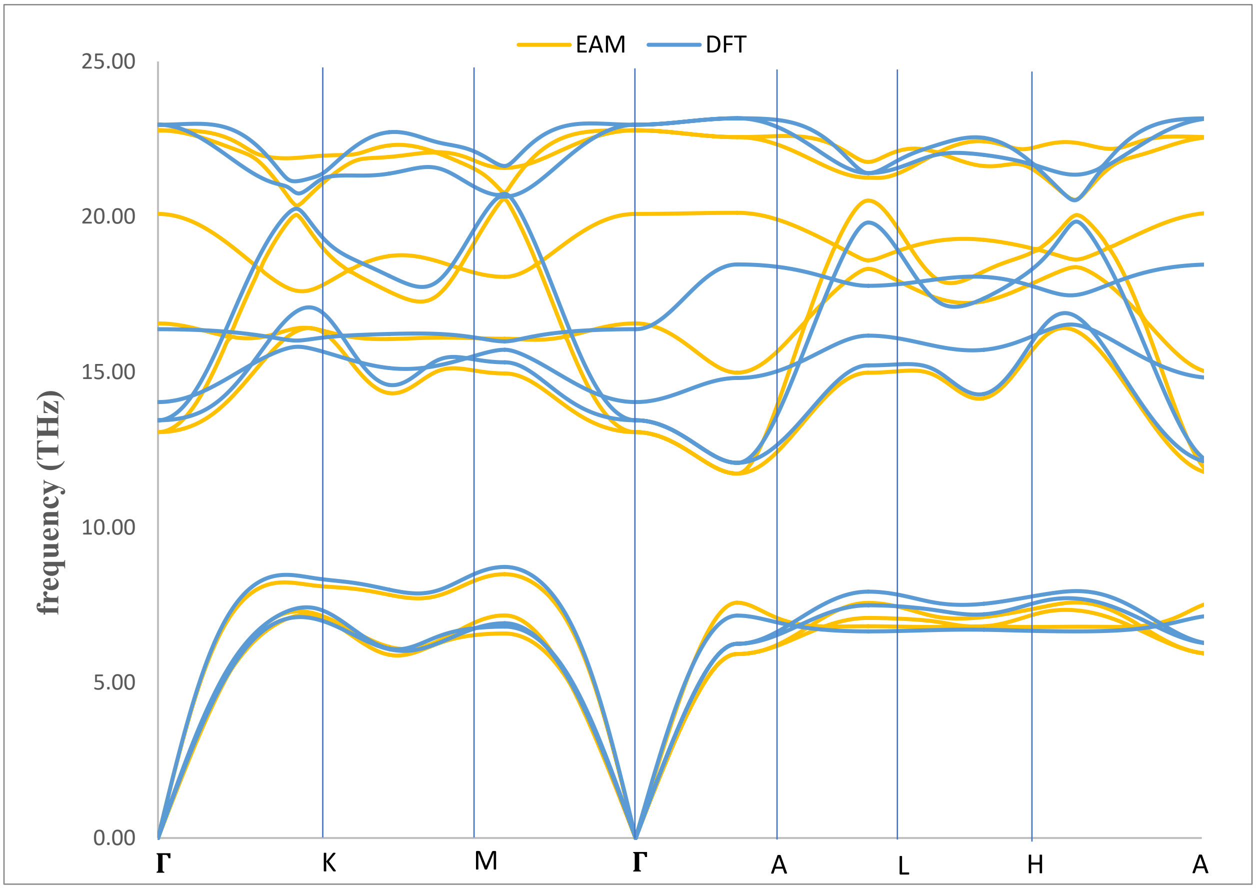

Figure 22: Phonon dispersion curve for EAM potentials compared with DFT calculation

frequencies are not correctly reproduced along the symmetry points in first Brillouin zone of hexagonal lattice. The EAM potential highly overestimates the vibrational frequencies for the phonon modes. Now, in contrast to EAM potential for the given same sample the RF-MEAM potential is able to follow the vibrational frequencies in the frequency range 15 THz to 20 THz but slightly overestimate it in Figure 23. The additional angular contribution and addition of background density prefactors in the parametrization of RF-MEAM potential sense the B-Zr-B triplet accurately by changing the electron density for boron and thereby the embedding function. The correction in phonon frequency in range 15 THz to 20 THz helps in better understanding of the thermal expansion and high temperature elastic constants.

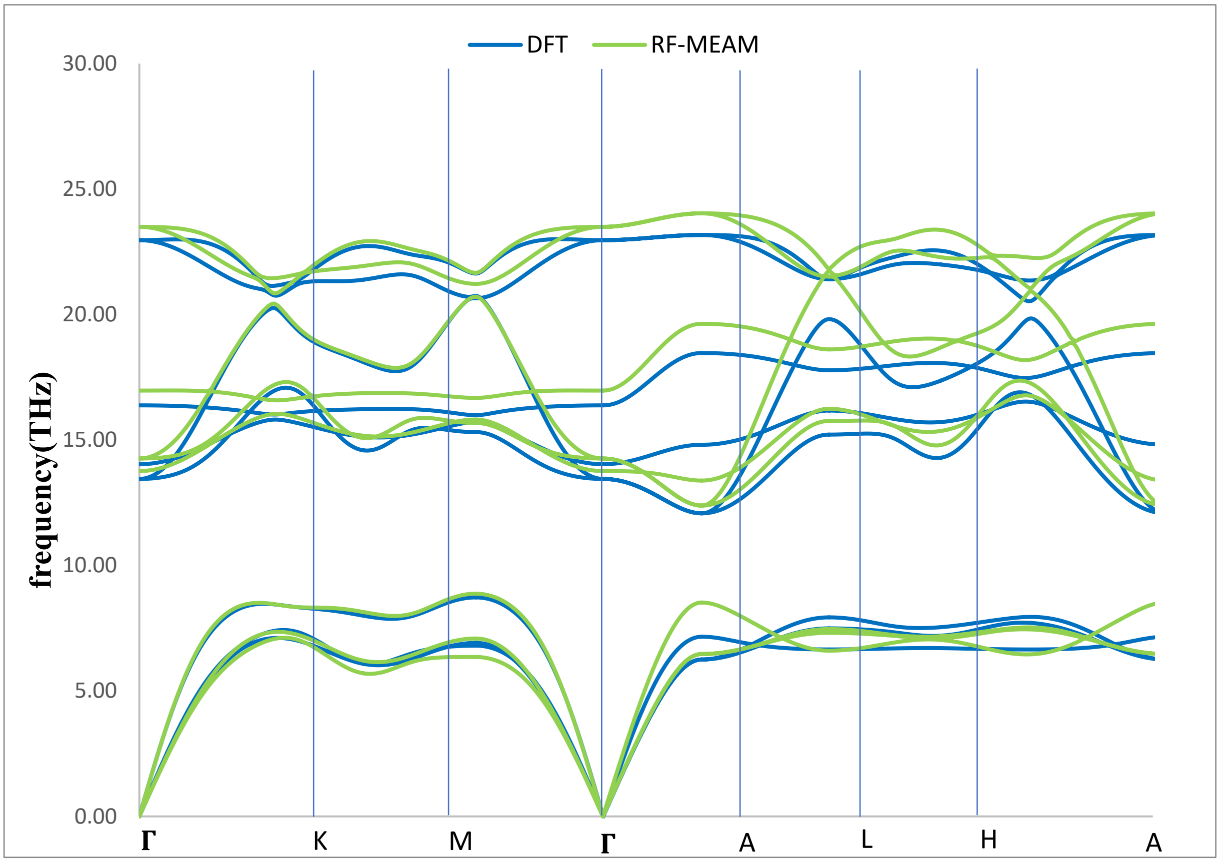

Figure 23: Phonon dispersion curve for RF-MEAM compared with DFT calculation

To understand the high temperature behavior of EAM potential I studied phonon dispersion curve. While same sampling was used for both EAM and RF-MEAM, the phonon curve in Figure 24 uses the NVT high temperature sample up to 2500K. Inclusion of high temperature data greater than 2000K and up to 4000K drastically changes the entire optical phonon modes of vibration. While frequencies for acoustic phonon modes remains same for the high symmetry points in first Brillouin zone because these are vibrations by heavier zirconium elements. The zirconium dominated boron vibration (at 15-20 THz) and only boron vibration (greater than 20 THz and up to 25 THz) do not agree well with phonon dispersion curve obtained from DFT.

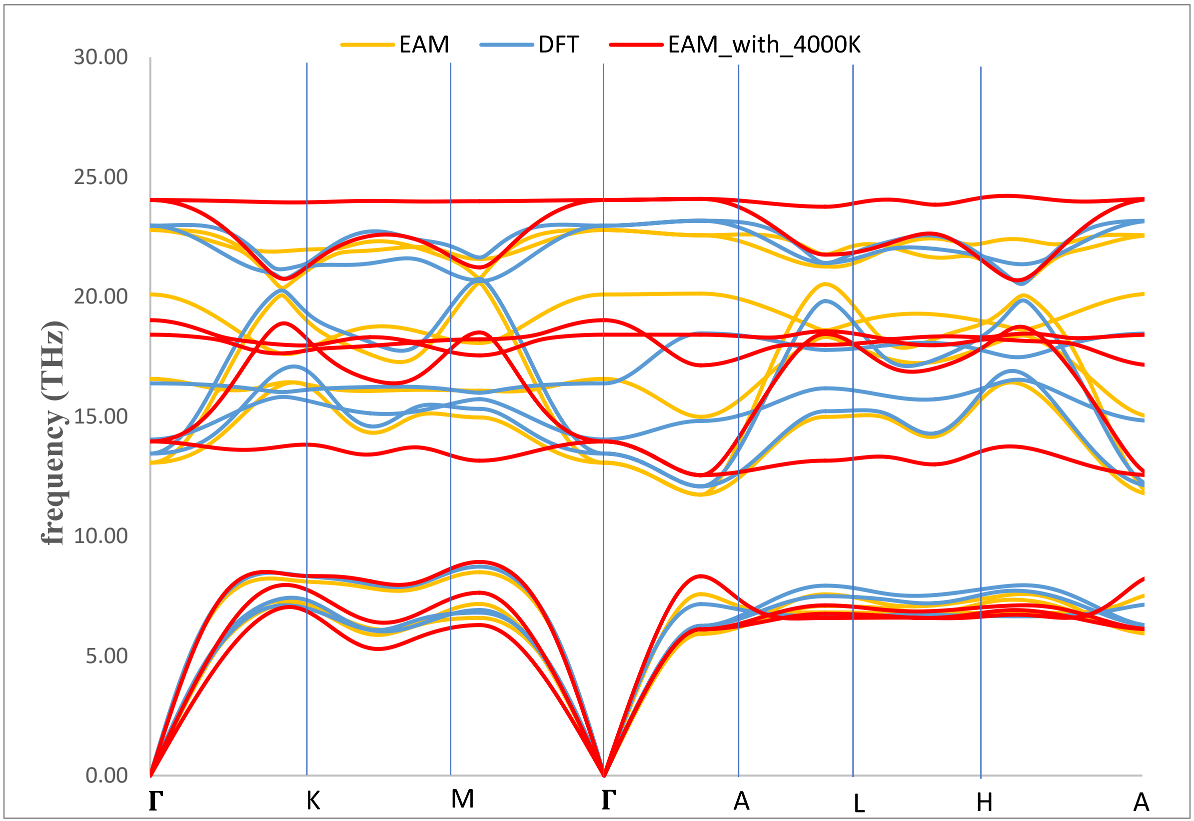

Figure 24: Phonon dispersion curve for potential generated with inclusion of higher NVT temperature sample up to 4000K

Firstly, all in-plane boron vibration is same along high symmetric path and the two phonon modes are almost identical for zirconium dominated boron vibration. At higher temperature there is more vibration and higher variations of pairs and triplets for B-Zr-B pairs are present. The inability to match these angular variations given the angular variation in high temperature data present a challenge for EAM potential to replicate thermal properties greater than 2000K. This suggest other approach must be addressed to properly account the behavior of anharmonicity at temperature greater than 2000K so that parameters in EAM potential can sense the angular variations.

The total density of states in Figure 25 shows slight shifting of the in-phase Zr vibrations by 0.3 THz, which resulted in a significant rise in occupancies of phonon modes near 16 THz and 20 THz.

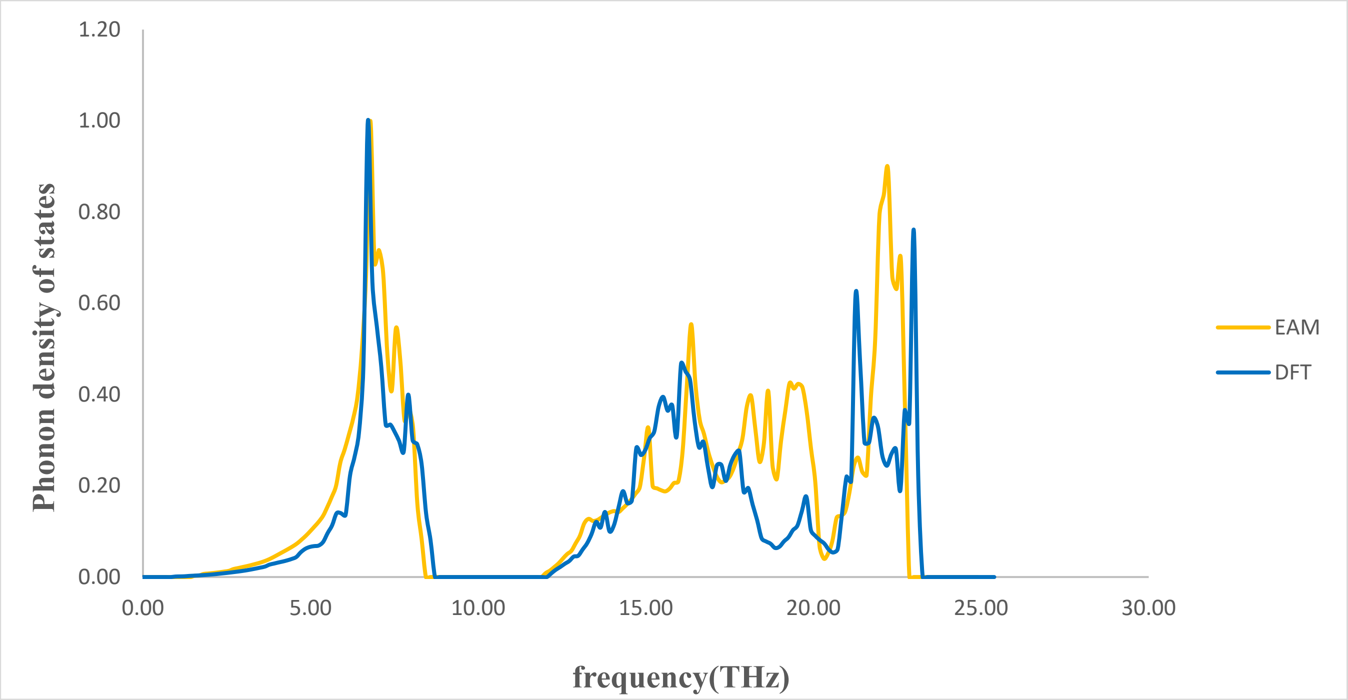

Figure 25: Density of states for zirconium diboride by EAM potential compared to that of DFT calculation

The optical phonon frequency modes operating at 14 THz and 16 THz in DFT calculations now shifts to a higher value by about 3 THz in the EAM potential. Figure 26 and Figure 27 shows the total and partial phonon density of states, which are consistent with the phonon dispersion results. These results also provide better insight into the shift of the optical phonon modes by showing that EAM overestimates specific B-vibrational frequencies at 14 THz and 16 THz in DFT calculation.

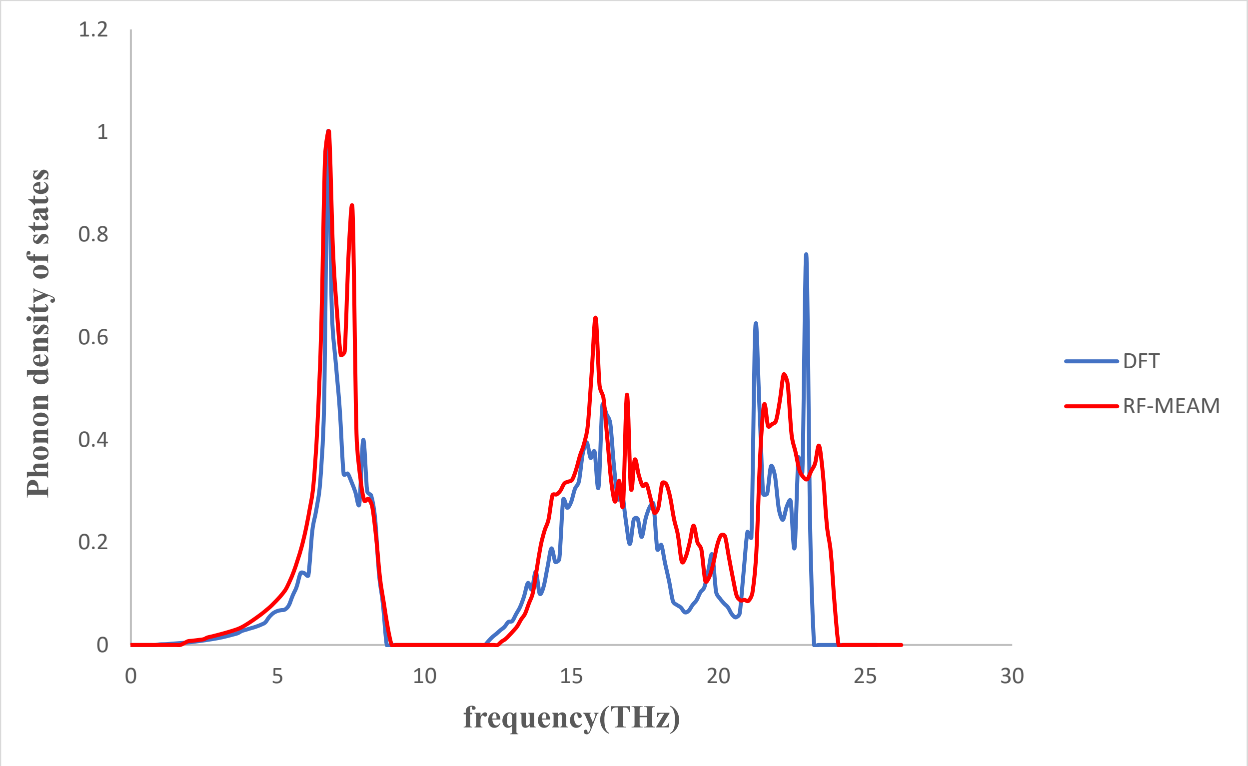

Figure 26: Density of states for zirconium diboride by RF-MEAM potential compared to that of DFT calculation

The phonon occupancies are in line with the DFT calculation for acoustic phonon modes. The density of states in Figure 26 shows that optical phonon modes (only boron vibration) has shifted by 0.7 THz. However, higher phonon occupancies near 20 THz frequency predicted by EAM potential is now significantly reduced.

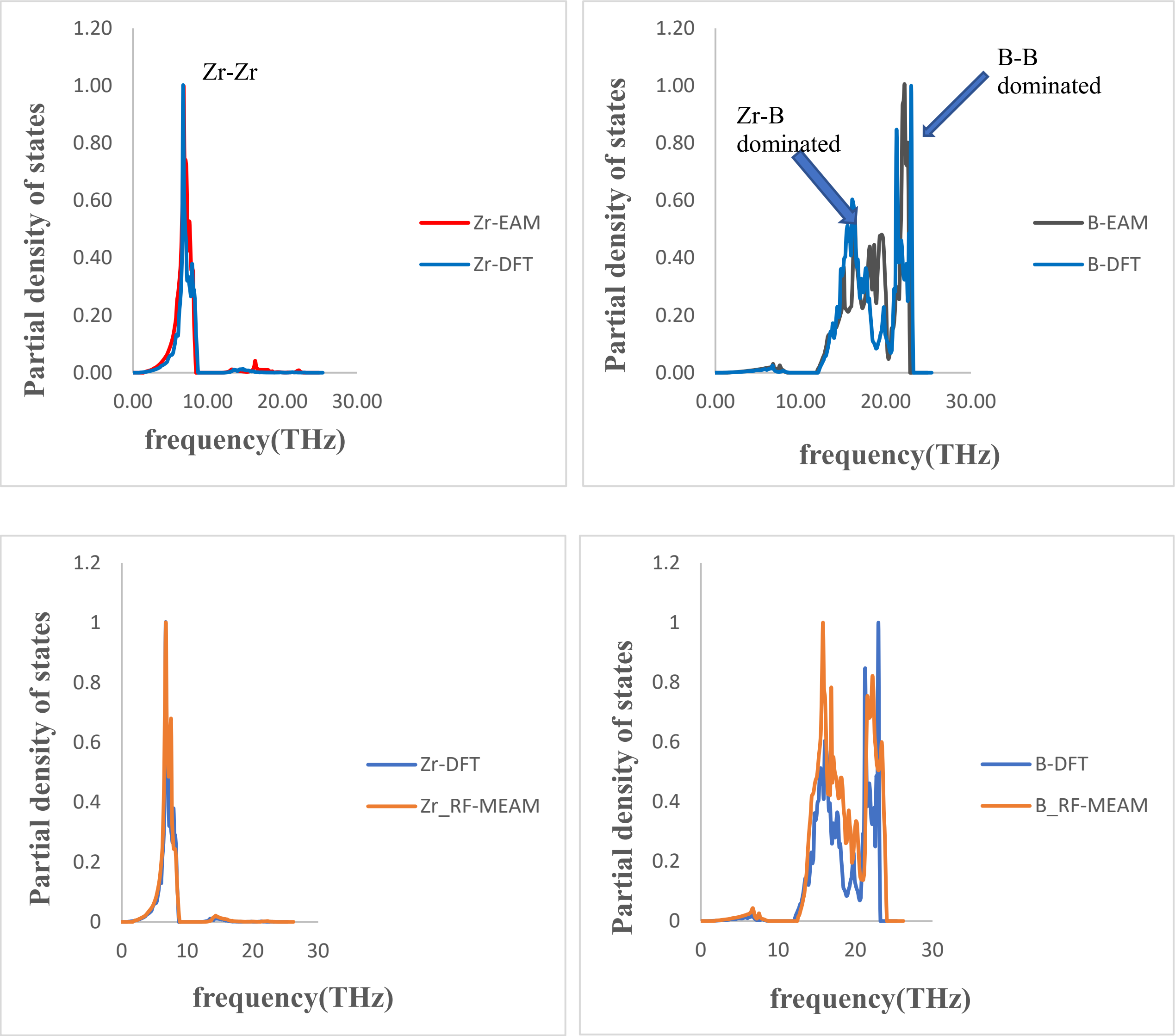

Figure 27: Partial density of states (a) top left, for Zr with EAM potential (b) top right for B with EAM potential (c) bottom left, for Zr with RF-MEAM potential (d) bottom right for B with RF-MEAM potential

I further split the density of states to atom specific contribution to identify if each of low frequency mode by zirconium is vibrating or has a contribution on phonon occupancies on higher frequency mode for both the EAM and RF-MEAM potential. Figure 27 on top left and bottom left compares the normalized phonon occupancies by zirconium against DFT calculation for both

EAM and RF-MEAM potential. While there is significant phonon occupancy of zirconium near 20 THz frequency range as compared to the DFT calculation for EAM potential, this might have resulted higher boron vibration around that frequency range on the top right of Figure 27. Unlike EAM potential no significant higher frequency vibration for zirconium is available for RF-MEAM potential as compared to DFT calculation. So, the phonon occupancy for boron dominated vibration follows the DFT calculation.

Thermal Expansion of Zirconium Diboride. For the thermal expansion or lattice expansion of zirconium diboride, LAMMPS code was used[58]. I used 10x10x10 super cell of zirconium diboride for simulating isothermal constant pressure and temperature (NPT) ensemble to find the lattice expansion at each temperature points. Metallic unit was used with a timestep of 1 fs for one million runs. The lattice parameters obtained are then normalized in a unit cell value and are plotted against the temperature. Figure 28 compares the lattice expansion using EAM potential as a function of temperature. The thermal expansion coefficient measures the rate at which the lattice expands by increasing the temperature. This anisotropic behavior on thermal expansion have been extensively studied. Several experimental studies have shown the lattice expansion at the order of $\sim 10^{-6}\ /K$ for different monocrystalline and polycrystalline sample for different temperature range[11-13, 62, 63]. The lattice expansion fitting shows that fair level of anisotropy with different lattice expansion coefficient was obtained. The lattice parameters were modelled with linear variation in temperature for both the EAM and RF-MEAM potential. The trendline below in Figure 28 represents the lattice estimation with temperature. The coefficient of linear expansion for lattice parameters a and c are given by the slope of trendline and the intercept represent the lattice parameter at room temperature. Here, large offset is seen in the lattice parameter c as compared to experimental values. This may presumably be due to activation of zirconium phonon modes at higher frequency which sweep the boron atoms along z-axis, since the higher phonon occupancy of atom specific zirconium at higher frequency (near 20 THz)

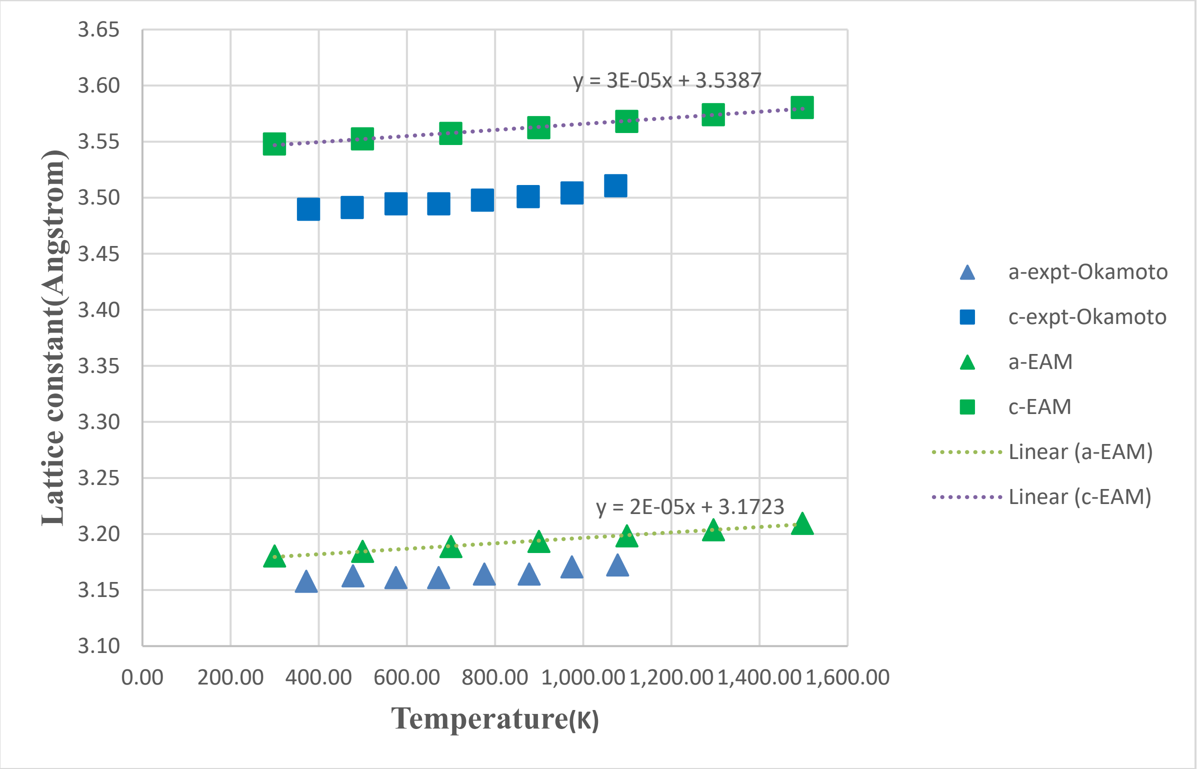

Figure 28: Lattice constant as a function of temperature using EAM potential

value in Figure 27(a). The lattice coefficient expansion for lattice parameter c is greater than that for lattice parameter a indicates that EAM potential is able to capture fair level of anisotropy in zirconium diboride. The lattice parameter using EAM potential at room temperature is obtained as $a = 3.5387$ Å and for $c = 3.1723$ Å. Similarly, the plot of lattice parameter as a function of temperature for RF-MEAM potential is shown in Figure 29. The lattice estimate with temperature is represented by the trendline in Figure 28. The slope of the trendline determines the coefficient of linear expansion for lattice parameters a and c, whereas the intercept represents the lattice parameter at room temperature. The offset in lattice parameter has been reduced by using RF-MEAM potential and may presumably be due to absent of higher frequency mode of zirconium atom as was seen on EAM potential.

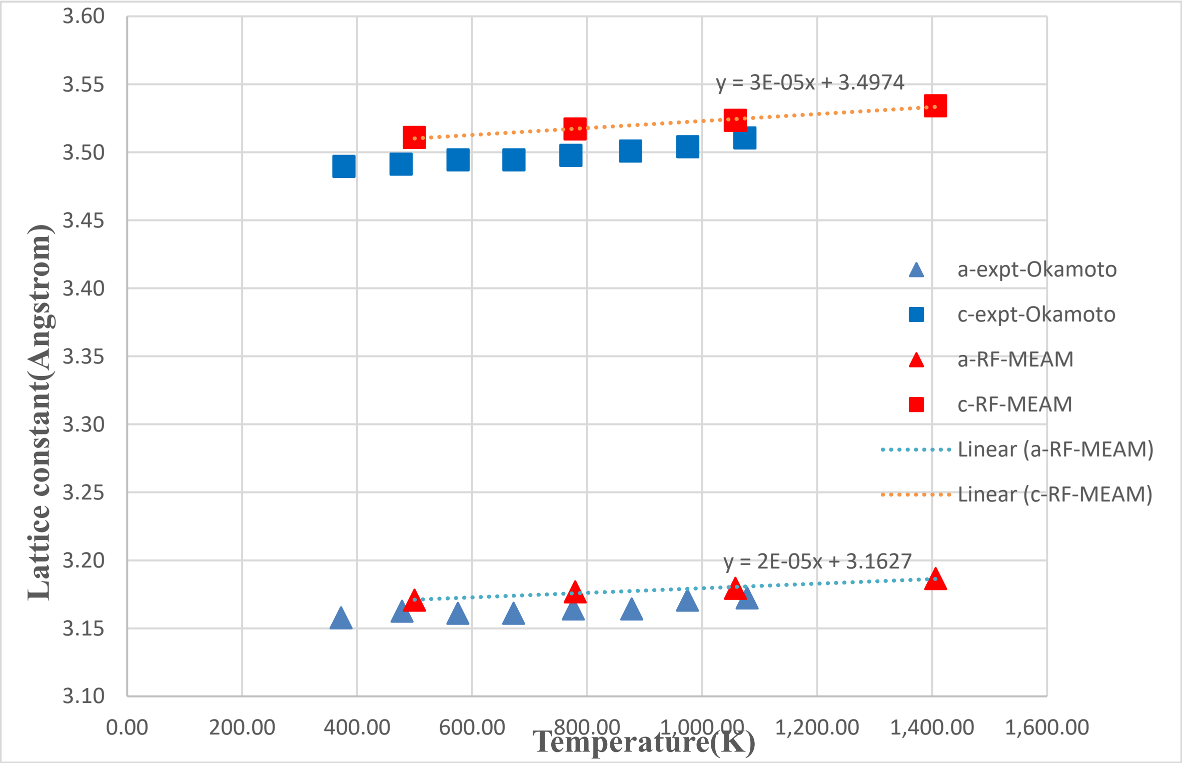

Figure 29: Lattice constant as a function of temperature compared to that from reference Okamoto et.al

Specific Heat Capacity of Zirconium Diboride. The specific heat capacity of zirconium diboride is modelled using phonopy and phonolammps. Computation of specific heat capacity of zirconium diboride was done following phonon dispersion. So, the process is similar to that of phonon dispersion. The thermal properties were set to true using phonopy to estimate the specific heat capacity from temperature range of 200K to 2000K. Specific heat capacity is a function of phonons and temperature and is given by sum of individual phonon modes as in equation (5). Figure 30 below shows the specific heat capacity of zirconium diboride using EAM potential against the DFT calculation and Tersoff potential[64]. The specific heat capacity using EAM potential has a wider difference as we go below 700K in the Figure 30 and the difference is low above 700K. The sampling used at high temperature obviously replicate the vibrations since

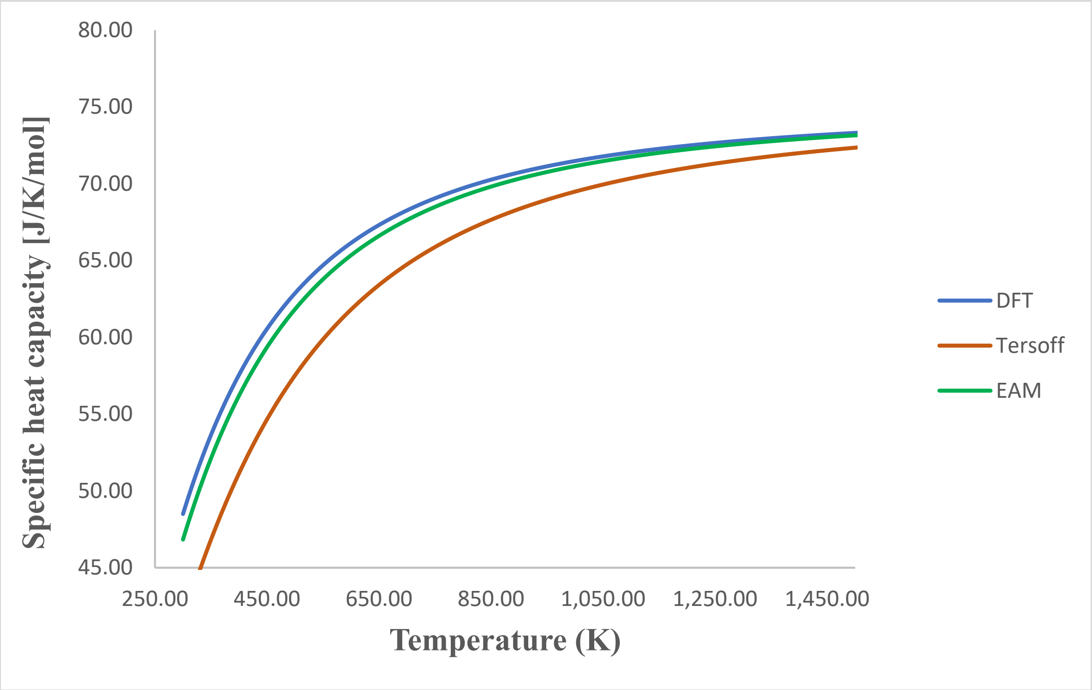

Figure 30: Specific heat capacity (Cv) as a function of temperature from DFT and EAM

the fitting procedure parametrize accordingly is also able to follow at low temperature where the sampling has not been introduced to fitting in the potential development. This is also due to the inconsistencies in the optical phonon modes obtained in EAM potential at the frequency range of 15 THz – 20 THz. However, we can see from Figure 31 that while there are still some differences at low temperature, but RF-MEAM potential is able to capture the phonon modes at this frequency range accurately as compared to EAM potential so, the difference due to specific heat capacity at low temperature is reduced.

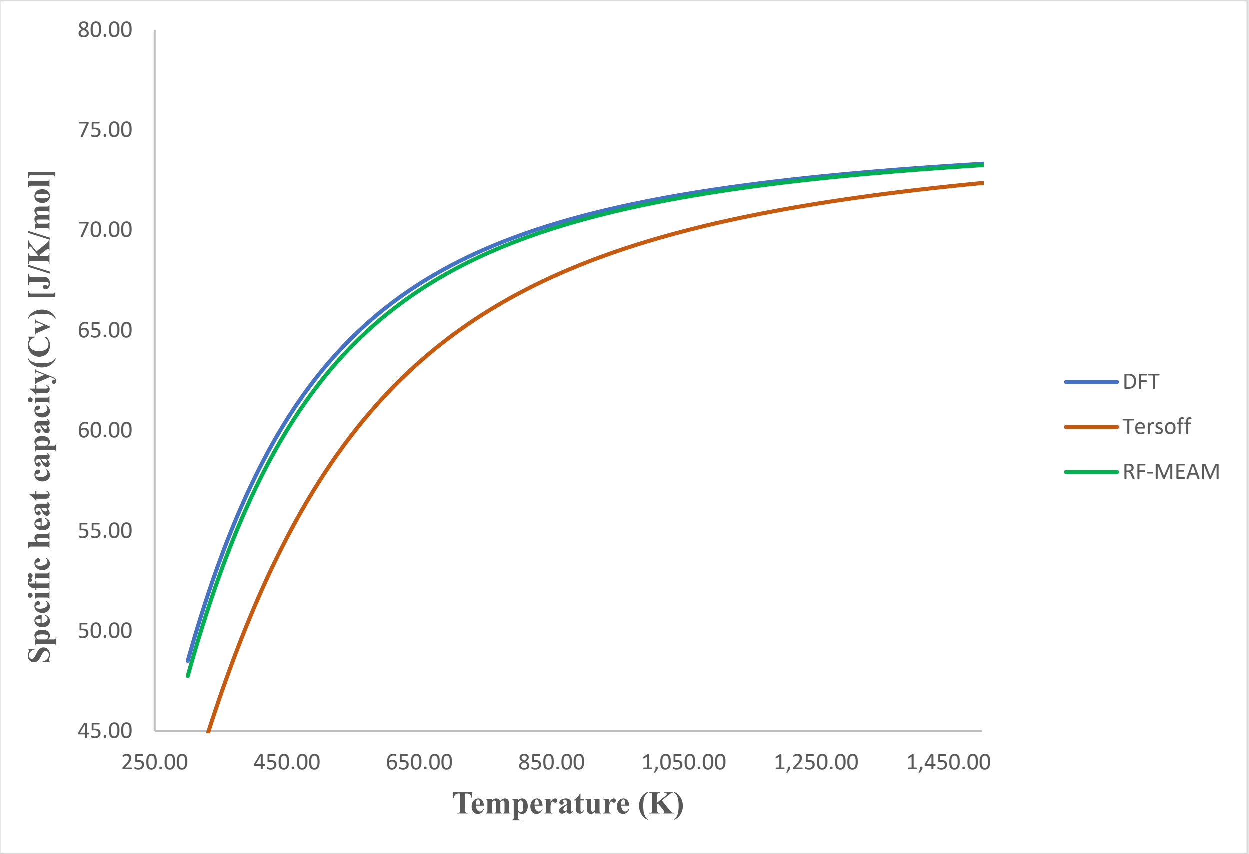

Figure 31: Specific heat capacity (Cv) as a function of temperature from DFT and RF-MEAM

Phonon Relaxation Time and Thermal Conductivity. The lattice thermal conductivity is calculated by solving phonon Boltzmann transport equation (PBTE) from the relaxation time approximation (RTA) along with Debye approximation and is shown in Figure 32. Oftentimes these are anharmonic calculation involving second and third order inter atomic force constants. The Debye-Callaway model present effective lattice thermal conductivity calculation considering

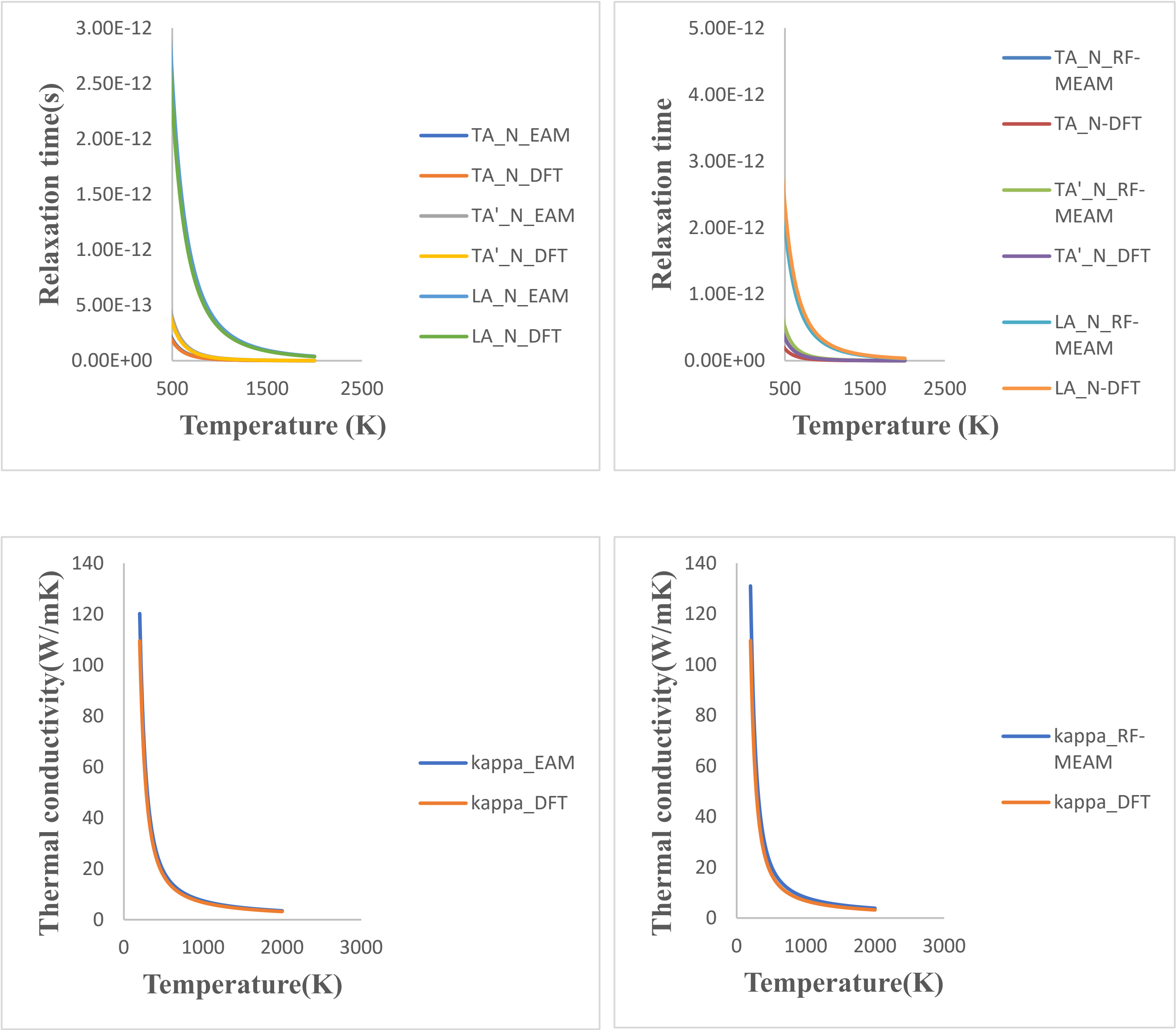

Figure 32: Phonon relaxation time and lattice thermal conductivity using EAM and RF-MEAM (a) top left, relaxation time for normal phonon process using EAM (b) top right, relaxation time for normal phonon process using RF-MEAM (c) bottom left, thermal conductivity using EAM (d) bottom right, thermal conductivity using RF-MEAM

four major scattering mechanisms including normal three-phonon process, Umklapp process, boundary scattering and isotopes disorder scattering. I used AICON to calculate the phonon relaxation time and thermal conductivity[56]. In Debye-Callaway model only acoustic branches of the phonon are considered for thermal conductivity, but AICON uses optical branches as well. At high temperature, optical branch contributes around 20% -40% for thermal conductivity. Figure 32 (a) and (b) represent the normal phonon relaxation time for zirconium diboride as a function of temperature. The normal phonon process follows fifth power of temperature and are more dominant in low temperature regime. Figure 32 above shows that the relaxation time obtained from both the potentials are of the order of pico seconds at $500\ K$. The normal phonon process quickly decays and Umklapp phonon process dominate where the scattering rate falls exponentially from Aspen-Palmer and Morelli[65, 66].

I also compared the lattice conductivity of zirconium diboride using the method formulated in the AICON code[56]. Thermal conductivity was computed using both the potentials and are compared with that of DFT calculation. While no such large difference is observed in the thermal conductivity from DFT, and potentials as seen from the Figure 32 (c) and (d). However, experimental value of thermal conductivity by Zhang is about 10 W/mK low as compared to DFT and potential calculation at temperature of 500K[14]. This is due to the polycrystalline sample of zirconium diboride being used. The difference decreases at high temperature because phonon thermal conduction becomes low since more of the electronic thermal conductivity at high temperature.

Mechanical Properties of Zirconium Diboride

Five independent elastic constants exist in hexagonal crystals. There are three distinct elastic shear constants and consequently three shear type anisotropy ratios for anisotropic crystals like zirconium diboride[67]. The Cij matrix principal minors are all positive-definite for anisotropic hexagonal crystals, thus there are three independent stability criteria for hexagonal crystals given by[67]

$$C_{11} > C_{12} \qquad \text{(i)}$$

$$C_{44} > 0 \qquad \text{(ii)}$$

$$(C_{11} + C_{12})C_{33} > 2C_{12}^2 \qquad \text{(iii)}$$

These ground state elastic constants calculation was performed using DFT calculation and was evaluated using LAMMPS for both the EAM and RF-MEAM potential. The DFT calculation of elastic constants was performed using VASP. IBRION=6 was used to calculate elastic constants using a 2x2x2 super cell of zirconium diboride. For this computation, a kinetic energy cutoff of 600 eV and a Monkhorst-Pack scheme of 11x11x11 were employed. The computation was done using the plane wave basis projector augmented wave method and the Perdew-Burke-Ernzerhof (PBE) parametrization of the generalized gradient approximation of exchange correlation[49-51]. The ground state elastic constants calculation for both EAM and RF-MEAM potential along with DFT calculation is given below in Table 4.

Table 4: Ground state elastic constant and bulk modulus using EAM and RF-MEAM potential

	C_{11}(GPa)	**C_{12}(GPa)**	**C_{13}(GPa)**	**C_{33}(GPa)**	**C_{44}(GPa)**	**B(GPa)**
DFT	554	61	123	428	246	238
RF-MEAM	536.24	84.322	152.33	424.63	250.19	254.78
EAM	574.40	165.23	140.16	334.38	212.47	263.81
Tersoff	422	156	171	320	119	240

Further, I also perform high temperature elastic constant calculation using LAMMPS. Figure 33 below is a plot of all elastic constants for different temperature using EAM potential.

As expected, the EAM potential is able to explain most of the elastic constants due to compressive stress and compressive strain because of sampling at different volumes; for instance, the value of C_{11} obtained from EAM potential is $574.40\ GPa$ and that by DFT calculation is $554\ GPa$ and similarly, C_{13} by EAM potential is $140.16\ GPa$ and that by DFT calculation is $123\ GPa$. The elastic constants due to shear stress and shear strain also closely resemble the DFT calculation as C_{44} by EAM potential and DFT calculation are $212.47\ GPa$ and $246\ GPa$. The values of elastic constants and bulk modulus of ZrB_2 by EAM potential, DFT calculation, and that by Dawson (Tersoff potential) are shown in Table 4[64]. The EAM results fare better than the ones predicted by the current Tersoff potential. This is presumably due to the more complex interactions that are considered in the EAM calculations as opposed to the 3-body interaction considered by the Tersoff method. The shear-related elastic constants such as C_{12} and C_{44}, while they are generally more accurate than those predicted using Tersoff, remain a challenge. Moreover, due to the limited statistics for the high force data along the y-axis, a larger divergence in C_{12} i.e., higher in comparison to that of experimental reference as also observed. The elastic constants at the ground state as obtained using the RF-MEAM interatomic potentials are also shown in Table 4. Significant improvement was noted in the elastic constant predictions using RF-MEAM compared to EAM, especially C_{12} and C_{13} obtained by utilizing the RF-MEAM when compared to DFT results. In the RF-MEAM potential, C_{12} was 84.332 GPa.

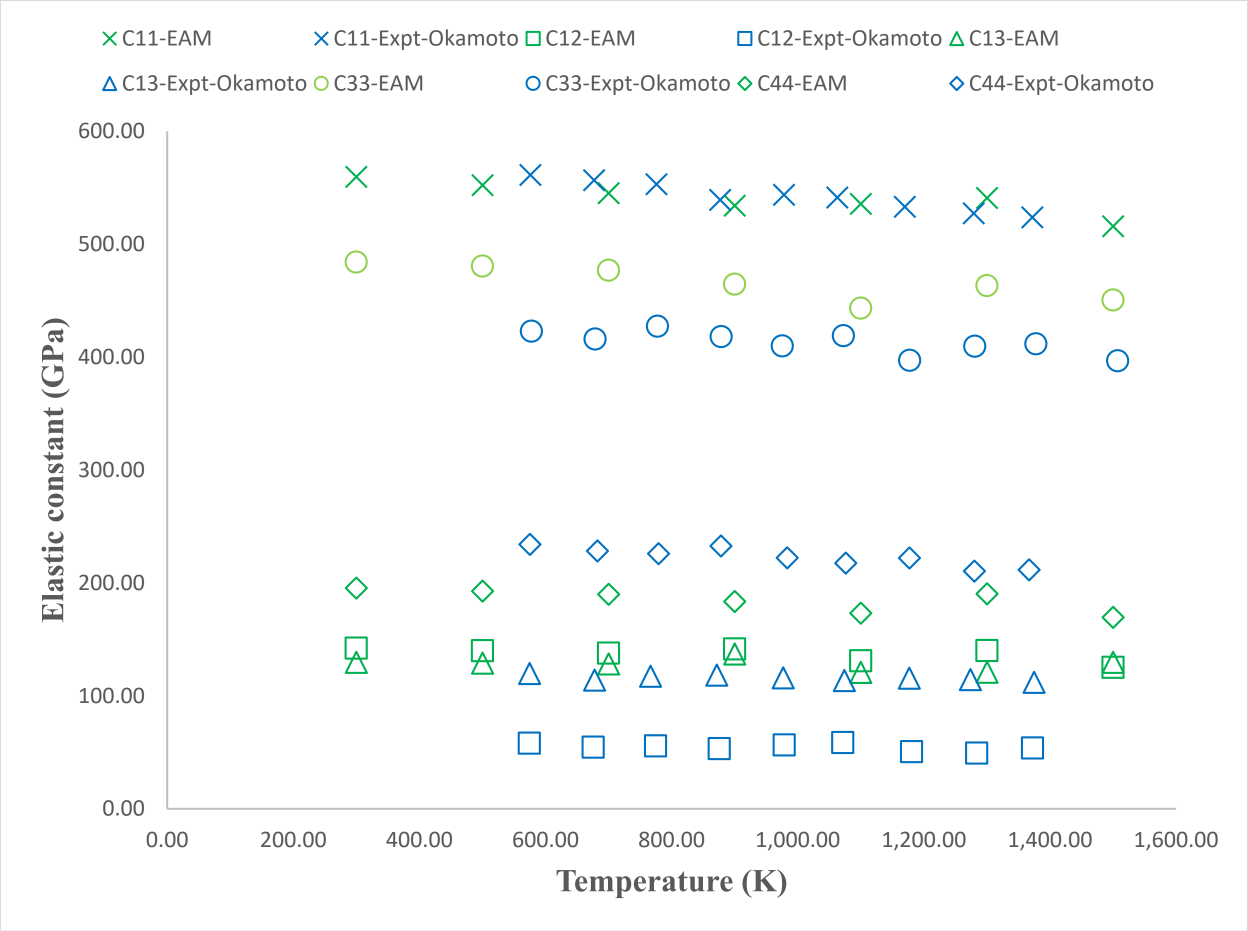

Figure 33: Variation of elastic constants with temperature compared to that of Okamoto using EAM potential

The same elastic constant was highly overestimated by the EAM potential at 165.23 GPa relative to the DFT results calculated from the DFT based of 61 GPa. Thus, using RF-MEAM has eliminated the large over estimation in Figure 34 of shear-stress related C_{12} (green color plots) by about 70 GPa that occurred with EAM, in this case, has been alleviated by almost 80 GPa utilizing RF-MEAM. In addition, the elastic constants as a function of temperature are also much closer to those observed experimentally as shown in Figure 33. This shows the benefits of adding the angular dependency as a part of RF-MEAM formulism, especially considering the relatively limited shear deformation related sampling utilized for the optimization procedures.

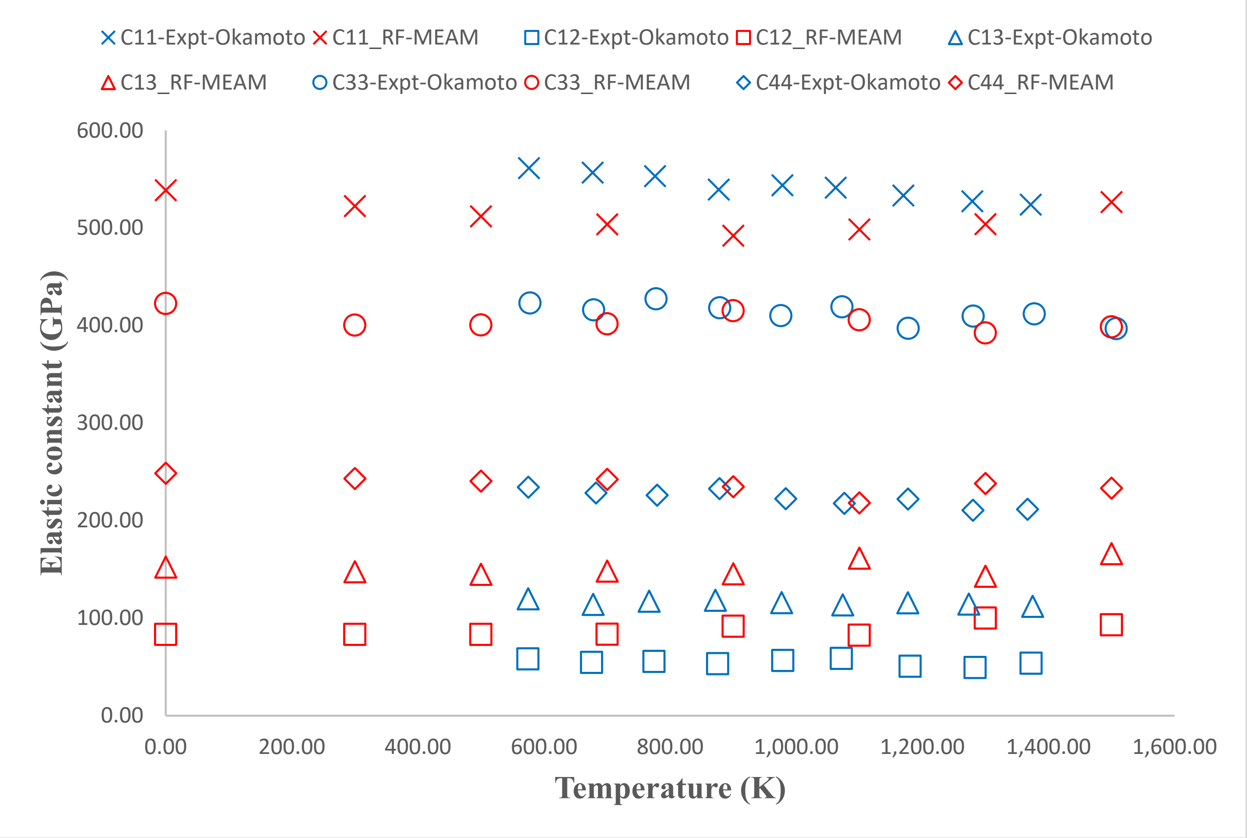

Figure 34: Variation of elastic constants with temperature compared to that of Okamoto using RF-MEAM potential

CONCLUSION

I present a review of my study for the development of EAM and RF-MEAM interatomic potential for zirconium diboride in this chapter and will summarize the effectiveness of both the EAM and RF-MEAM potential, shortcoming in our approach on sampling as well as fitting and will talk about our future steps for creating robust potentials.

The overarching goal of this project is to develop an EAM and RF-MEAM potential for thermal properties of zirconium diboride through energy and force-fitting method using MEAMfit. The approaches used in this study were as follows: 1) design structures that would allow to evaluate the energy, forces and capture vibrations associated with high temperature system, 2) execute DFT/AIMD calculations to obtain force and energy data for a specific system, and then, lastly, 3) fit the obtained DFT data to a specific potential function to build the desired potential. The overall results give a consistency on matching energy, force and stress dataset of the DFT calculation. Some inconsistencies, however, were observed in higher force fit along y- and z-axis for EAM potential. This may be due to the EAM potential not being able to capture high temperature vibration as evidenced by phonon dispersion curve after introducing high temperature data beyond 2500K. All of the thermal properties evaluated using EAM and RF-MEAM potential suggest that EAM and RF-MEAM potential is applicable in describing thermal properties of zirconium diboride. Phonon dispersion, thermal expansion and elastic constants calculation shows that RF-MEAM potential is effective over EAM potential. While the EAM potential is unable to capture higher temperature vibration by introducing higher temperature sample data beyond 2500K. Volume sampling technique has to be addressed for the high temperature sample in EAM potential if it were to capture anharmonic vibration above 2000K.

Since all of the volume sampling were done to get phonon pressure that would get the correct harmonic vibration (second order) as well as higher order vibration (third order and so on). Different strategy has to be applied for volume sampling at high temperature in developing EAM potential. As we expand and contract volumes in a hope that it would add higher order vibration as much as possible in the energy and force sample. This could also be done other way i.e., since the harmonic energy is proportional to square of displacement and similarly the anharmonic energy could be energy due to higher order displacement. So, we could instead displace atoms in zirconium diboride using cubic and quartic function and relax the structure based on this displaced atomic position. The relaxed structure would then be used as AIMD simulation at high temperature.

Overall, our general approach on developing interatomic potential by firstly fitting the energy and force data at relatively low temperature and then further go on adding high temperature data to fit the potential seems to work well. As far as the fitting strategy as concerned, force fitting was found to be more effective than fitting a combined the elastic constant DFT dataset with the free energy fitting.

For our future studies, we will be focusing on solving the current issue with the volume sampling at higher temperature and possibly explore other sampling technique. Further, we will be working other form of diboride including high entropy diborides with five different metals in a metallic plane in zirconium diboride. Recent advances on artificial intelligence and machine learning proposes a promising application on molecular dynamics and interatomic potential development. Given the sufficient amount of data collected for zirconium diboride I would like to explore interatomic potential development for zirconium diboride and high entropy alloy diboride using machine learning.

FUTURE WORKS

For the future, I would like to work on interatomic potential development using machine learning. Machine learning potential does not assume any analytic form of the potential energy surface, it instead tries to establish a correlation between the crystal structure and the potential energy surface using large datasets, and once the correlation is established, it can be applied to other test datasets and molecular dynamics simulations. One of the most difficult difficulties in molecular modeling is precisely and effectively representing the interatomic potential energy surface (PES). Traditionally, direct application of quantum mechanics models, such as density functional theory (DFT) models, or empirically built atomic potential models, such as the embedded atomic method (EAM), have been used. The former technique is constrained by the size of the system that can be handled, whereas the latter class of methods is constrained by the model's correctness and transferability. The PES is represented by the Deep Potential model as a total of "atomic" energies that are symmetrically dependent on the coordinates of the atoms in each atomic environment[68, 69]. It is a Python/C++ tool that reduce computation time to create a deep learning model of interatomic potential energy and force field and perform molecular dynamics (MD). This raises new hopes for resolving the accuracy-versus-efficiency conundrum in molecular simulations. DeePMD-kit has applications ranging from finite molecules to extended systems, as well as metals.

The DeepMD-kit works on three folds, prepare the data, train the dataset and test the data. Also, other code such as alamode and phonolammps along with phonopy can be interfaced with the DeePMD-kit to model different materials properties using molecular dynamics simulation. To create the deep potential, I used the same sample data for creating EAM and RF-

MEAM potential. The input data format used by deep potential is python numpy format. Dpdata code was used to convert the all the AIMD data set into python numpy format. The detailed code for preparing the dataset is given below in the APPENDIX.

For training deep potential, the number of neighboring atoms for each zirconium and boron was set to 87 and 93. Smooth cut off radius of 6.2 Å was used and for the model the neuron size was set to 25, 50 and 100. For fitting ResNET of neuron size 240, 240, 240 was used. The learning rate was set to exponential and the potential was trained up to two million batches. Figure 35 below shows the phonon dispersion curve using deep potential. The deep potential clearly replicates the DFT calculation and has a good representation of optical phonon modes. The deep potential is able to replicate the zirconium dominated boron vibration in the frequency range of 15-20 THz.

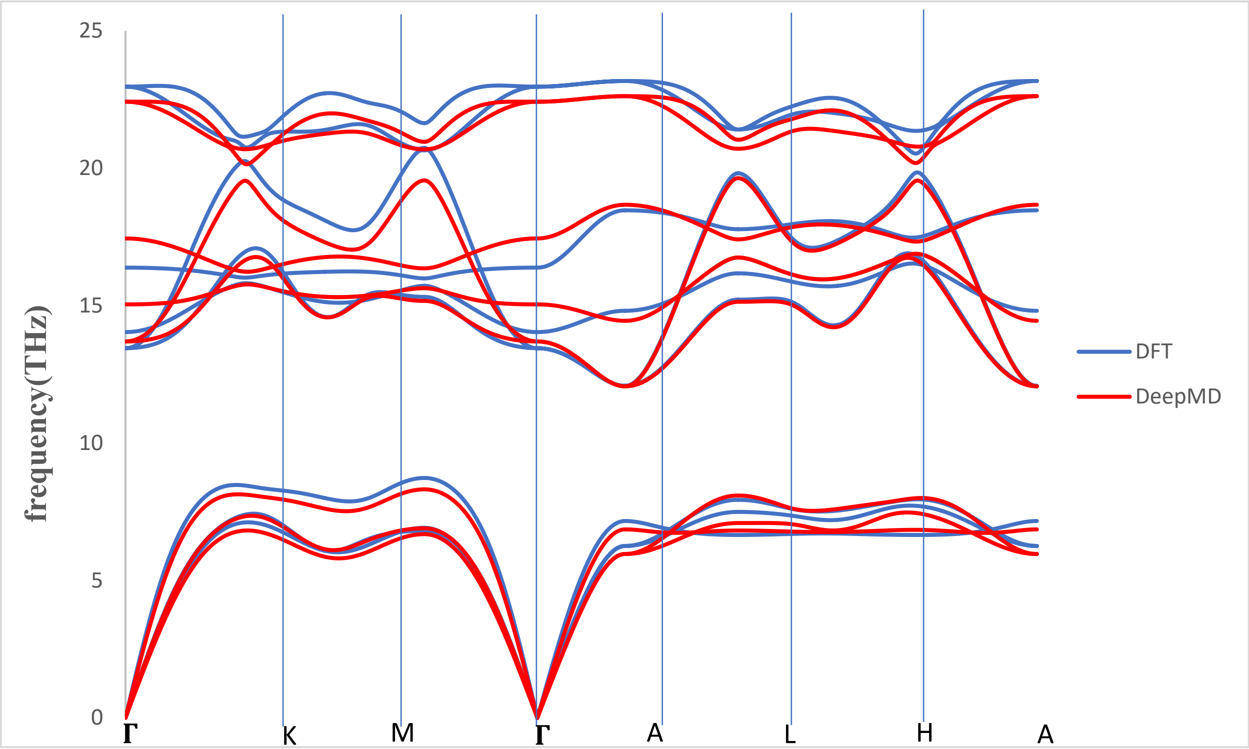

Figure 35: Phonon dispersion curve using Deep Potential compared to that of DFT

REFERENCES

[1] K. Upadhya, J. Yang, and W. Hoffman, “Materials for ultrahigh temperature structural applications,” *Am. Ceram. Soc. Bull.*, vol. 76, no. 12, pp. 51-56, 1997.

[2] W.G. Fahrenholtz, G. Hilmas, I. Talmy, and J. Zaykoski, “Refractory Diborides of Zirconium and Hafnium,” *J. Am. Ceram. Soc.,* vol. 90, no. 5, pp. 1347-1364, 2007.

[3] C. Mroz, “Zirconium diboride,” *Am. Ceram. Soc. Bull.*, vol. 73, no. 6, pp. 141-142, 1994.

[4] A.S. Brown, “Hypersonic designs with a sharp edge,” *Amer Inst Aeronaut Astronaut,* vol. 39, no. 9, pp. 20-21, 1997.

[5] H. Moissan, *Comptes Redus Hebdomadaires des Seances de l’Academie des Sci-ences*, vol. 122, pp. 651, 1896.

[6] C. Jesse Ingram, “Current status of refractory metals for structural applications,” in *Joint Conference on Lifting Manned Hypervelocity and Reentry Vehicles*, Langley Field, Virginia, 1960, pp. 1-10.

[7] W.H. Steurer, R. M. Crane, L. L. Gilbert, C. A. Hermach, E. Scala, E. J. Zeilberger, and R. H. Raring, “Thermal Protection Systems: Report on the Aspects of Thermal Protection of Interest to NASA and the Related Materials R&D Requirements,” National Aeronautics and Space Administration, Washington D.C., 1962.

[8] E.L. Courtright, H.C. Graham, A.P. Katz, and R.J. Kerans, “Ultrahigh temperature assessment study-ceramic matrix composite,” Pacific Northwest Laboratory, Richland, WA, Sept., 1992.

[9] L. Kaufman and E.V. Clougherty, “Investigation of boride compounds for very high temperature applications,” ManLabs Inc, Cambridge, MA, 1963.

[10] W.G. Fahrenholtz and G. Hilmas, “Ultra-high Temperature Ceramics: Materials for Extreme Environments,” *Scr. Mater.,* vol. 129, pp. 94-99, 2017.

[11] D. Kovalev, et al., “Thermal Expansion of Micro- and Nanocrystalline ZrB_2 Powders,” *Inorganic Materials*, vol. 56, no. 3, pp. 258-264, 2020.

[12] F. Keihn and E. Keplin, “High-Temperature Thermal Expansion of Certain Group IV and Group V Diborides,” *J. Am. Ceram. Soc.,* vol. 50, no. 2, pp. 81-84, 1967.

[13] I. Engström and B. Lönnberg, “Thermal expansion studies of the group IV-VII transition-metal disilicides,” *J. Appl. Phys.*, vol. 63, no. 9, pp. 4476-4484, 1988.

[14] L. Zhang, D. Pejaković, J. Marschall, and M. Gasch, “Thermal and Electrical Transport Properties of Spark Plasma-Sintered HfB_2 and ZrB_2 Ceramics,” *J. Am. Ceram. Soc.,* vol. 94, no. 8, pp. 2562-2570, 2011.

[15] G. Mahajan, N. Karve, U. Patil, P. Kuppan, and K. Venkatesan, “Analysis of Microstructure, Hardness and Wear of Al-SiC-TiB_2 Hybrid Metal Matrix Composite,” *Indian J. Sci. Technol.*, vol. 8, no. 2, p. 101, 2015.

[16] R.P. Tye and E.V. Clougherty, “Thermal and Electrical Conductivities of Some Electrically Conducting Compounds,” in *Proc. of the Fifth Symposium on Thermophysical Properties,* Cambridge, MA, Sept.-Oct., 1970.

[17] S. Guo, Y. Kagawa, T. Nishimura, and H. Tanaka, “Thermal and Electric Properties in Hot-Pressed ZrB_2-$MoSi_2$-SiC Composites,” *J. Am. Ceram. Soc.,* vol. 90, no. 7, pp. 2255-2258, 2007.

[18] W. Tian, Y. Kan, G. Zhang, and P. Wang, “Effect of carbon nanotubes on the properties of ZrB_2–SiC ceramics,” *Mater. Sci. Eng., A*, vol. 487, no. 1-2, pp. 568-573, 2008.

[19] J. Zimmermann, G. Hilmas, W. Fahrenholtz, R. Dinwiddie, W. Porter, and H. Wang, “Thermophysical Properties of ZrB_2 and ZrB_2–SiC Ceramics,” *J. Am. Ceram. Soc.*, vol. 91, no. 5, pp. 1405-1411, 2008.

[20] L. Solymar, D. Walsh, and R.R. Syms, *Electrical properties of materials.* Oxford, England: Oxford university press, 2014.

[21] P. Rennert and D. Jiles, *Introduction to the Electronic Properties of Materials.* London, England: Chapman & Hall, 1994.

[22] G. Samsonov, B. Kovenskaya, and T. Serebryakova, “Some physical characteristics of the diborides of transition metals of groups IV and V,” *Soviet Physics Journal*, vol. 14, no. 1, pp. 11-14, 1973.

[23] M. Dove, “Introduction to the theory of lattice dynamics,” *École thématique de la Société Française de la Neutronique*, vol. 12, pp. 123-159, 2011.

[24] N. W. Ashcroft and N. D. Mermin, *Solid state physics.* New York, USA: Holt, Rinehart and Winston, 1976.

[25] D. Zhou, “An Introduction of Density Functional Theory and its Application,” *Physics. Drexel. Edu*, 2007.

[26] J. Tse, “Ab Initio Molecular Dynamics with Density Functional Theory,” *Annu. Rev. Phys. Chem.*, vol. 53, no. 1, pp. 249-290, 2002.

[27] P. Hohenberg and W. Kohn, “Inhomogeneous Electron Gas,” *Phys. Rev.*, vol. 136, no. 3, pp. B864-B871, 1964.

[28] M. Tuckerman, “Ab initio molecular dynamics: basic concepts, current trends and novel applications,” *J. Phys.: Condens. Matter*, vol. 14, no. 50, pp. R1297-R1355, 2002.

[29] E. Paquet and H. Viktor, “Computational Methods for Ab Initio Molecular Dynamics,” *Advances in Chemistry*, vol. 2018, pp. 1-14, 2018.

[30] R. Zhou, *Molecular modeling at the atomic scale*. Boca Raton, FL: CRC Press, 2014.

[31] H. Andersen, “Molecular dynamics simulations at constant pressure and/or temperature,” *J. Chem. Phys.*, vol. 72, no. 4, pp. 2384-2393, 1980.

[32] D. Evans and B. Holian, “The Nose–Hoover thermostat,” *J. Chem. Phys.*, vol. 83, no. 8, pp. 4069-4074, 1985.

[33] T. Helgaker, P. Jorgensen, and J. Olsen, *Molecular Electronic-Structure Theory*. New York: John Wiley & Sons, 2014.

[34] W. Koch and M. Holthausen, *A Chemist's Guide to Density Functional Theory*, 2nd ed. Wiley-VCH, 2001.

[35] O.B. Firsov, “Calculation of atomic interaction potentials,” *Zh. Eksp. Teor. Fiz*, vol. 33, pp. 696, 1957.

[36] J. Ziegler and J. Biersack, “The Stopping and Range of Ions in Matter,” *Treatise on Heavy-Ion Science*, pp. 93-129, 1985.

[37] H. Jensen, “The charge distribution in ions and the lattice constant of rubidium by the static method,” *Z Phys,* vol. 77, pp. 722-745, 1932.

[38] J.E. Jones, “On the determination of molecular fields. —II. From the equation of state of a gas,” in *Proc. of the Royal Society of London. Series A, Containing Papers of a Mathematical and Physical Character*, vol. 106, no. 738, 1924, pp. 463-477.

[39] P. Morse, “Diatomic Molecules According to the Wave Mechanics. II. Vibrational Levels,” *Phys. Rev.*, vol. 34, no. 1, pp. 57-64, 1929.

[40] J. Tersoff, “New empirical approach for the structure and energy of covalent systems,” *Phys. Rev. B*, vol. 37, no. 12, pp. 6991-7000, 1988.

[41] M. Stott and E. Zaremba, “Quasiatoms: An approach to atoms in nonuniform electronic systems,” *Phys. Rev. B*, vol. 22, no. 4, pp. 1564-1583, 1980.

[42] J. Nørskov and N. Lang, “Effective-medium theory of chemical binding: Application to chemisorption,” *Phys. Rev. B*, vol. 21, no. 6, pp. 2131-2136, 1980.

[43] M. Daw and M. Baskes, “Semiempirical, Quantum Mechanical Calculation of Hydrogen Embrittlement in Metals,” *Phys. Rev. Lett.*, vol. 50, no. 17, pp. 1285-1288, 1983.

[44] R. Johnson and D. Oh, “Analytic embedded atom method model for bcc metals,” *J. Mater. Res.*, vol. 4, no. 5, pp. 1195-1201, 1989.

[45] M. Baskes, J. Nelson, and A. Wright, “Semiempirical modified embedded-atom potentials for silicon and germanium,” *Phys. Rev. B*, vol. 40, no. 9, pp. 6085-6100, 1989.

[46] A. Duff, M. Finnis, P. Maugis, B. Thijsse, and M. Sluiter, “MEAMfit: A reference-free modified embedded atom method (RF-MEAM) energy and force-fitting code,” *Comput. Phys. Commun.*, vol. 196, pp. 439-445, 2015.

[47] M. Timonova and B. Thijsse, “Optimizing the MEAM potential for silicon,” *Modell. Simul. Mater. Sci. Eng.,* vol. 19, no. 1, p. 015003, 2010.

[48] N. Hine, J. Dziedzic, P. Haynes, and C. Skylaris, “Electrostatic interactions in finite systems treated with periodic boundary conditions: Application to linear-scaling density functional theory,” *J. Chem. Phys.*, vol. 135, no. 20, p. 204103, 2011.

[49] J. Perdew, K. Burke, and M. Ernzerhof, “Generalized Gradient Approximation Made Simple,” *Phys. Rev. Lett.*, vol. 77, no. 18, pp. 3865-3868, 1996.

[50] G. Kresse and J. Furthmüller, “Efficient iterative schemes forab initiototal-energy calculations using a plane-wave basis set,” *Phys. Rev. B*, vol. 54, no. 16, pp. 11169-11186, 1996.

[51] P. Blöchl, “Projector augmented-wave method,” *Phys. Rev. B*, vol. 50, no. 24, pp. 17953-17979, 1994.

[52] A. Jain et al., “Commentary: The Materials Project: A materials genome approach to accelerating materials innovation,” *APL Mater.*, vol. 1, no. 1, p. 011002, 2013.

[53] A. Duff, et al., “Improved method of calculating ab initio high-temperature thermodynamic properties with application to ZrC,” *Phys. Rev. B*, vol. 91, no. 21, 2015.

[54] A. Togo and I. Tanaka, “First principles phonon calculations in materials science,” *Scr. Mater.*, vol. 108, pp. 1-5, 2015.

[55] *Phonopy.* (2014). A. Togo. [online]. Available: https://phonopy.github.io/phonopy/

[56] T. Fan and A. Oganov, “AICON: A program for calculating thermal conductivity quickly and accurately,” *Computer Physics Communications*, vol. 251, p. 107074, 2020.

[57] *Phonolammps.* (2019). A. Carreras. [online]. Available: https://github.com/abelcarreras/phonolammps

[58] S. Plimpton, “Fast Parallel Algorithms for Short-Range Molecular Dynamics,” *J. Comput. Phys.*, vol. 117, no. 1, pp. 1-19, 1995.

[59] T. Tadano, Y. Gohda, and S. Tsuneyuki, “Anharmonic force constants extracted from first-principles molecular dynamics: applications to heat transfer simulations,” *J. Phys.: Condens. Matter*, vol. 26, no. 22, p. 225402, 2014.

[60] T. Tadano and S. Tsuneyuki, “Self-consistent phonon calculations of lattice dynamical properties in cubic $SrTiO_3$ with first-principles anharmonic force constants,” *Phys. Rev. B*, vol. 92, no. 5, 2015.

[61] Y. Oba, T. Tadano, R. Akashi, and S. Tsuneyuki, “First-principles study of phonon anharmonicity and negative thermal expansion in ScF_3,” *Phys. Rev. Mater.*, vol. 3, no. 3, 2019.

[62] N. Okamoto, M. Kusakari, K. Tanaka, H. Inui, M. Yamaguchi, and S. Otani, “Temperature dependence of thermal expansion and elastic constants of single crystals of ZrB2 and the suitability of ZrB2 as a substrate for GaN film,” *J. Appl. Phys.*, vol. 93, no.1, pp. 88-93, 2003.

[63] W. Paxton, et al., “Anisotropic Thermal Expansion of Zirconium Diboride: An Energy-Dispersive X-Ray Diffraction Study,” *Journal of Ceramics*, vol. 2016, pp. 1-5, 2016.

[64] M. Daw, J. Lawson, and C. Bauschlicher, “Interatomic potentials for Zirconium Diboride and Hafnium Diboride,” *Comput. Mater. Sci.*, vol. 50, no. 10, pp. 2828-2835, 2011.

[65] M. Asen-Palmer, et al., “Thermal conductivity of germanium crystals with different isotopic compositions,” *Phys. Rev. B*, vol. 56, no. 15, pp. 9431-9447, 1997.

[66] D. Morelli, J. Heremans, and G. Slack, “Estimation of the isotope effect on the lattice thermal conductivity of group IV and group III-V semiconductors,” *Phys. Rev. B*, vol. 66, no. 19, 2002.

[67] H. Ledbetter, “Elastic properties of zinc: A compilation and a review,” *J. Phys. Chem. Ref. Data*, vol. 6, no. 4, pp. 1181-1203, 1977.

[68] J. Han, L. Zhang, R. Car, and W. E, “Deep Potential: A General Representation of a Many-Body Potential Energy Surface,” *Comput. Phys. Commun.*, vol. 23, no.3, 2018.

[69] L. Zhang, J. Han, H. Wang, R. Car, and W. E, "Deep Potential Molecular Dynamics: A Scalable Model with the Accuracy of Quantum Mechanics," *Phys. Rev. Lett.*, vol. 120, no. 14, 2018.

[70] R. He, D. Fang, P. Wang, X. Zhang, and R. Zhang, "Electrical properties of ZrB2–SiC ceramics with potential for heating element applications," *Ceramics International*, vol. 40, no. 7, pp. 9549-9553, 2014.

[71] M. S. Daw and M. I. Baskes, "Embedded-atom method: Derivation and application to impurities, surfaces, and other defects in metals," *Phys. Rev. B,* vol. 29, no. 12, p. 6443, 1984.

[72] M. Finnis and J. Sinclair, "A simple empirical N-body potential for transition metals," *Philos. Mag. A,* vol. 50, no. 1, pp. 45-55, 1984.

[73] S. Foiles, M. Baskes, and M. S. Daw, "Embedded-atom-method functions for the fcc metals Cu, Ag, Au, Ni, Pd, Pt, and their alloys," *Phys. Rev. B,* vol. 33, no. 12, p. 7983, 1986.

[74] D. W. Brenner, "Relationship between the embedded-atom method and Tersoff potentials," *Phys. Rev. Lett.,* vol. 63, no. 9, p. 1022, 1989.

[75] A. Gouissem, W. Fan, A. C. Van Duin, and P. Sharma, "A reactive force-field for Zirconium and Hafnium Di-Boride," *Comput. Mater. Sci,* vol. 70, pp. 171-177, 2013.

[76] K. D. Nielson, A. C. Van Duin, J. Oxgaard, W.-Q. Deng, and W. A. Goddard, "Development of the ReaxFF reactive force field for describing transition metal catalyzed reactions, with application to the initial stages of the catalytic formation of carbon nanotubes," *J. Phys. Chem. A,* vol. 109, no. 3, pp. 493-499, 2005.

[77] A. C. Van Duin, B. V. Merinov, S. S. Jang, and W. A. Goddard, "ReaxFF reactive force field for solid oxide fuel cell systems with application to oxygen ion transport in yttria-stabilized zirconia," *J. Phys. Chem. A,* vol. 112, no. 14, pp. 3133-3140, 2008.

[78] Y. Zhang, A. Lunghi, and S. Sanvito, "Pushing the limits of atomistic simulations towards ultra-high temperature: A machine-learning force field for ZrB_2," *Acta Mater.,* vol. 186, pp. 467-474, 2020.

APPENDIX

VASP calculation

Ground state relaxation

```
PREC=accurate
ALGO=FAST
ISPIN=2
ICHARG=1
NELM=100
NELMIN=3
IBRION=2
EDIFF=0.000002
NSW=200
ISIF=3
ENCUT=520
LREAL=AUTO
ISMEAR=-5
SIGMA=0.05
LWAVE=true
LPEAD=false
LCALCPOL=false
LCALCEPS=false
EFIELD_PEAD=0, 0, 0
```

```
LEFG=false
LRHFATM=false
LMAXTAU=0
```

Elastic constant

```
PREC=High
NSW=1
ISIF=3
IBRION=6
NFREE=2
ENCUT=600
POTIM=0.01
EDIFF=1E-8
EDIFFG=-1E-8
LREAL=Auto
ISMEAR=-5
SIGMA=0.03
```

Phonon calculation

```
PREC=Accurate
ENCUT=500
IBRION=8
EDIFF=1E-8
KPAR=9
IALGO=38
```

```
ISMEAR=0
SIGMA=0.1
LREAL=.FALSE.
ADDGRID=.TRUE.
LWAVE=.FALSE.
LCHARG=.FALSE.
```

NVT calculation

```
PREC=NORMAL
EDIFF=1E-3
ENCUT=520
EDIFFG=-1E-3
NCORE=4
NELM=40
NELMIN=20
NSW=500
POTIM=1.00
ISIF=2
IBRION=0
ISYM=0
TEBEG=1500
TEEND=1500
SMASS=0
MDALGO=2
```

```
LWAVE=.FALSE.
```

phonolammps

```
units          metal
boundary       p p p
atom_style     atomic
read_data      data.zrb2
pair_style     eam/alloy
pair_coeff     * * ZrB.eam.alloy_1 Zr B
neighbor       0.5 nsq
```

phonopy

```
ATOM_NAME=Zr B
DIM=2 2 2
MP=8 8 8
BAND=0.0 0.0 0.0 0.666667 0.333333 0.0 0.5 0.0 0.0 0.0 0.0 0.0 0.0 0.0 0.5 0.5 0.0 0.5
0.666667 0.333333 0.5 0.0 0.0 0.5
FORCE_CONSTANTS=READ
```

NPT calculation

```
units          metal
boundary       p p p
atom_style     atomic
read_data      data.zrb2
pair_style     eam/alloy
pair_coeff     * * ZrB.eam.alloy_1 Zr B
```

```
neighbor        0.5 nsq


units       metal

boundary    p   p   p

atom_style  atomic


# ---------------------- ATOM DEFINITION --------------------------

read_data ZrB2_10x10x10


# ----------------------- FORCE FIELDS ----------------------------

mass 1 91.224

mass 2 10.811


pair_style      eam/alloy

pair_coeff      * * ZrB.eam.alloy_1 Zr B


# ------------------------ SETTINGS -------------------------------

compute csym all centro/atom fcc

compute peratom all pe/atom


####################################

# EQUILIBRATION

reset_timestep  0
```

```
timestep 0.001

velocity all create 300 12345 mom yes rot yes

fix 1 all npt temp 1000 1000 1 iso 0 0 1 drag 1

#fix 1 all nvt temp 1000.0 30.0 10.0

#fix 1 all nve


# Set thermo output

thermo 1000

thermo_style custom step temp lx ly lz press pxx pyy pzz pe

dump myDump all atom 10 dump_NPT_500K.atom

# Run for at least 10 picosecond (assuming 1 fs timestep)

run 1000000
```

MEAMfit

```
TYPE=EAM

CUTOFF_MAX=4.4

NTERMS=3

NTERMS_EMB=3

TYPE=RF-MEAM

CUTOFF_MAX=4.4

NTERMS=3

NTERMS_EMB=3
```

DeepMD input

```
{
```

```
    "_comment": " model parameters",
    "model": {
"type_map":["Zr", "B"],
"descriptor" :{
    "type":"se_a",
    "sel":[87, 93],
    "rcut_smth":6.20,
    "rcut":6.00,
    "neuron":[25, 50, 100],
    "resnet_dt":false,
    "axis_neuron":16,
    "seed":1,
    "_comment":" that's all"
},
"fitting_net" : {
    "neuron":[240, 240, 240],
    "resnet_dt":true,
    "seed":1,
    "_comment":" that's all"
},
"_comment":" that's all"
    },
```

```
    "learning_rate" :{
"type":"exp",
"decay_steps":5000,
"start_lr":0.001,
"stop_lr":3.51e-10,
"_comment":"that's all"
    },

    "loss" :{
"start_pref_e":0.02,
"limit_pref_e":1,
"start_pref_f":1000,
"limit_pref_f":1,
"start_pref_v":0.2,
"limit_pref_v":1,
"_comment":" that's all"
    },

    "_comment": " traing controls",
    "training" : {
"systems":["../../data/"],
"set_prefix":"set",
"stop_batch":2000000,
```

```
"batch_size":1,

"seed":1,

"_comment": " display and restart",
"_comment": " frequencies counted in batch",
"disp_file":"lcurve.out",
"disp_freq":100,
"numb_test":10,
"save_freq":1000,
"save_ckpt":"model.ckpt",
"load_ckpt":"model.ckpt",
"disp_training":true,
"time_training":true,
"profiling":false,
"profiling_file":"timeline.json",
"_comment":"that's all"
   },

   "_comment":"that's all"
}
```